



Universidad de Concepción
Dirección de Postgrado
Facultad de Ciencias Físicas y Matemáticas - Programa de Magíster en Ciencias
con Mención en Física

**SIMULACIONES N -BODY DE LOS PRIMEROS
CÚMULOS DE ESTRELLAS: CAMINO DE
FORMACIÓN PARA AGUJEROS NEGROS DE MASA
INTERMEDIA**

**(N -BODY SIMULATIONS OF PRIMORDIAL STAR
CLUSTERS: FORMATION PATHWAY FOR
INTERMEDIATE MASS BLACK HOLES)**

Tesis para optar al grado de Magíster en Ciencias
con Mención en Física

BASTIÁN ALEJANDRO REINOSO REINOSO
CONCEPCIÓN-CHILE
2018

Profesor guía: Dominik Schleicher
Dpto. de Astronomía, Facultad de Ciencias Físicas y Matemáticas
Universidad de Concepción

Agradecimientos

Primero quiero agradecer a mi familia, mi madre *Margarita Reinoso*, mis hermanos *Pablo Reinoso* y mi hermana *Pía Reinoso* por su incondicional apoyo, su comprensión y el cariño que me han brindado siempre, sin los cuales difícilmente habría logrado mis objetivos.

A mi polola y compañera de vida *Evelyn Piticar*, que me brindó su amor, paciencia, comprensión y apoyo, tranquilizandome en los momentos más difíciles y dando mucho ánimo siempre.

I would also like to acknowledge to my professors and supervisors *Michael Fellhauer* and *Dominik Schleicher* who taught me a lot during my last years doing this and other investigations and with whom I shared good moments and beers. I thank the help of my collaborators *Ralf Klessen* and *Tjarda Boekholt* for very usefull and stimulating discussions.

También agradezco a mis compañeros y amigos con quienes compartí momentos de relajo, distracción y diversión durante toda mi carrera, además de interesantes discusiones sobre nuestros trabajos.

Finalmente agradezco el soporte financiero de CONICYT a través de la beca de magíster nacional 2017, CONICYT-PFCHA/MagisterNacional/2017-22171385 que recibí durante todo el programa de magíster.

Resumen

En este trabajo mostramos cómo se pueden haber formado semillas de agujeros negros de masa intermedia en el Universo temprano a través de colisiones estelares entre las primeras estrellas del Universo que formaron cúmulos estelares densos. Nuestro trabajo se centra en estudiar los primeros cúmulos estelares, formados por estrellas de población III que según estudios recientes deben haber sido mucho más masivas y con radios más grandes, por un factor de 100, que las estrellas formadas en el universo de hoy en día. Consideramos además los cúmulos más densos formados con un *half-mass radius* de 0.1 pársec y libres de gas, y seguimos su evolución con simulaciones *N*-body usando el código NBODY6 hasta un tiempo de aproximadamente 2 Millones de años. La colisión entre dos estrellas fue tratada con la aproximación *hit and stick* asumiendo que toda la masa se conserva y que el producto de la colisión tiene la misma densidad que las estrellas que colisionan. No incluimos evolución estelar ni una función de masa inicial en nuestras simulaciones. Nuestra investigación muestra que en dichos sistemas se produce una contracción de la parte central del cúmulo por interacciones entre las estrellas, las que comienzan a fusionarse con una sola estrella en el centro del cúmulo, formando un objeto que puede llegar a contener más del 10% de la masa total del sistema. Realizamos un total de 280 simulaciones para entender cómo el número de estrellas y su tamaño influye en la formación y la masa final del objeto más masivo del cúmulo. Finalmente encontramos relaciones matemáticas que nos permiten estimar la masa del objeto a cualquier tiempo y para diferentes combinaciones del número de estrellas y su tamaño, en un cúmulo estelar del Universo temprano, mostrando que es posible formar agujeros negros con masas en el orden de $10^3 M_{\odot}$ dentro del tiempo de vida típico de las estrellas de población III. También exploramos los efectos del gas en los cúmulos y en el proceso de *runaway growth* usando un potencial de Plummer analítico y estático centrado en el cúmulo, sin acreción de masa ni expulsión de gas. Nuestros resultados muestran un incremento en el número de colisiones y en la masa del objeto final, sin embargo, encontramos un *delay* en el crecimiento del objeto más masivo relacionado a las dificultades para formar sistemas estelares binarios debido a las altas velocidades de las estrellas en esos sistemas producto de la fuerza gravitacional extra ejercida por el potencial. Finalmente realizamos las primeras simulaciones de prueba con la interfaz AMUSE, con el objetivo de acoplar en el futuro un código de hidrodinámica para tratar el gas de forma realista en futuras investigaciones. Comparamos los resultados con las simulaciones realizadas con NBODY6 encontrando un excelente acuerdo tanto en la evolución de los cúmulos como en la formación de objetos masivos en su centro.

Abstract

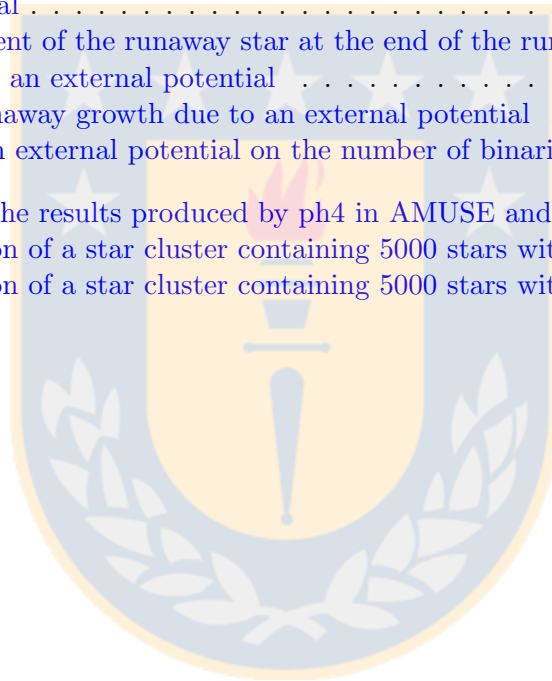
In this work we show how could have been formed intermediate mass black holes in the early Universe through stellar collisions between the first stars of the Universe that formed part of dense stellar clusters. Our work focuses on studying the first star clusters, formed by population III stars which according to recent studies they must have been much more massive and with larger radii, by a factor of 100, than the stars formed in the present day Universe. We also consider the most dense clusters formed with a half-mass radius of 0.1 parsec and gas free, and we follow their evolution with N -body simulations using the code NBODY6 until a time of approximately 2 Million years. The collision between two stars was treated with the *hit and stick* approximation assuming that all the mass is conserved and that the collision product has the same density that the colliding stars. We did not include stellar evolution nor an initial mass function in our simulations. Our research shows that in such systems there is a contraction of the central part of the cluster by interactions between the stars, which start to merge with a single star in the center of the cluster, forming an object that could contain more than 10% of the total mass of the system. We performed a total of 280 simulations to understand how the number of stars and their size influences the formation and the final mass of the most massive object. Finally we find mathematical relations that allow us to estimate the mass of the object at any time for different combinations of the number of stars and their size in a star cluster of the early Universe, showing that it is possible to form black holes with masses in the order of $10^3 M_{\odot}$ within the typical lifetime of population III stars. We also explored the effects of the gas in the clusters and in the process of runaway growth using an analytic and static Plummer potential centered in the cluster, without mass accretion nor gas expulsion. Our results show an increase in the number of collisions and in the mass of the final object, however, we found a delay in the growth of the most massive object related to the difficulties for forming binary systems due to the high velocities of the stars in these systems owing to the extra gravitational force exerted by the potential. Finally we performed the first test simulations with the AMUSE interface, with the objective of coupling in the future a hydrodynamics code to treat the gas in a realistic form in future investigations. We compared the results with the simulations performed with NBODY6 finding an excellent agreement as well as in the clusters evolution as in the formation of massive objects at their center.



List of Figures

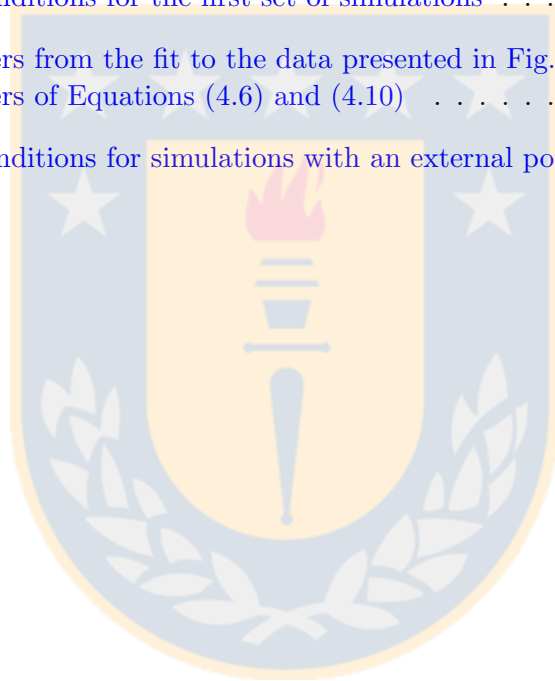
1.1	Conditions for the direct collapse scenario	4
1.2	Possible detection of the first stars	5
1.3	Three different paths for forming massive black hole seeds in the early Universe	6
1.4	Mass and Radius evolution of a protostar accreting at $\dot{M} = 10^{-3} M_{\odot} \text{ yr}^{-1}$	9
1.5	Total number of collisions in a star cluster for different initial half mass radius and different initial number of stars.	12
2.1	Block time-step scheme of NBODY6	17
2.2	Illustration of the Ahmad-Cohen scheme	19
3.1	Evolution of a star cluster with 1000 stars, each one of them with an initial radius of $500 R_{\odot}$	27
4.1	Evolution of a star cluster with 5000 stars, each one of them with an initial radius of $500 R_{\odot}$	30
4.2	Collision rate $\frac{N_{\text{col}}}{N}$ calculated in bins of 3 crossing times for the same simulation presented in Fig. 4.1	32
4.3	Collision rate $\frac{N_{\text{col}}}{N}$ calculated in bins of 5 crossing times for the same simulation presented in Fig. 4.1	32
4.4	Collision rate $\frac{N_{\text{col}}}{N}$ calculated in bins of 10 crossing times for the same simulation presented in Fig. 4.1	33
4.5	Fraction of collisions and final mass of the runaway object as function of N and R_{star}	35
4.6	Modeling the runaway growth	38
4.7	Computing the collision rate with a time interval of 2 crossing times	40
4.8	Computing the collision rate with a time interval of 10 crossing times	41
4.9	Example of a simulation with few collisions	42
4.10	Combination of the data	43

4.11	Parameters of the Gaussian fit A , t_{delay} , and t_{duration} as functions of the initial stellar radii R_{star} and initial number of stars N	45
4.12	Parameter t_{duration} of the Gaussian fit as a function of the number of stars N	47
4.13	Estimation of the number of collisions experienced by the runaway star for different combinations of N and R_{star}	48
5.1	Stability of a star cluster without an analytic potential	52
5.2	Stability of a star cluster with an analytic potential	53
5.3	Collision fraction for a gas-free star cluster	56
5.4	Mass of the runaway object for a gas-free star cluster	57
5.5	Fraction of collisions for cluster with an external potential	58
5.6	Mass of the runaway object for clusters with an external potential	58
5.7	Collision fraction at the end of the runaway growth for clusters with an external potential	59
5.8	Mass enhancement of the runaway star at the end of the runaway growth for clusters with an external potential	60
5.9	Delay in the runaway growth due to an external potential	62
5.10	The effects of an external potential on the number of binaries in a cluster	63
6.1	Comparison of the results produced by ph4 in AMUSE and NBODY6	68
6.2	General evolution of a star cluster containing 5000 stars with ph4.	69
6.3	General evolution of a star cluster containing 5000 stars with NBODY6	70



List of Tables

3.1	Initial conditions for the first set of simulations	28
4.1	Parameters from the fit to the data presented in Fig. 4.5	34
4.2	Parameters of Equations (4.6) and (4.10)	46
5.1	Initial conditions for simulations with an external potential	55



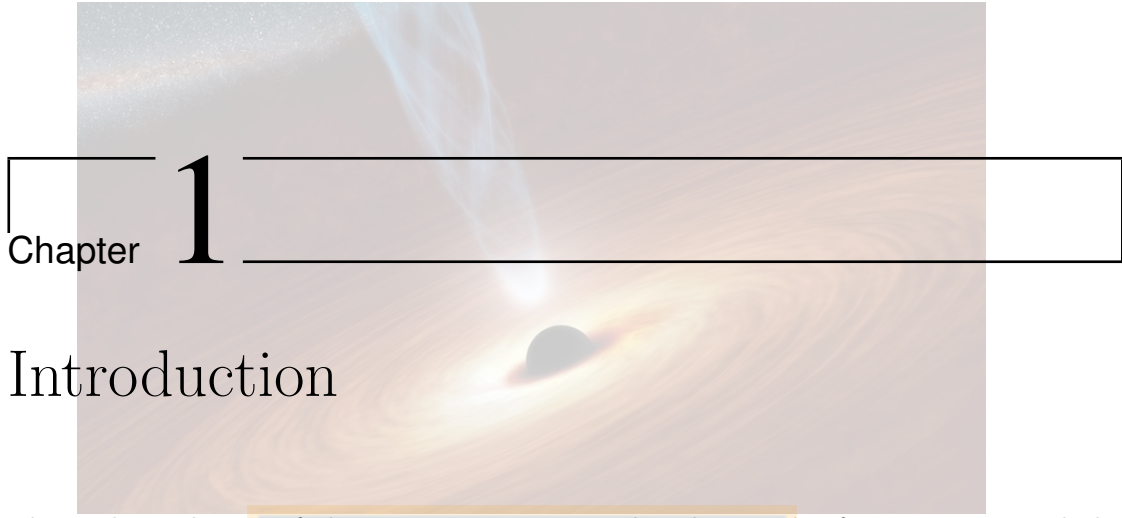


Contents

Resumen	iv
Abstract	v
List of figures	vii
List of tables	ix
1 Introduction	3
1.1 Formation of Black Holes at high redshift	3
1.2 Formation of the first stars	5
1.3 Core Collapse and Stellar Collisions	10
1.4 Previous Work	11
1.4.1 Stellar collisions in previous studies	11
1.4.2 Stellar collisions in the early Universe	12
2 NBODY6	15
2.1 General overview	15
2.2 The Hermite integrator method	15
2.3 Speeding up routines	16
2.3.1 Block and individual time-steps	16
2.3.2 The Ahmad-Cohen scheme	18
2.3.3 KS Regularization	19
2.4 Stellar Evolution and Collisions	20
2.4.1 The stellar evolution routines	20
2.4.2 Stellar collisions	21
2.5 Adaptation of the code	21
2.5.1 The stellar collisions routine	21
2.5.2 Stellar collisions and regularization	22
2.5.3 The stellar radii	23
2.5.4 Deactivating Stellar evolution	23

2.5.5	Input File for stellar collisions with NBODY6	23
3	Setup	25
3.1	Simulation time	25
3.2	Parameter space	26
4	Results	29
4.1	Evolution of the clusters	29
4.2	Time-step for computing the collision rate	31
4.3	Total number of collisions	31
4.3.1	Linear fit	34
4.4	Maximum mass	34
4.5	Number of collisions as a function of time	36
4.5.1	Modeling the runaway collision process	36
4.5.2	Collisions with the runaway object	37
4.5.3	Number of collisions per time interval	39
4.5.4	Simulations with few collisions	39
4.5.5	Combination of the data	39
4.6	Parameter estimation	42
4.6.1	The normalization factor A	44
4.6.2	The delay time and duration time of the runaway growth	44
4.6.3	Estimation of the number of collisions	46
5	Analytic gas potential	49
5.1	Analytic potential in NBODY6	49
5.1.1	Stability of the clusters under the effects of an external potential	51
5.2	First simulations	51
5.3	A delay in the runaway growth	57
5.3.1	The importance of binaries	60
6	AMUSE	65
6.1	The AMUSE framework	65
6.2	Bridge	66
6.3	AMUSE simulations	67
6.3.1	Pure dynamical simulations	67
7	Conclusions	73
7.1	Discussion	74
	Bibliography	77





Chapter 1

Introduction

The early evolution of the Universe, in particular the epoch of reionization and the formation of the first black holes is still not very well understood. On the theoretical side some progress has been made, however this is not very useful without the observations that could confirm or falsify these models, nevertheless these observations will become possible in the next decade thanks to the James Webb Space Telescope [1].

One of the most intriguing subjects is about the formation of Super Massive Black Holes (SMBHs) at high redshift. These astrophysical objects contain about 10^6 - $10^9 M_{\odot}$ and are found in the early and in the local Universe. For example, in the center of the Milky Way there is a SMBH with a mass of $4.5 \times 10^6 M_{\odot}$ at a distance of $R_0 = 8.4$ kpc [2, 3].

Finding these SMBHs in the local Universe is not that surprising given that they had more than 12 Gyr to grow, the intriguing issue is the presence of SMBHs at high redshift ($z \geq 6$) because these objects had less than one million years to grow.

For about a decade, the most distant Quasar known was ULASJ1120+0641 at redshift $z = 7.085$. This Quasar hosts a SMBH with a mass of $M = 2.9 \times 10^9 M_{\odot}$ [4]. However, in a recent work, Bañados et al. [5] found the most distant Quasar known to date, ULAS 1342+0928 at redshift $z = 7.54$ which hosts a SMBH with $M = 8 \times 10^8 M_{\odot}$. The presence of those supermassive black holes when the Universe was only 690 Myr old ($z = 7.54$) suggests that either the first black hole seeds were as massive as $5 \times 10^5 M_{\odot}$ or that they were grown incredibly fast, either by accreting the surrounding gas at super-Eddington rates or by merging thousands of smaller black holes, or probably, a combination of both processes.

1.1 Formation of Black Holes at high redshift

The most promising mechanism to explain SMBHs at high redshift is the so-called Direct Collapse (DC) [6, 7, 8], and consists in the formation of a very massive black hole seed with a mass $M_{\text{seed}} \sim 10^5 M_{\odot}$. This scenario is only possible if the main cooling mechanism during the collapse of a massive gas cloud ($M_{\text{cloud}} \sim 10^6 - 10^8 M_{\odot}$) is suppressed.

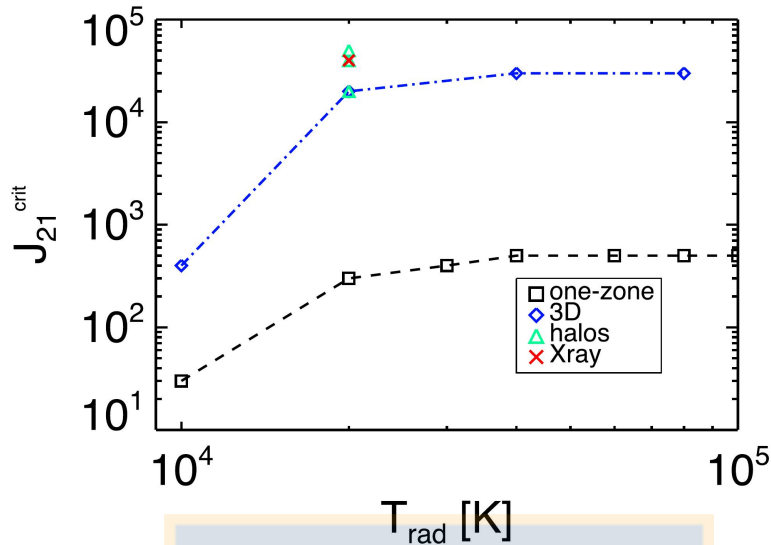


Figure 1.1: Conditions for the direct collapse scenario. Radiation flux required to destroy and suppress the formation of H_2 molecules in a $10^7 M_{\odot}$ gas cloud. One zone and 3D models are presented, along with a red cross showing the results of including an X-Ray background which makes little difference. Source: Latif et al. 2015[9].

In the early Universe, massive gas clouds collapse due to H_2 rovibrational cooling, however if H_2 is dissociated, the only cooling mechanism is through $\text{Ly}\alpha$ emission of atomic hydrogen, but the cooling is less efficient and the cloud reaches temperatures of the order of 10^4 K collapsing isothermally without fragmentation, and leading to the formation of a $0.01 M_{\odot}$ protostar which grows with an accretion rate of $\dot{M} = 0.1 - 1 M_{\odot} \text{ yr}^{-1}$. The main problem with this process is that it requires a very high UV flux in order to dissociate H_2 and to prevent further formation. The required flux is often expressed in units of $J_{21} = 10^{-21} \text{ erg cm}^{-2} \text{ s}^{-1} \text{ Hz}^{-1} \text{ sr}^{-1}$ and recent studies have found that this scenario is possible if $J_{21} \sim 10^4$ [9](see Fig. 1.1).

Such a high UV flux is conceivable only in the close vicinity (~ 10 kpc) of a star-forming galaxy and most of the closest stars must be Population II stars, given that they emit more photons than Population III (Pop. III) stars with approximately the same energy required to dissociate H_2 and to detach electrons from H^- which is the main formation channel of H_2 . These special conditions make this scenario a very rare and special one, and it is thus very unlikely that all the observed SMBHs at $z \lesssim 6$ were formed this way.

An alternative path to form very massive black hole seeds is the collapse of massive Pop. III stars which are more massive than present day stars because they were formed in a low metallicity environment where the gas cooling was much less efficient. This leads to a larger Jean's Mass of the order of $100 M_{\odot}$ which in turn produces stars with masses

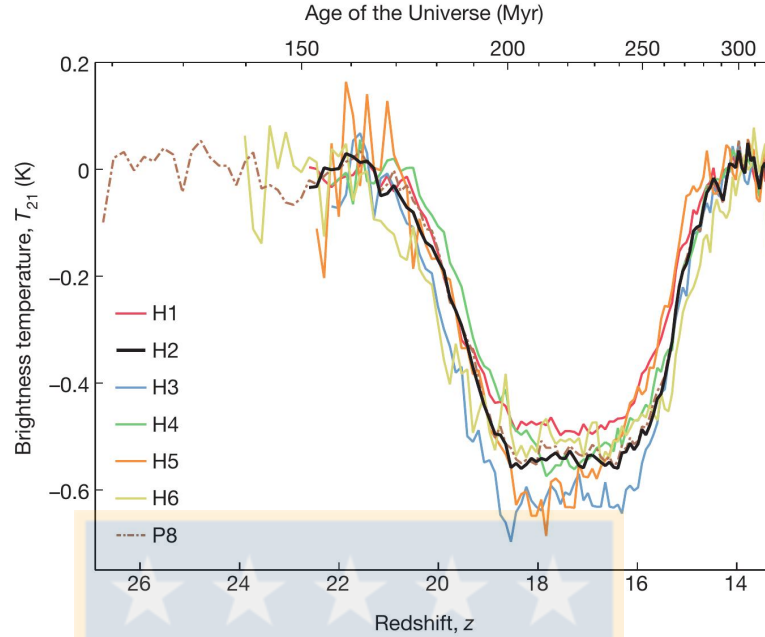


Figure 1.2: Possible detection of the first stars. Absorption profile of the 21 cm line plotted against the redshift and the age of the Universe. The absorption is due to the spin flip of the electron in the H atoms of the gas that is in the surroundings of the first stars. The original absorption profile is a single line but looks like a wide absorption signal due to absorption at slightly different epochs. The redshift is due to the expansion of the Universe and the profile is detected by different hardware configurations. The black solid line is the best fit for the hardware and software configurations which yields the best signal-to-noise ratio. Source: Bowman et al. 2018[10].

in this range. For this reason the expected black hole masses of collapsed Pop. III stars are around 20-50 M_{\odot} . Dedicated radio observations seem to have detected the footprint that these stars leave on the cosmic gas, and the detection agrees with existing models for their formation and characteristics, however the amplitude of the signal was higher than expected (see Fig. 1.2). A diagram showing the different paths for the formation of massive black holes in the early Universe is presented in Fig. 1.3.

1.2 Formation of the first stars

The first stars of the Universe were much more massive than present day stars, however the formation of such massive stars is not completely understood yet, moreover the existence of the most massive stars discovered to date cannot fully be explained. Some examples are the VFTS 682 Star with 150 M_{\odot} [12] and R136a1 with 315 M_{\odot} [13].

In the early Universe, the gas from which the first stars were formed was composed

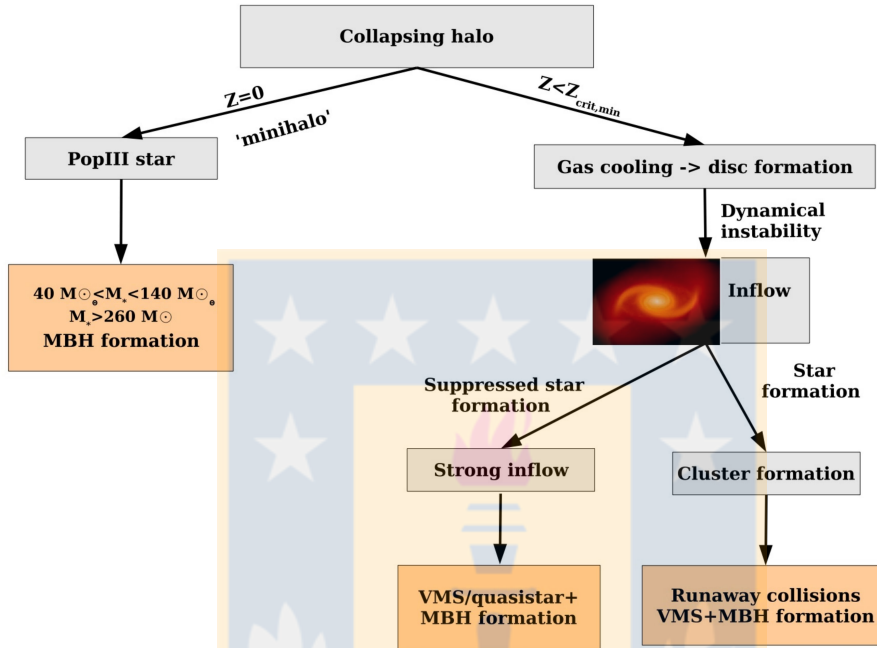
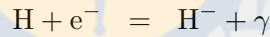


Figure 1.3: Three different paths for forming massive black hole seeds in the early Universe. The path in the left represents the collapse of the first generation of stars which emerged from gas with the abundances expected after recombination ($Z=0$). On the right, the other possible path requires the presence of few metals ($Z < Z_{crit}$) in a gas cloud that will form a disc as it cools and then a star cluster may be formed which will experience a runaway collision process producing a massive star or black hole, or, alternatively, if the star formation is suppressed, a strong inflow of gas is expected at the center of the cloud originating a super massive star or an IMBH. Source: Volonteri 2010[11].

mainly of hydrogen and helium and the main cooling mechanism was molecular hydrogen cooling. This means that the cooling was less efficient than in the present day Universe where metals and dust are present. The temperature of the gas in the star forming regions of the early Universe was about 300 K, whereas the molecular clouds of the present day Universe have a temperature of about 10 K. Due to these high temperatures, the thermal pressure in the gas, and, therefore the Jeans mass of the fragments were enhanced by a factor of about 100. Today the typical stellar mass is $1 M_{\odot}$, therefore we could expect that in the early universe the typical stellar mass was $100 M_{\odot}$.

Another important process occurring in protostars is the mass accretion, which is expected to be very high in the early Universe [14] [15], and this parameter may determine if a protostar becomes a high mass star. According to Hosokawa et al.[16], the formation of massive stars by accretion requires an accretion rate of $\dot{M}_* > 10^{-4} M_{\odot} \text{ yr}^{-1}$ to overcome the radiation pressure from the forming star in order to keep accreting mass once the star has ignited hydrogen in the core.

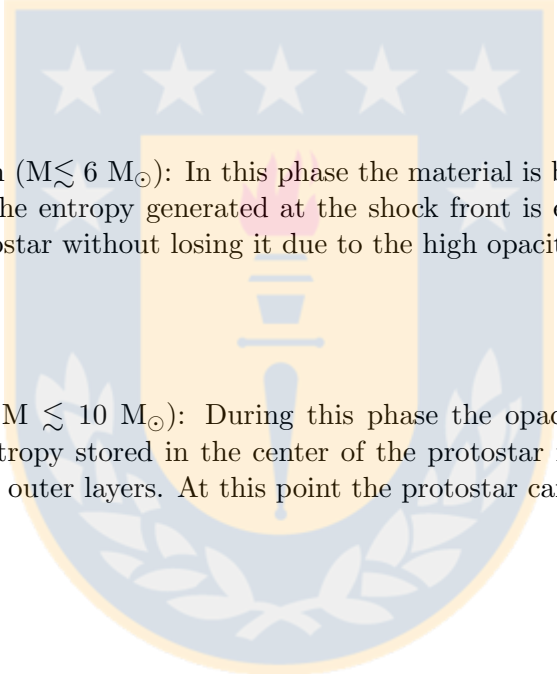
The first stars formed in the Universe, the Pop. III stars, were assembled in dark matter minihalos with masses around $10^5 - 10^6 M_{\odot}$ at redshift $z \sim 20-25$ [17]. In a recent study using interferometry to detect the absorption profile of the redshifted 21 cm line of the atomic hydrogen, Bowman et al.[10] found evidence that the first stars existed between redshift $z \sim 15-20$, even though the amplitude of the signal was higher than expected, the observation is consistent with actual models for the formation of the first stars in primordial gas clouds which are formed mainly of atomic hydrogen, and had virial temperatures around 1000 K. Trace amounts of H_2 in these clouds triggers the cooling and therefore the collapse of the cloud [18]. H_2 is formed in the cloud via two reactions:



The first reaction is the capture of one electron by atomic hydrogen. In the early Universe these free electrons are the ones remaining in the gas after recombination. The cooling of the gas is due to rovibrational emission of H_2 , and the gas can be cooled down to temperatures around 300 K and densities of $n \sim 10^4 \text{ cm}^{-3}$. At this density and temperature, the gas fragments and forms clumps of gas with masses of the order of the Jeans mass $M_J \sim 1000 M_{\odot}$. These fragments will undergo further collapse until densities of the order of $n \sim 10^{14} - 10^{16} \text{ cm}^{-3}$ (Yoshida et al.[19]). At this stage, three-body reactions form H_2 , and cause the cloud to become fully molecular, moreover, the gas becomes optically thick to molecular hydrogen cooling and the energy remains trapped in the cloud, which in turn, rises the temperature of the gas until the formation of a protostar [20].

Numerical simulations using Adaptive Mesh Refinement (AMR) or Smoothed Particle Hydrodynamics (SPH) following the collapse of such clouds have found no evidence for fragmentation until these densities (Abel et al.[21]; Yoshida et al.[15, 19]). Therefore we expect the formation of a protostar with a mass $M_{\text{protostar}} \sim 0.01 M_{\odot}$ but the accretion rates at this stage can be very high $\dot{M} \sim c_s^3 \sim 10^{-3} - 10^{-2} M_{\odot} \text{ yr}^{-1}$ (Abel et al.[21], Yoshida et al.[15]).

In a study by Hosokawa & Omukai[16] about stellar evolution of accreting protostars with accretion rates $\dot{M} \sim 10^{-6} - 6 \times 10^{-3} M_{\odot} \text{ yr}^{-1}$, they solve the equations governing the stellar structure and the accreting envelope simultaneously. They found that the evolution of a protostar accreting at $\dot{M} = 10^{-3} M_{\odot} \text{ yr}^{-1}$ is divided in four characteristics phases (see also Fig. 1.4):

- 
- Adiabatic Accretion ($M \lesssim 6 M_{\odot}$): In this phase the material is being accreted into the protostar and the entropy generated at the shock front is embedded into the interior of the protostar without losing it due to the high opacity of the gas.
 - Swelling ($6 M_{\odot} \lesssim M \lesssim 10 M_{\odot}$): During this phase the opacity of the gas decreases, and the entropy stored in the center of the protostar is released causing an expansion of the outer layers. At this point the protostar can reach a radius of $100 R_{\odot}$.
 - Kelvin-Helmholtz contraction ($10 M_{\odot} \lesssim M \lesssim 30 M_{\odot}$) with the decrease in opacity comes an expansion of the envelope of the protostar, the thermal pressure decreases and therefore a contraction will occur.
 - Main-sequence accretion ($M \gtrsim 30 M_{\odot}$) along with the contraction, the temperature of the protostar increases until reaching the temperature needed for hydrogen burning at the center, and the protostar becomes a star in the main sequence phase. Then the accretion may continue on to the protostar.

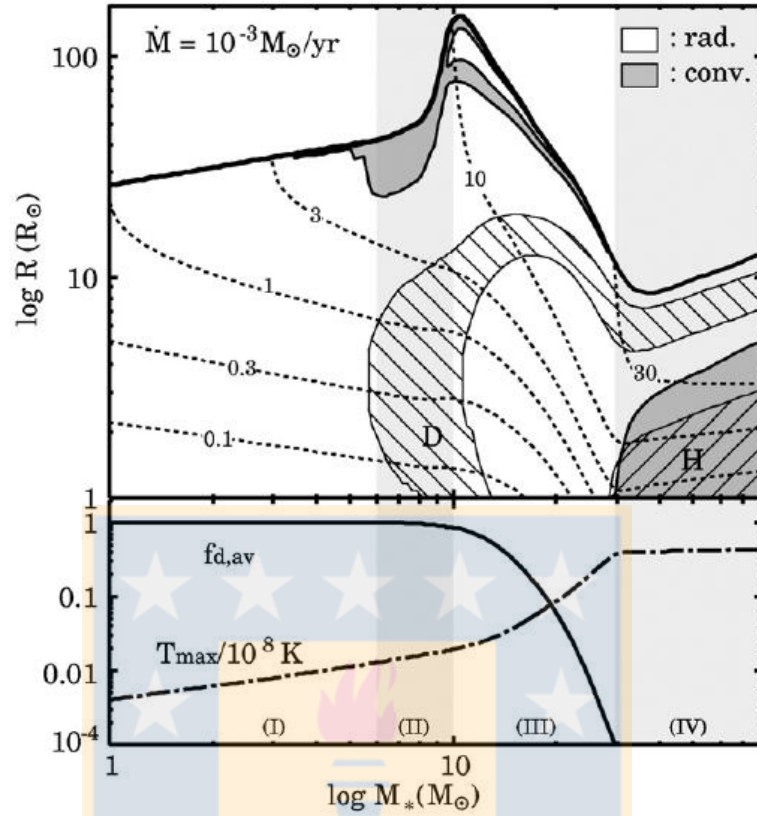


Figure 1.4: Mass and Radius evolution of a protostar accreting mass at $\dot{M} = 10^{-3} M_\odot \text{ yr}^{-1}$. The evolution is divided in four characteristics phases. Note the enhancement in radius when the protostar reaches about $10 M_\odot$. The central temperature (dashed line) is shown in the bottom panel in units of 10^8 K along with the deuterium fraction. Source: Hosokawa et al.[16]

An even higher accretion rate is possible if the main cooling mechanism is suppressed in the early stages of the cloud collapse. As shown by Latif et al.[9], a realistic model for UV and X-ray radiation from a nearby star-forming region, could dissociate and prevent the formation of H_2 molecules in primordial gas clouds, however, the required conditions are quite rare and the expected occurrence of this is relatively low. Nevertheless, if the H_2 cooling is suppressed in a cloud, we expect the only cooling mechanism to be Lyman- α transitions of atomic hydrogen, which is much less efficient in cooling the gas, and the expected temperatures are around 1000 K. A protostar formed in the center of those clouds can reach accretion rates in the order of $0.1\text{-}1 M_\odot \text{ yr}^{-1}$. Those rapidly accreting protostars can reach radius in the order of $R_{\text{protostar}} \sim 1000 R_\odot$ as shown by Hosokawa et al.[22].

1.3 Core Collapse and Stellar Collisions

Stellar collisions have been investigated before in the present day Universe as the runaway collisions scenario. Many authors find that runaway collisions occur in dense massive star clusters once these clusters undergo a process termed core collapse [23, 24, 25, 26] which is a consequence of the redistribution of kinetic energy due to close stellar encounters inside the cluster. Close to the cluster center stars are moving faster due to the deeper gravitational potential, this causes frequent close encounters between stars and some of them are thrown away from the cluster center, taking with them some kinetic energy from the stars in the core. As the stars are left with less kinetic energy in the cluster center, they will fall deeper in the potential well and this effect can be seen at large scales as a collapse of the cluster core.

The core collapse time scale is related to the cluster relaxation time or dynamical time scale. This is the time required for a star with a typical velocity to cross the system. In practice, the typical velocity is taken to be the root-mean square of the velocity of the stars. The dynamical time scale for a system in virial equilibrium is defined as:

$$t_{\text{dyn}} = \sqrt{\frac{R_{\text{vir}}^3}{GM}}, \quad (1.1)$$

where R_{vir} is the virial radius of the cluster, M is the total mass of the cluster and G is the gravitational constant. This is the time scale on which virial equilibrium and stable stellar orbits are established. Another important time scale for gravitating systems is the relaxation time scale t_{relax} , related to changes in global parameters of the cluster like orbital parameters of the stars. Relaxation is driven by two body encounters which causes a redistribution of energy in the system. For a system containing identical particles, the relaxation time scale is defined as [25]:

$$t_{\text{relax}} = \frac{0.065 \langle v^2 \rangle^{3/2}}{nm^2 G^2 \ln \Lambda}, \quad (1.2)$$

where n is the number density of stars, m is the mass of one star and Λ is the ratio between the size of the system and the distance at which an encounter would result in a 90 degree deflection of the two stars. For N identical particles, $\Lambda = \gamma N$ with $\gamma = 0.4$ [25], while for more realistic systems Giersz and Heggie [27] found $\gamma = 0.11$. A common measure for the relaxation time of a cluster is the half-mass relaxation time scale, which is obtained replacing all quantities in Eq. (1.2) by their global averages and assuming virial equilibrium:

$$t_{\text{rh}} = 0.138 \frac{N}{\ln \gamma N} t_{\text{dyn}}. \quad (1.3)$$

Numerical experiments find that core collapse is expected to occur at about 20 t_{rh} [28] but this also depends on the fraction of primordial binaries in the cluster.

Binary systems play an important role during the collapse phase and re-expansion of the core in the post-collapse phase. It has been shown that binary stars may fall to the cluster center through the effects of dynamical friction, as these systems are more massive than single stars; moreover, the interaction between binary and single stars causes the binary system to become more tightly bound, and this effect, instead of releasing kinetic energy from the core, creates hard binaries. For that reason, this mechanism delays core collapse [29, 30].

On the other hand, dynamical friction of single massive stars usually occurs faster than the core collapse time. A clear signature of core collapse is the presence of a power-law cusp in the surface brightness of a star cluster, an example of a core collapsed cluster is *Messier 15* which also shows x-ray sources close to its center [31].

1.4 Previous Work

1.4.1 Stellar collisions in previous studies

Star clusters that undergo core-collapse are expected to produce the so-called “runaway collisions scenario”, this is, a single star which experiences most of the collisions and grows exponentially in mass during the core collapse process [32, 33, 34]. Stellar collisions have been suggested as the origin of the brightest supernova SN2006gy [35] given that its exceptional luminosity must have been due to the explosion of a massive star with $M > 100 M_{\odot}$ [36]. If this is correct, after the fade of the supernova, a dense star cluster should be visible. Stellar collisions are also invoked to explain the lack of massive stars in the IMF of the Orion Nebula Cluster (ONC) given that massive stars have a larger probability to merge in the center of dense star clusters due to dynamical friction and the larger radius of these stars. If the cluster was denser in the past and stellar collisions created a big black hole with $M > 100 M_{\odot}$, this could be the reason for the large velocity dispersion of the four Trapezium stars [37].

Further studies of stellar collisions during the early stages of a star cluster evolution have shown that the fraction of collisions (i.e. total number of collisions divided by the initial number of stars) is around 1% even for very dense star clusters with a half mass radius $R_h \leq 0.1$ pc. Baumgardt and Klessen [38] performed N -body simulations of embedded star clusters with a Kroupa IMF with limits of $0.1 M_{\odot}$ and $15 M_{\odot}$ in order to assess the role of stellar collisions in the formation of massive stars, however, as can be seen in Fig. 1.5 the fraction of collisions is around 1% even for dense clusters with initial binaries.

On the other hand, Moeckel and Clarke [39] also performed N -body simulations of embedded star clusters, modeling the gas as an analytic potential with a Plummer density profile. The initial mass function is a simple power law $\eta(m) \propto m^{-2-35}$ and the limits are 0.03 - $30 M_{\odot}$, the gas is instantaneously expelled once the stars have enhanced their mass by a factor of 10 due to accretion. By including gas accretion onto the stars, the core collapse phase is not only a consequence of dynamical evolution of the cluster but instead is also caused by the mass growth of the stars, and the gas is expelled when the

cluster has passed the core collapse phase or shortly before. The deeper core collapse due to the gas potential and the accretion of the stars nevertheless produces a total of 2.5×10^{-3} % of colliding stars, using 32000 particles in a very compact cluster with a half-mass radius $R_h = 0.14$ pc (see [39], their Table 1.).

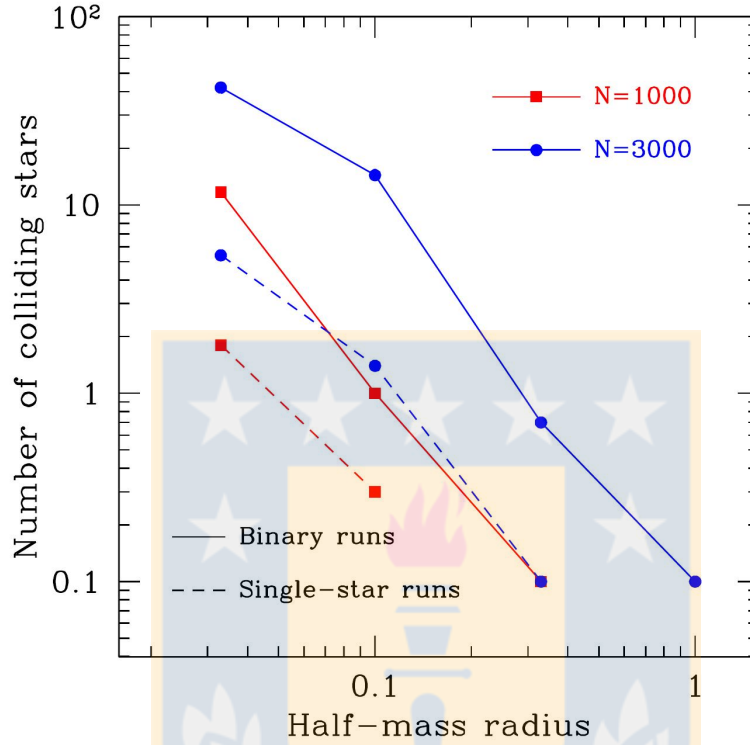


Figure 1.5: Total number of collisions in a star cluster for different initial half mass radius and different initial number of stars. Simulations with an initial binary population are shown also, and clearly they produce more collision. Source: Baumgardt and Klessen 2011 [38].

1.4.2 Stellar collisions in the early Universe

In a more recent study Sakurai et al.[40] performed cosmological simulations to reproduce the initial conditions of a collapsing gas cloud. They then replaced a fraction of the gas particles depending on the Star Formation Efficiency (SFE) to produce star clusters with $M_{\text{cluster}} = 10^5 M_{\odot}$. They assumed a metallicity $Z \sim 10^{-4} Z_{\odot}$ which is expected for the formation of second generation stars, when the environment has already been polluted by stellar winds and supernova explosions from Pop. III stars. At this metallicity, fragmentation is expected to occur at densities $n_H \sim 10^7 \text{ cm}^{-3}$ which is the central gas density of the cloud at the moment when they replace the gas particles by a star cluster (see their Fig. 1). The dynamical evolution of the cluster is performed with the hybrid

N-body code BRIDGE (Fujii et al.[41]). They produce star clusters with $R_h \sim 1$ pc, with $N = 5000 - 20000$ particles and adopt a power law Initial Mass Function (IMF) given by $\eta(m) \propto m^{-2.35}$ with masses in the range 3-100 M_\odot . They show that massive black holes with masses several times $10^4 M_\odot$ can be formed.

Our study is focused on the star clusters made up of stars formed out of a gas cloud with metallicity $Z < 10^{-5}$. At this low metallicities fragmentation is suppressed until densities $n_h \geq 10^9 \text{ cm}^{-3}$ and we expect a smaller number of objects but with higher masses (Clark, Glover & Klessen[42]) consistent with a flat IMF. Moreover if a sub-turbulent motion is present during the formation of the stars, fragmentation is expected to occur at densities $n_h \sim 10^{11} \text{ cm}^{-3}$ in the disk formed around the first protostar, and an enhancement in the number of objects is expected for turbulence in the order of $\delta v_c \sim 0.4$ (Clark et al.[43]).





NBODY6

2.1 General overview

To integrate the motion of the particles in our star clusters, we use the code NBODY6 [44].

NBODY6 uses a Hermite integrator method, which is a fourth-order predictor corrector method and allows the use of a longer time-step than the individual time-step scheme to get the same accuracy [45]. We briefly describe here some of the features of NBODY6 based on the user manual of the code, written by Sverre Aarseth [46].

2.2 The Hermite integrator method

Each particle is described by its position \mathbf{r}_0 , velocity \mathbf{v}_0 and mass m at time t_0 . The acceleration and its time derivative for each particle due to all other particles are given by:

$$\mathbf{a}_{0,i} = - \sum_{i \neq j} Gm_j \frac{\mathbf{R}}{R^3}, \quad (2.1)$$

$$\dot{\mathbf{a}}_{0,i} = - \sum_{i \neq j} Gm_j \left[\frac{\mathbf{V}}{R^3} + \frac{3\mathbf{R}(\mathbf{V} \cdot \mathbf{R})}{R^5} \right], \quad (2.2)$$

where G is the gravitational constant; $\mathbf{R} = \mathbf{r}_{0,i} - \mathbf{r}_{0,j}$ and $R = |\mathbf{r}_{0,i} - \mathbf{r}_{0,j}|$.

This method first predicts a new position and velocity for the next time-step with a Taylor series for r_i and v_i

$$r_{p,i} = r_0 + v_0(t - t_0) + a_{0,i} \frac{(t - t_0)^2}{2} + \dot{a}_{0,i} \frac{(t - t_0)^3}{6}, \quad (2.3)$$

$$v_{p,i} = v_0 + a_{0,i}(t - t_0) + a_{0,i} \frac{(t - t_0)^2}{2}. \quad (2.4)$$

The improvement of the Hermite interpolation is to approximate the higher acceleration terms by another Taylor series:

$$a_i = a_{0,i} + a_{0,i} \dot{}(t - t_0) + \frac{1}{2} a_{0,i}^{(2)} \cdot (t - t_0)^2 + \frac{1}{6} a_{0,i}^{(3)} \cdot (t - t_0)^3, \quad (2.5)$$

$$\dot{a}_i = \dot{a}_{0,i} + a_{0,i}^{(2)} \cdot (t - t_0) + \frac{1}{2} a_{0,i}^{(3)} \cdot (t - t_0)^2. \quad (2.6)$$

We don't know the derivatives $a_{0,i}^{(2)}$ nor $a_{0,i}^{(3)}$, however, we can calculate $a_{p,i}$ and $\dot{a}_{p,i}$ by using Eq. (2.1) and Eq. (2.2) with the predicted values of $r_{p,i}$ and $v_{p,i}$ calculated from the initial values using Eq. (2.3) and Eq. (2.4). Once we have $a_{p,i}$ and $\dot{a}_{p,i}$ we replace them in the right-hand side of Eq. (2.5) and is easy to show that:

$$a_{0,i}^{(3)} = 12 \frac{a_{0,i} - a_{p,i}}{(t - t_0)^3} + 6 \frac{\dot{a}_{0,i} + \dot{a}_{p,i}}{(t - t_0)^2}, \quad (2.7)$$

$$a_{0,i}^{(2)} = -6 \frac{a_{0,i} - a_{p,i}}{(t - t_0)^2} - 2 \frac{2\dot{a}_{0,i} + \dot{a}_{p,i}}{t - t_0}. \quad (2.8)$$

Now if we extend Eqs. (2.3) and (2.4) by two more orders we find:

$$r_{1,i}(t) = r_{p,i}(t) + a_{0,i}^{(2)} \frac{(t - t_0)^4}{24} + a_{0,i}^{(3)} \frac{(t - t_0)^5}{120}, \quad (2.9)$$

$$v_{1,t} = v_{p,i}(t) + a_{0,i}^{(2)} \frac{(t - t_0)^3}{6} + a_{0,i}^{(3)} \frac{(t - t_0)^4}{24}. \quad (2.10)$$

The high-order accelerations are found using the low terms for r_0 and r_p but deriving only for the first derivative. The local error in r and v within the two time-steps $\Delta t = t_1 - t_0$ is expected to be of order $\vartheta(\Delta t^5)$, and the global error for a fixed physical integrator time, scales with $\vartheta(\Delta t^4)$.

2.3 Speeding up routines

2.3.1 Block and individual time-steps

It is widely known that in stellar systems there is a big range of time scales, while in systems like binary stars the orbital periods are of the order of some days, the relaxation time of a star cluster can be in the order of hundred of millions or even billions of years.

In this sense one may ask: What is the optimal time-step for evolving such systems? The answer is that different time-steps must be used to evolve different particles depending on the fluctuations of the force acting on them. If one uses a very small time-step then two-body interactions can be integrated accurately, however, the evolution of the entire system will be very time-consuming and even an impossible task for most of the computers available today. On the other hand, choosing a larger time-step could lead to an inadequate treatment of close encounters. To overcome this problem, NBODY6 makes use of the “individual time-step scheme” [47]. The idea of this solution is that particles in regions where the changes of the forces are relatively large, are integrated with small time-steps, while particles in regions of slowly changing relative forces, are allowed to move a larger distance before recomputing becomes necessary.

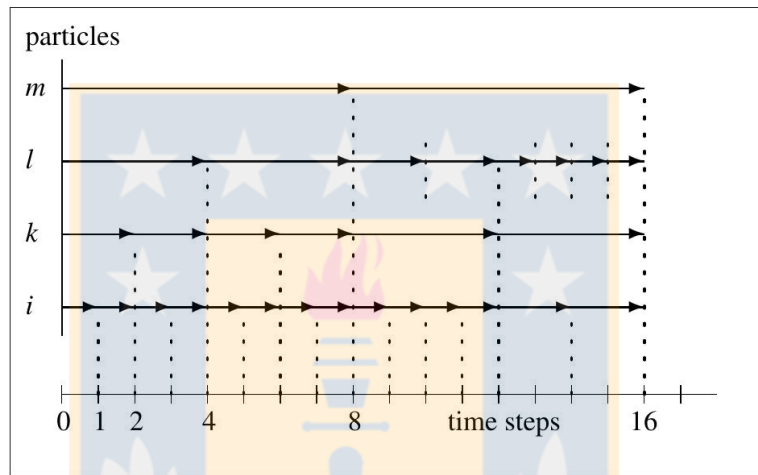


Figure 2.1: Block time-step scheme of NBODY6. Source: NBODY6 User Manual[46]

NBODY6 assigns each particle its own time-step Δt_i as shown in Figure 2.1 where particle k has a time-step which is twice the time-step for the particle i , also particle l has a time-step which is $\Delta t_l = 4\Delta t_i$. A full force calculation is done at the dotted lines, whereas at odd time-steps an extrapolation is made for particles with longer time-steps. The step-width can be altered after a full-force calculation as shown in Fig. 2.1 where we see that the time-step for particle k is doubled after 8 time-steps of the particle i . The time-step has to stay commensurable with each other’s particle’s time-step and the total time to guarantee a hierarchy. This is the block step scheme.

A first estimate for the time-step of a particle comes from the rate of change of acceleration $\Delta t_i \propto \sqrt{a_i/\dot{a}_i}$, however, after some experimentation the next formula was adopted:

$$\Delta t_i = \sqrt{\eta \frac{|a_{1,i}| |a_{1,i}^{(2)}| + |a_{1,i}|^2}{|a_{1,i}| |a_{1,i}^{(3)}| + |a_{1,i}^{(2)}|^2}} \quad (2.11)$$

Where η is a dimensionless accuracy parameter which controls the error. In most applications it's taken to be $\eta \approx 0.01$ to 0.02 .

2.3.2 The Ahmad-Cohen scheme

Even if the code can reach high precision in the calculation of the positions and velocities of each particle, the full calculation of $a_{0,i}$ and $\dot{a}_{0,i}$ Eq. (2.1) and Eq. (2.2) for each particle due to the contribution of all the other particles is very time-consuming, especially if the simulation requires large N . Therefore is desirable to implement a method to speed up this calculation while maintaining the collisional approach. In this way the method suggested by [48] is used in NBODY6.

The idea of this scheme is to split the force polynomial in Eq. (2.5) on a given particle i into two parts, a regular and an irregular component:

$$a_i = a_{i,irr} + a_{i,reg}. \quad (2.12)$$

The irregular acceleration results from particles that are close to the actual particle, this is, in a certain neighborhood of i . As this particles are close, they give rise to a stronger fluctuating gravitational force, therefore, this calculation must be done more frequently than the acceleration coming from particles that are more distant to i since they do not change too much their relative position with respect to i so quickly. The full summation in Eq. (2.1) can be replaced by a summation over the N_{nb} nearest particles and add a distant contribution from all the other particles, this contribution is updated using another Taylor series after calculating the force from the regular component FR and its time derivative FRDOT at the last regular force computation. To determine from which particles the irregular force FIRR must be calculated, NBODY6 uses a distance criterion, all the particles inside a sphere (“Neighbour Sphere” with radius r_s) are held in a list, which is modified at the end of each “regular time-step” when a total force summation is carried out.

We can summarize the procedure as follows: First, at the beginning of the force calculation, a list of neighbour objects is created around a particle i and the irregular component $a_{i,irr}$ is calculated from the list, then the summation is continued to the distant objects to obtain $a_{i,reg}$. The time derivatives of both forces is also calculated and from equation (2.5) the position and velocity of the particle are predicted. Then at time $t_{1,irr}$ the corrector is applied only for $a_{i,irr}$ from the neighbours and the regular component $a_{i,reg}$ is obtained by extrapolation, next, at the next irregular time-step $t_{2,irr}$ again the predictor-corrector method proceeds for the neighbour particles whereas the regular force term correction is still neglected. Finally, when t_1 is reached, the total force is calculated using the Hermite predictor-corrector method and a new list of neighbour objects is constructed. NBODY6 calculates at certain times only the forces of neighbours (irregular time-step, t_{irr}), while at other times both forces from neighbor and distant particles are computed, this leads to a significant gain in efficiency.

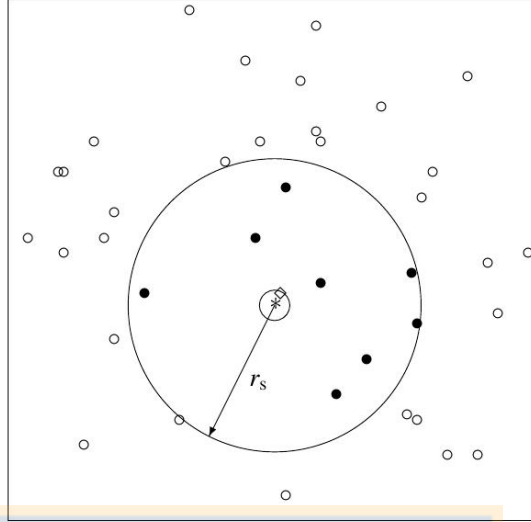


Figure 2.2: Illustration of the Ahmad-Cohen scheme. Here is shown with a cross a particle and its neighbour sphere with a radius r_s . Black dots are particles inside the neighbour radius. Source: NBODY6 User Manual [46]

2.3.3 KS Regularization

One of the most expensive calculations, especially in star clusters, is the treatment of close encounters and binary systems due to the small time-steps and small distances involved in such calculations. An accurate treatment of the dynamics of very close systems requires distances in the order of AU which is in the order of 10^{-6} pc, much smaller than typical sizes of star cluster. On the other hand the time-step may be reduced to months or days, which is about 10^{-7} yr, and usually the evolution of star cluster is followed up to several Myr. If these systems are long-lived then a simulation containing a large number of binaries becomes extremely expensive.

A solution for this issue is the use of KS regularization, first developed by Kustaanheimo & Stiefel (1965), and implemented in N -body codes by Mikkola & Aarseth [49]. The main idea is a switch to a different coordinate system when a close encounter is found. The two close bodies are replaced by a center of mass particle and integrated separately in the new coordinate system, with the advantage that such unperturbed two-body system is accurately described by a harmonic oscillator in the new system, avoiding truncation errors due to small separations or time-steps.

Regularization is controlled by 2 input parameters, **RMIN** and **DTMIN** which refers to the distance between the two particles and their time-step, and if they are smaller than **RMIN** and **DTMIN** those particles are candidates for regularization but not regularized until they fulfill 2 more criteria:

If the particles are approaching each other ($\mathbf{R} \cdot \mathbf{V} > 0.1\sqrt{G(m_1 + m_2)\mathbf{R}}$) and their mutual force is less than 4 times the force exerted on them by the other particles

($\gamma < 0.25$), then the particles are regularized.

$$\gamma = \frac{|\mathbf{a}_{\text{pert}}| \cdot \mathbf{R}^2}{G(m_1 + m_2)}$$

The parameter deciding if a pair of particles is unperturbed is **GMIN** which is by default set to **GMIN** = 10^{-6} , and once γ falls below **GMIN** the pair is considered unperturbed.

2.4 Stellar Evolution and Collisions

2.4.1 The stellar evolution routines

The Stellar Evolution package included in NBODY6 is based on the work by Hurley, Pols and Tout [50], they used previous models to compute the evolution of stars with different masses and found fitting formulae which can return the values of luminosity, radius, T_{eff} and mass at different stages of the life of a star depending on the metallicity. The models on which these formulae are based are valid for a range of masses between 0.5 - 50 M_{\odot} and were computed for seven values of total metallicity $Z = 0.0001, 0.0003, 0.001, 0.004, 0.01, 0.02$ and 0.3. These models are very complete and follow the evolution of the stars up to the late stages of their life, including Core Helium Burning stars, Neutron stars and Black Holes.

In NBODY6, stellar collisions can only occur if the stars are first regularized (routine *ksint.f*, see Sec. 2.3.3). In that routine, the collision criteria is based on the paper by Kochanek 1992[51] who studied the tidal capture process and tidal circularization of binary systems. The criteria for collisions is as follows:

$$R_{\text{coll}} = 1.7 \left(\frac{m_1 + m_2}{2m_1} \right)^{1/3} R_1. \quad (2.13)$$

If the distance of the binary at pericentre R_p is smaller than R_{coll} then the routine *cmbody.f* is called. Within that routine there is a call to the stellar evolution routines because the new merged star must be initialized by computing a new radius and luminosity. Additionally, each star has its own evolution time that is used to accurately track the different stages of the evolution.

Due to the call to these routines, the standard treatment of collisions in NBODY6 is not appropriate for our purposes for several reasons, the most important is that these stellar evolution routines are valid for present day stars given that the range of masses and metallicity does not cover the parameter range of the first stars when the metallicity was around $Z \lesssim 10^{-6}$ and the mass was between 10 and 1000 M_{\odot} . For that reasons we switched off the stellar evolution routines in NBODY6 and instead specify explicitly the stellar mass and the stellar radius for each star.

2.4.2 Stellar collisions

A collision is detected in Nbody6 once the distance between two stars at pericenter becomes smaller than R_{coll} defined in Eq. (2.13). Then the routine to handle the collision *cmbody.f* is called and the two stars are removed from the array of particles and replaced by a new particle whose mass is the sum of the masses of the two colliding stars:

$$M_{\text{new}} = M_1 + M_2.$$

The new star is placed in the center of mass of the previous configuration and its new velocity is calculated as:

$$\mathbf{V}_{\text{new}} = \frac{M_1 \mathbf{V}_1 + M_2 \mathbf{V}_2}{M_1 + M_2}. \quad (2.14)$$

As we have switched off the stellar evolution routines, we have to set by hand the new radius of the star, and to do that, we impose the condition that the density of the stars remains constant, so the radius of the new star is:

$$R_{\text{new}} = R_1 \left(\frac{M_1 + M_2}{M_1} \right)^{1/3}. \quad (2.15)$$

2.5 Adaptation of the code

In this section we describe in detail the modifications made to the code NBODY6 in order to adapt the code to our requirements, i.e, including stellar collisions without the need to activate the stellar evolution package, which does not include a correct mass-radius relation for Pop. III stars [16, 52]. The second change is the activation of the currently suppressed routine *intide.f* which initializes equal mass and equal radii stars. We use the standard NBODY6¹ code without GPU acceleration.

2.5.1 The stellar collisions routine

Here we describe the changes we did to the routine *cmbody.f* located in the directory *Ncode*. This routine replaces two colliding stars by a new star placed in the center of mass of the previous configuration, this is written in the line 308 of the file *cmbody.f*:

```
*      Define global c.m.  coordinates & velocities from body #I1 & I2.
      ZM = BODY(I1) + BODY(I2)
      DO 12 K = 1,3
          CM(K) = (BODY(I1)*X(K,I1) + BODY(I2)*X(K,I2))/ZM
          CM(K+3) = (BODY(I1)*XDOT(K,I1) + BODY(I2)*XDOT(K,I2))/ZM
      12 CONTINUE
```

¹Webpage NBODY6: <https://www.ast.cam.ac.uk/~sverre/web/pages/nbody.htm>

The trick in this routine is what we write in the line 365:

```
RADIUS(I1)=(ZM/BODY(I1))*0.3333*RADIUS(I1)
```

This is very important, because without stellar evolution activated, the radius of the stars is not updated after the collision. Effectively, this assumes that the collision product quickly settles into a new equilibrium configuration in which the density corresponds to that of an unperturbed star of the same mass, different parameterizations are also possible to include by modifying this line.

This routine (*cmbody.f*) is called once a collision is identified in the code by any of the next routines:

- *brake4.f*
- *brake.f*
- *chrect.f*
- *circ.f*
- *ksint.f*
- *kstide.f*
- *quad.f*
- *roche.f*
- *spiral.f*
- *triple.f*
- *unpert.f*



2.5.2 Stellar collisions and regularization

We are interested in the routine *ksint.f* responsible for the integration of regularized particles [49]. This is the main routine capturing collisions since the particles are often regularized before getting closer than $R_1 + R_2$. To ensure that this occurs, the user must choose the parameter $RMIN > R_1 + R_2$ to regularize the stars before they get too close and the collision is missed. We modified this routine as follows:

- line 439: replace "IF(KZ(19).GE.3...." ---> "IF(KZ(19).GE.0"
- line 568: replace "IF(KZ(19).GE.3...." ---> "IF(KZ(19).GE.0"

With these changes, the routine *cmbody.f* can be called even if the stellar evolution package is not activated ($KZ(19) = 0$).

2.5.3 The stellar radii

As we want to avoid using the stellar evolution routines included in NBODY6 we need to explicitly define the radius of each particle. A currently suppressed routine was doing this previously in NBODY6, the routine *intide.f*. To activate this routine again we have to erase a few comments in the routine *start.f*. In this file lines 60 - 62 were commented, so we just erased the comments:

```
IF (KZ(27).GT.0) THEN
  CALL INTIDE
END IF
```

Once *intide* is activated we modified the routine as follows:

```
*   Assign individual radii for main-sequence and evolved stars.
DO 30 I = 1,N
*   Adopt a primitive scheme in case of no stellar evolution.
  IF (I.LE.IMS) THEN
    RADIUS(I) = RMS*RSTAR
    TEV(I)=10D+10
    SPIN(I)=0
    KSTAR(I)=1
  ELSE
    TEV(I)=10D+10
    SPIN(I)=0
    KSTAR(I)=1
    RADIUS(I) = REV*RSTAR
  END IF
30 CONTINUE
```

We have included the parameters $TEV(I)=10D+10$, $SPIN(I)=0$ and $KSTAR(I)=1$ for both stellar populations in this routine, however its important to note that for our simulations we use only 1 population of stars. These new parameters describe the evolutionary epoch of the stars, the rotation and the stellar type chosen to be 1 (main-sequence stars).

2.5.4 Deactivating Stellar evolution

In order to prevent the stellar evolution routines from changing any parameter of the stars, we modified the routines by writing a `return` at line 60 of the file *star.f* and at line 82 in the file *hrdiag.f*. These routines initialize the stars according to its metallicity, mass and evolutionary epoch.

2.5.5 Input File for stellar collisions with NBODY6

Here we present a template of the input file used to perform the simulations with NBODY6. This template was used for all the simulations, the only changes were the number of objects N , the maximum neighbour number $NNMAX$, the random number $NRAND$,

the initial radius of the neighbour sphere `RS0`, the mean mass `ZMBAR`, the maximum and minimum particle mass `BODY1` and `BODYN` and the parameters defining the radii of the stars `IMS`, `IEV`, `RMS` and `REV`. A detailed description of the input file is out of the scope of this thesis and we refer the reader to the NBODY6 manual for further details.

```

1 10000.0
1000 1 10 196 75 1
0.02 0.01 0.3 0.5 1.0 412.0 2.0E-01 0.14 10.0
1 1 1 0 1 0 2 0 0 0
0 0 0 0 1 0 0 0 0 0
1 0 2 0 1 2 1 0 0 0
0 0 0 0 0 0 1 0 0 0
0 0 0 1 0 0 0 0 0 0
1.0E-04 0.0001 0.2 1.0 1.0E-06 0.001
1.0 10.0 10.0 0 0 0.0001 0.0 0.0
0.5 0.0 0.0 0.0 0.125
1.0 1000 0 100.0 1.0

```

The last line of the input file correspond to the input parameters required by *intide.f*. These parameters specify the radius of a typical star in solar units `RSTAR`, the number of idealized main-sequence stars `IMS`, the number of idealized evolved stars `IEV`, the scale factor for main-sequence stars `RMS` and the scale factor for evolved stars `REV`. The input file shown here is for evolving a star cluster of 1000 equal mass ($10 M_{\odot}$) stars with equal radius ($100 R_{\odot}$) in virial equilibrium. The virial radius of the cluster is 0.14 pc, this yields a half mass radius of 0.1 pc.

The total mass is $10^4 M_{\odot}$, and the cluster is evolved up to 412 crossing times. We choose a relatively large `RMIN` in order to ensure that stars are regularized before they can become closer than $R_1 + R_2$.

Setup

To explore the effect of stellar collisions, we model a compact, gas free star cluster in virial equilibrium. We assume a star formation efficiency of 100% and the total mass of the cluster to be $10^4 M_{\odot}$. We also assume that the total metallicity at the time of formation of the cluster is $Z \leq 10^{-6}$ as this value is necessary for the formation of massive Pop. III stars (Clark, Glover & Klessen[42]). If the cooling is due to H_2 rovibrational emission or Hydrogen $Ly\alpha$ emission, then fragmentation occurs at densities of the order of $n \sim 10^9 \text{ cm}^{-3}$ or even higher. This allows the formation of very dense star clusters with a half mass radius $R_h \sim 0.1 \text{ pc}$. Thus we set the half mass radius of the cluster to be $R_h = 0.1 \text{ pc}$.

Another important aspect of the formation of a star cluster is the fragmentation process, this is crucial in determining the number of stars formed and the Initial Mass Function (IMF) of the stars. There are some studies about fragmentation in primordial gas clouds, however these studies are still somewhat incomplete, but point towards a flat IMF for a metallicity $Z \leq 10^{-6}$ (Clark, Glover & Klessen[42], Clark et al.[43]) with the total number of stars being low. However the simulations were terminated before all the gas was accreted into the stars, and for a low mass gas cloud $\sim 1000 M_{\odot}$, the total number of stars, even considering sub-sonic turbulent motions seems to be around 20.

Here we don't use an IMF and instead assume that all the stars are equal, with the same mass and radius and explore different combinations of the number of stars and the stellar radii. No stellar evolution is included in our simulations.

3.1 Simulation time

The goal of this investigation is to understand the collision process in very dense star clusters populated by very massive and big Pop. III stars. We wish to know how many collisions we can expect and how much is growing the runaway object before the cluster gets dissolved due to its natural evolution [53] or destroyed by a supernova explosion. Our simulations stops at $250 t_{\text{cross}}$ which is roughly 2 Myr. We have chosen this end-time based on the first test simulations that we ran. Essentially, stellar collisions occur very

early in the cluster, and eventually the 10 % of the total mass is gathered in a single object between 10-80 crossing times and the runaway object is formed at this time in most of the simulations. An exception is the case for $N= 5000$ stars with $R_{\text{star}} = 20 R_{\odot}$, in this case the time at which the central object has grown until the 10% of the total mass of the cluster is at $\sim 200 t_{\text{cross}}$. The runaway growth can be seen in the bottom panel of Fig. 3.1 and the moment at which the central object has gathered 10 % of the total mass can be seen in the middle panel as a shrink in the 10% Lagrangian radius, we decided to stop at $250 t_{\text{cross}}$ because the mass enhancement and the collision rate is slowing down shortly this occurs.

3.2 Parameter space

We present the main parameters of the cluster and the stars that we used in our simulations in Tab. 3.1. The first column is an identifier for the simulation, the second column shows the number of stars used to model the cluster, the third column is the total mass of the cluster, the fourth column is the half-mass radius of the cluster and the fifth and sixth columns are the mass and radius of each star. Each simulation was repeated 9 more times varying the initial random seed. This allows a better statistical analysis and error estimation. We keep the mass and the half mass radius of the cluster constant and explore the effect of using a different number N of stars with $N = 100, 500, 1000, \& 5000$ and we also vary $R_{\text{star}} = 20, 50, 100, 200, 500, 1000, \& 5000 R_{\odot}$. We performed a total of 280 simulations.

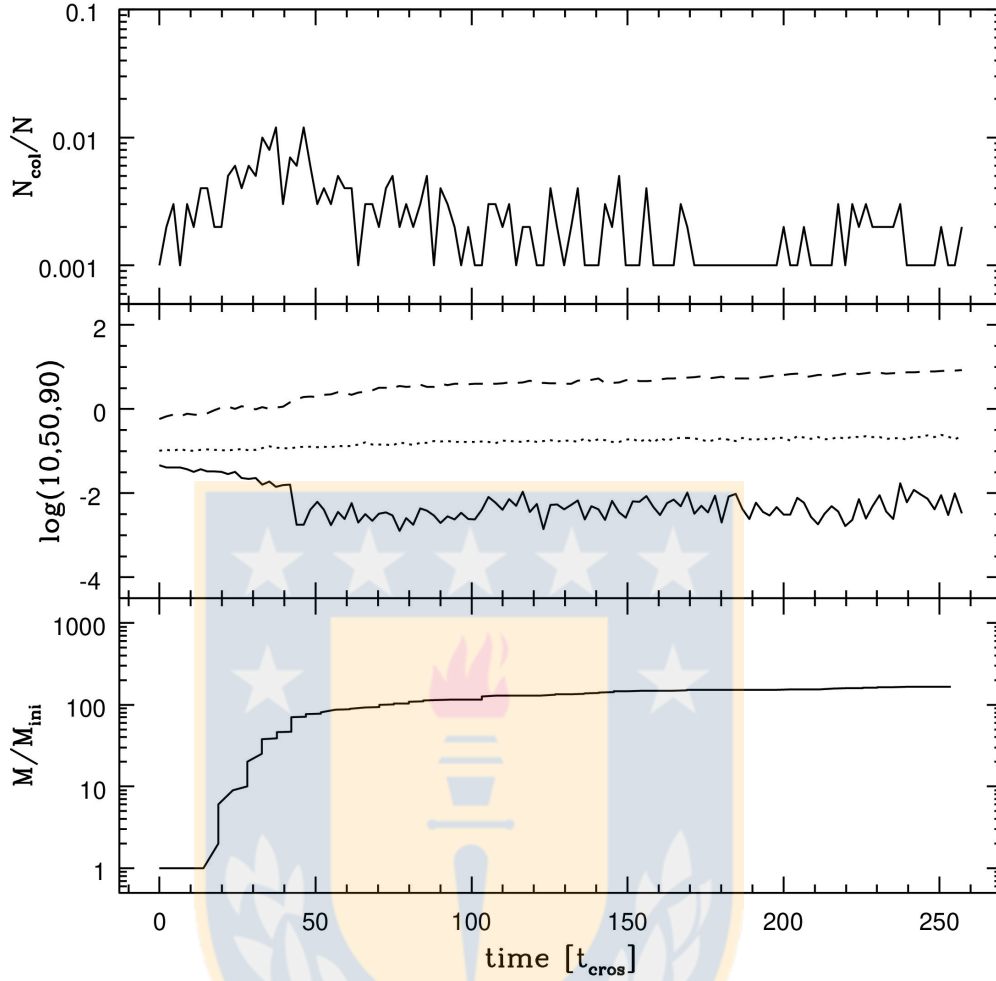


Figure 3.1: Evolution of a star cluster with 1000 stars, each one of them with an initial radius of $500 R_{\odot}$. The top panel shows the collision rate N_{coll}/N calculated in bins of 5 crossing times. Clearly this rate is maximum at the moment when the object grows up to 10% of the total mass of the cluster which is around 30-50 crossing times. The middle panel shows the evolution of the 10%, 50% and 90% Lagrangian radius and the moment when the runaway object reaches a mass of 10% of the total mass is clearly visible between 30 - 50 crossing times as a shrink in the 10% Lagrangian radius, while the half mass radius remains nearly constant but the outer part of the cluster is expanding. The bottom panel shows the evolution of the runaway object in units of the initial mass, which is $10 M_{\odot}$ for this case. The moment of exponential growth is clear around 30-50 crossing times when the central part of the cluster contracts and the collision rate is highest. Most of the collisions involve this central object which at the end dominates the cluster center. Source: Own elaboration

ID	N	$M_{c,i}$ M_{\odot}	R_h pc	M_{star} M_{\odot}	R_{star} R_{\odot}
1	100	10^4	0.1	100	20
2	100	10^4	0.1	100	50
3	100	10^4	0.1	100	100
4	100	10^4	0.1	100	200
5	100	10^4	0.1	100	500
6	100	10^4	0.1	100	1000
7	100	10^4	0.1	100	5000
8	500	10^4	0.1	20	20
9	500	10^4	0.1	20	50
10	500	10^4	0.1	20	100
11	500	10^4	0.1	20	200
12	500	10^4	0.1	20	500
13	500	10^4	0.1	20	1000
14	500	10^4	0.1	20	5000
15	1000	10^4	0.1	10	20
16	1000	10^4	0.1	10	50
17	1000	10^4	0.1	10	100
18	1000	10^4	0.1	10	200
19	1000	10^4	0.1	10	500
20	1000	10^4	0.1	10	1000
21	1000	10^4	0.1	10	5000
22	5000	10^4	0.1	2	20
23	5000	10^4	0.1	2	50
24	5000	10^4	0.1	2	100
25	5000	10^4	0.1	2	200
26	5000	10^4	0.1	2	500
27	5000	10^4	0.1	2	1000
28	5000	10^4	0.1	2	5000

Table 3.1: Initial conditions for the first set of simulations. The first column is the number of the simulation, the second columns is the total mass corresponding only to the stellar mass as these are simulations of the gas-free cluster models presented in Sec. 3. The third column is the half-mass radius of the cluster and the fourth and fifth columns are the stellar mass and the number of stars respectively. Source: Own elaboration.

Results

4.1 Evolution of the clusters

We run a few simulations first to understand the cluster evolution and the main results. We decided to stop the simulations at $t = 400 t_{\text{cross}}$ independent of the number of stars or stellar radius and look at the general evolution of some clusters to better decide a final time for stopping all the simulations.

The evolution of the clusters is very similar, and in all cases the runaway object eventually encompasses the 10% of the total mass of the cluster, we suspect that this is related to the process of core collapse (see Sec. 1.3) when the central part of the cluster contracts. This marks the moment at which the central object grows exponentially in mass due to the large number of collisions occurring at this stage, most of them with the same central object which becomes then the runaway object and gathers up to 10% of the total mass of the cluster or even more.

In order to understand how the cluster evolution influences the amount of collisions we calculate a collision rate that we define as the total number of collisions N_{coll} divided by the initial number of stars N in a given interval of time, chosen to be 5 crossing times for all the simulations. A brief discussion of how this time interval affects the results is presented in Section 4.2. In general, shortly before, during, and shortly after the 10% Lagrangian radius reaches its first minimum value, i.e., when the central object has grown up to 10% of the total mass of the cluster, probably due to the processes that leads to core collapse, the collision rate reaches its maximum value, typically, in an interval of 5 crossing times, around 0.01-0.02% of the stars of the cluster merge, and the time during which this rate is maintained depends mainly on the number of stars. Before and after this episode of frequent collisions the collision rate oscillates between 0-0.003 (see top panel of Fig. 3.1).

While for a cluster containing 1000 stars, the collision rate is of the order of 0.01-0.02 (in an interval of 5 crossing times) close to the moment at which the 10% of the total mass is contained in a single object, this value changes to 0.004-0.006 for a cluster containing

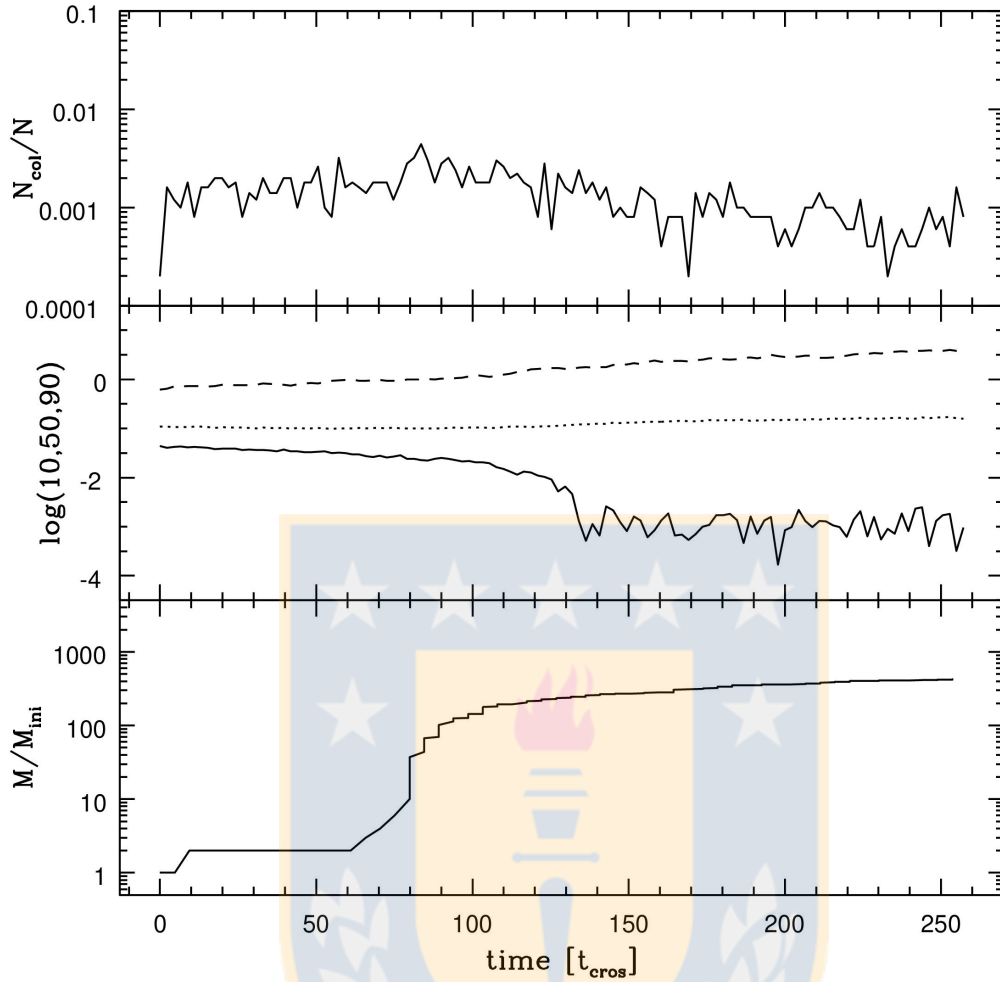


Figure 4.1: Evolution of a star cluster with 5000 stars, each one of them with an initial radius of $500 R_{\odot}$. The top panel shows the collision rate N_{coll}/N calculated in bins of 5 crossing times. The collision rate reaches the maximum value of 0.4% at around 80 crossing times, however a relatively high rate is maintained from the beginning up to 150 crossing times, shortly after 10% of the mass has been gathered in the central object. The middle panel shows the evolution of the 10%, 50% and 90% Lagrangian radii and the moment at which the runaway object encompasses the 10% of the total mass is clearly visible between 70-150 crossing times. During this period, the runaway object has grown by a factor of ~ 200 . Meanwhile the half mass radius remains nearly constant and the outer part of the cluster is expanding. The bottom panel shows the evolution of the runaway object in units of the initial mass, which is $2 M_{\odot}$ for this case. The moment of exponential growth is around 80 - 150 crossing times when the central part of the cluster contracts and the collision rate is highest. Most of the collisions involve this central object which at the end dominates the center. The period of maintained relatively high collision rate produces slightly more massive stars, which can then collide with the central object. Source: Own elaboration.

5000 stars. This difference can be explained by the factor 5 in the denominator when calculating N_{col}/N and therefore this is an indication that the number of collisions in this interval of time (5 crossing times) is very similar and not depending on the number of stars. The difference is the amount of time during which the collision rate is maintained, being longer for a larger number of stars.

4.2 Time-step for computing the collision rate

In this section we present a brief discussion on the choice of the time interval for computing the collision rate. We define the collision rate as the number of collisions divided by the initial number of stars in a given time interval Δt . We analyze a simulation of 5000 stars, each with $500 R_{\odot}$, the same that is presented in Fig. 4.1. First we use a time interval of 3 crossing times, $\Delta t = 3 t_{\text{cross}}$ and calculate the total number of collisions in this interval. For such a Δt we are close to detect 1 or 0 collisions in the time interval and obtain a more detailed description of the collision rate variation. The main features are still clearly visible, an enhancement in the collision rate at 50 - 100 t_{cross} and then a slow decrease towards the end of the simulation (see Fig. 4.2). We also show the collision rate calculated in bins of 5 crossing times in Fig. 4.3. The use of a larger bin-size for computing the collision rate gives a more general description of the collision rate variation, showing more clearly the enhancement at the moment when the cluster center shrinks (50 - 100 t_{cross}). Finally we also compare the previously calculated collision rates in intervals of 3 or 5 crossing times with the collision rates calculated in intervals of 10 crossing times, the results are presented in Fig. 4.4. We found again the same behavior, an increase between 50 - 100 crossing times and then a slow decrease towards the end. The description is now even more general, the fraction of collisions actually increases because we are including more collisions by considering a longer time interval, however the fraction of collisions per crossing time is the same. We decided to use a bin-size of 5 crossing times to describe the collision rate variations in a general way and at the same time a more detailed description than using a bin-size of 10 crossing times.

This analysis shows that our choice of the time interval does not affect our results.

4.3 Total number of collisions

We are also interested in understanding how the total number of collisions is affected by changing the total number of stars and the stellar radii. For a better comparison we plot the total fraction of collisions N_{col}/N as function of the radius of the stars R_{star} in Fig. 4.5.

We obtained the total number of collisions from the general output of NBODY6, which we called *out.txt*. As we have deactivated the stellar evolution routines now the information about collisions must be obtained from this file by doing:

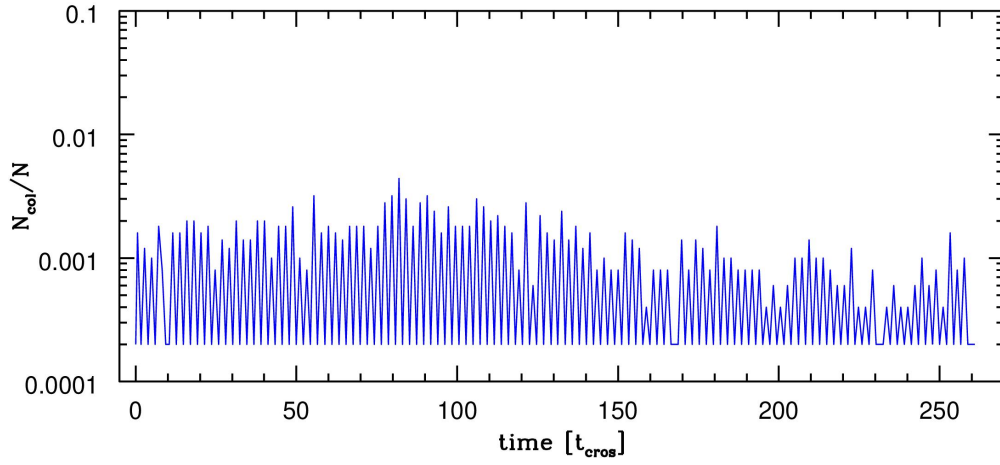


Figure 4.2: Collision rate $\frac{N_{\text{col}}}{N}$ calculated in bins of 3 crossing times for the same simulation presented in Fig. 4.1. By using a smaller bin-size we can compute more accurately the collision rate during the simulation time, however we still see the main features in which we are interested, an increase between 50 - 100 t_{cros} and a slow decrease towards the end of the simulation. Source: Own elaboration.

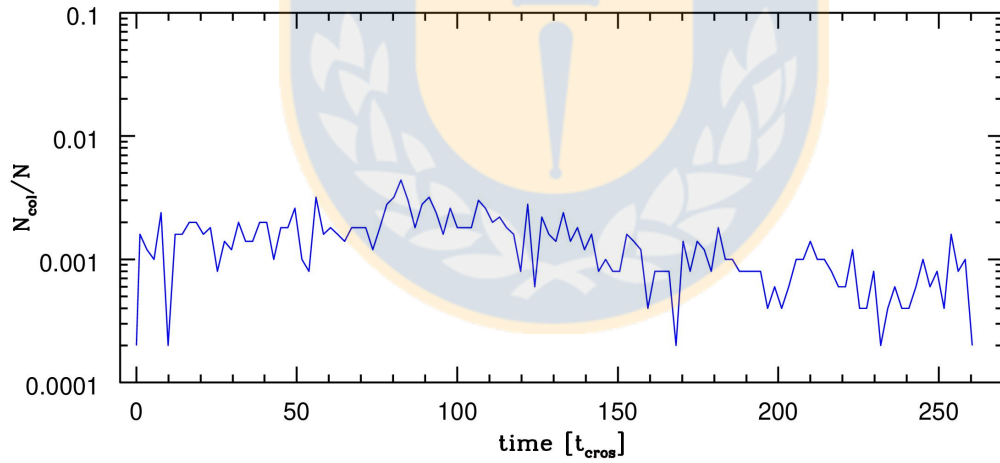


Figure 4.3: Collision rate $\frac{N_{\text{col}}}{N}$ calculated in bins of 5 crossing times for the same simulation presented in Fig. 4.1. We see now similar collision rates as by using a bin-size of 3 crossing times, but now a more general description of the collision rate is obtained. Source: Own elaboration.

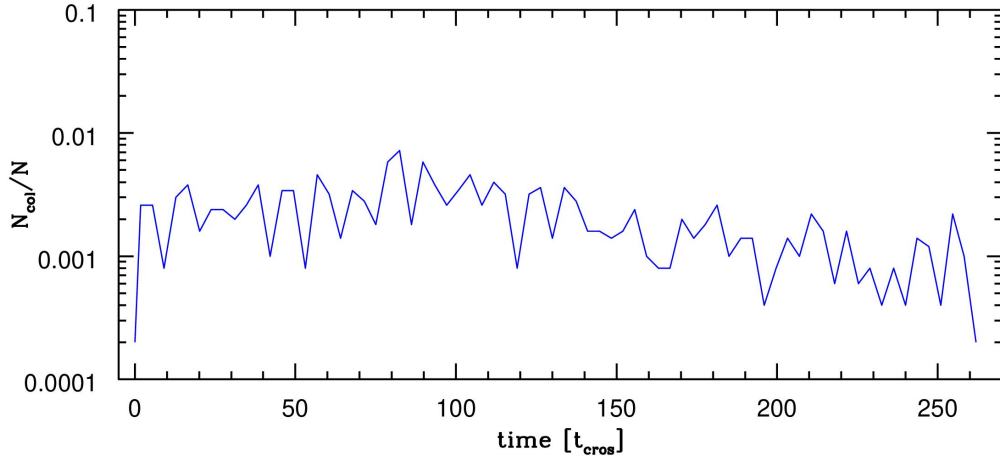


Figure 4.4: Collision rate $\frac{N_{\text{col}}}{N}$ calculated in bins of 10 crossing times for the same simulation presented in Fig. 4.1. We see now similar collision rates as by using a bin-size of 3 crossing times, but now a more general description of the collision rate is obtained. Source: Own elaboration.

```
grep -i -r 'COLLISION' out.txt >COL.dat
```

This command generates the file *COL.dat* containing important information about each collisions, the total mass of the final product, the mass of the colliding stars, the ID of the colliding stars, the time of the collisions, etc. Alternatively, one can find the number of collisions at different times in the file *fort.56* in the last column.

We simply calculate now the total number of collisions for each simulation N_{col} divided by the initial number of stars N . As we performed 10 simulations for the same combination of R_{star} and N (varying only the initial random seed) we calculated then the mean value for N_{col}/N from the 10 different results and the standard deviation as:

$$\sigma = \sqrt{\frac{\sum_{i=1}^{10} \left(\left(\frac{N_{\text{col}}}{N} \right)_i - \overline{\left(\frac{N_{\text{col}}}{N} \right)} \right)^2}{N - 1}}.$$

We found that the fraction of collisions does not depend on the number of stars used to model the star cluster but depends strongly on the radii of the stars. This is probably due to the fact that stellar collisions occur only close to the center of the cluster, therefore only the fraction of stars which is closest to the center will experience collisions. On the other hand, the probability of collisions depends also on the cross-section and increasing the stellar radius we are increasing the cross-section.

N	A	B	C	D
100	0.45 ±0.02	-2.25 ±0.06	0.40±0.04	-0.16±0.09
500	0.49 ±0.02	-2.27 ±0.06	0.53±0.04	0.22±0.09
1000	0.51±0.04	-2.29 ±0.09	0.57±0.06	0.44±0.14
5000	0.50±0.03	-2.16 ±0.07	0.52±0.05	1.28±0.12

Table 4.1: Parameters from the fit to the data presented in Fig. 4.5. Parameters from the fit to Eqs. (4.1) (Cols. 2 and 3) and (4.2) (Cols. 4 and 5) to estimate the total fraction of collisions in a cluster depending on the initial radii of the stars R_{star} and the initial number N of stars (Eq. (4.1)). Parameters D and E are used to estimate the mass of the most massive object divided by its initial mass ($M_{\text{max}}/M_{\text{ini}}$) at the end of the runaway growth, depending on the initial radii R_{star} of the stars and the initial number N of stars (Eq. (4.2)). Source: Own Elaboration.

4.3.1 Linear fit

Here we show the fraction of collisions and the enhancement of the mass of the central object as a function of the stellar radius in Fig. 4.5. The different lines are the fits to the data which we obtained with the help of *gnuplot*, using the command *fit* which uses the non-linear least-squares Marquardt-Levenberg algorithm. Once we have found, for a given number of stars N the logarithm of the mean value for the fraction of collisions $\log\left(\frac{N_{\text{col}}}{N}\right)$ as function of the logarithm of the stellar radii we fit the linear function:

$$f(x) = A \log(R_{\text{star}}) + B.$$

Now we have a function that we can use to calculate the fraction of collisions or the total number of collisions expected for a star cluster whose crossing time is $t_{\text{cros}} = 0.0078$ Myr, assuming that all the stars have the same mass and same radius R_{star} :

$$\frac{N_{\text{col}}}{N} = 10^{A \log(R_{\text{star}}) + B}. \quad (4.1)$$

The parameters A and B depend weakly on the number of stars and are presented in Tab. 4.1.

4.4 Maximum mass

We have obtained the mean maximum mass divided by the initial mass $\frac{M_{\text{max}}}{M_{\text{ini}}}$ for each combination of R_{star} and N , and also the associated error in an analog way as we did for the total fraction of collisions (see Sec. 4.3).

We can find the most massive object in each simulation by searching in the file *COL.dat*. This file was obtained as described in Sec. 4.3 and contains information about the final mass of the collision products. Once the most massive object was found, we simply divided its final mass by its initial mass. The results are presented in the bottom panel of Fig. 4.5.

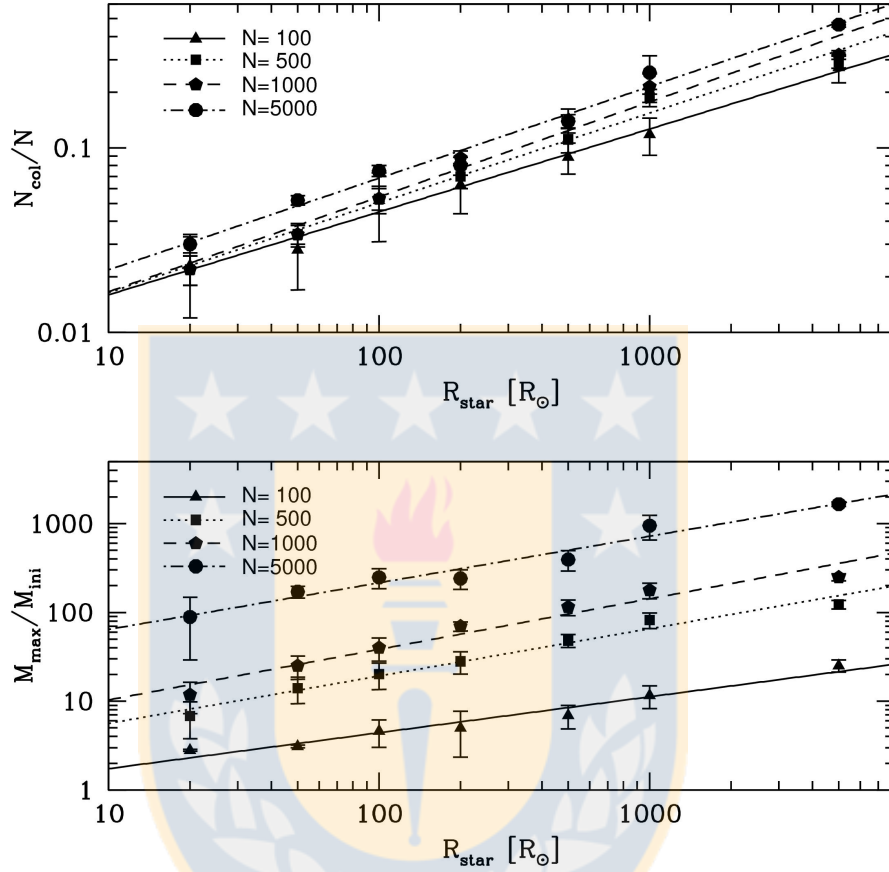


Figure 4.5: Fraction of collisions and final mass of the runaway object as function of N and R_{star} . Top panel: Mean total fraction of collisions N_{col}/N as function of the stellar radius R_{star} for star clusters with different number of stars. The different lines are the best fits to the data points. Interestingly we found that the relation between the collision fraction and the stellar radii is a power law with roughly the same slope independently of the number of stars but strongly dependent on the stellar radii. Source: Own elaboration.

Unlike for the total fraction of collisions, the maximum mass of the runaway object depends on both the initial number of stars N and the radii of the stars R_{star} . This result is more intuitive to understand, as on one hand, the number of collisions increases with increasing number of stars, and even when not all the collisions involve the runaway object, we may think that the number of collisions experienced by the runaway object to be a fraction of the total number of collisions, and naturally, increasing the number of stars also increases the maximum mass of the runaway object. On the other hand we know that an enhancement in the radii of the stars increases the number of collisions and therefore the maximum mass of the runaway object.

We did the same fit as described in Sec. 4.3.1 using the next equation:

$$\frac{M_{\text{max}}}{M_{\text{ini}}} = 10^{(C \log(R_{\text{star}}) + D)}, \quad (4.2)$$

with C and D the free parameters which vary slightly with N as can be seen in Tab. 4.1.

4.5 Number of collisions as a function of time

The previous functions we found are a useful tool to obtain a first approximation of the total number of collisions in a star cluster, depending on the number of stars and their radii (Eq. (4.1)) or additionally for calculating to a first approximation the expected mass enhancement of the runaway object (Eq. (4.2)). However we are interested in the amount of collisions or mass growth due to collisions that experiences the runaway object before it could explode as a core-collapse supernova or pair-instability supernova. An estimation of the gravitational binding energy of the clusters that we are considering is obtained following the approach for a spherical distribution:

$$U = -\frac{3GM^2}{5R},$$

with $M = 10^4 M_{\odot}$ and $R = R_{\text{vir}} = 0.14 \text{ pc}$ this yields $U = -3.8 \times 10^{49} \text{ erg}$ and according to Kasen, Woosley and Heger 2011 [54], a pair-instability supernova can produce up to 10^{53} erg , sufficient to disrupt the star cluster and halt stellar collisions.

Due to this constraint we decided to derive a function that relates the number of collisions and the time in order to be able to estimate the number of collisions experienced by the runaway object before a supernova explosion occurs inside the star cluster. In this section we describe the steps to derive this function.

4.5.1 Modeling the runaway collision process

In the top panels of Figs. 3.1 and 4.1 the clusters slowly experience the process of two-body relaxation which leads to a shrink of the central parts that can be seen as an

enhancement in the collision rate and this marks the time at which the runaway object grows rapidly in mass, then it is natural to expect also an enhancement in the number of collisions experienced by the runaway object in this time interval.

We aim now to model the expected number of collisions with the runaway object as a function of time and for this we have chosen the Gaussian function since the number of collisions at different time intervals may follow approximately a Gaussian function, especially during the moments at which the object has grown up to 10% of the total mass of the cluster as can be seen in Fig. 4.6.

Now, assuming that we can model the number of collisions depending on time as a Gaussian distribution, the total number of collisions up to a certain time t can be calculated as:

$$N_{\text{col}} = A \int_0^t \exp\left(\frac{-(t - t_{\text{delay}})^2}{2 t_{\text{duration}}^2}\right). \quad (4.3)$$

We have defined 3 parameters for the Gaussian fit: t_{delay} which is the center of the Gaussian and marks the moment at which the function reach the maximum value. This parameter can be thought as the delay time at which the runaway process occurs, or alternatively, as the time at which half of the expected number of collisions occur. The next parameter is the duration time t_{duration} analogous to the standard deviation of the Gaussian function and is related to the duration time of the runaway growth. Finally we introduced the parameter A which is a normalization parameter that we calculate in such a way that the function can reproduce accurately the total number of collisions.

4.5.2 Collisions with the runaway object

In order to apply our fitting function to the data we first have to separate the collisions which involve the runaway object. This can be determined with the help of the star's ID which is an integer number assigned to each star by NBODY6 and that is preserved during the collisions by keeping the ID of the most massive star once a collision is detected, and subsequently, the new star will conserve this ID. The ID of each star can be found, in one way, by extracting the information of collisions from the output file generated by NBODY6. In the following we will show the command that we used to extract this information. Our output file is named *out.txt* and we use `grep` and `awk` to extract the information and present it in an ordered manner to be processed afterwards. We use the next command:

```
grep -i -r 'COLLISION' out.txt | awk '{ print $3,$11,$12,$14,$15 }'
>TIMECOL.dat
```

This command generates the file *TIMECOL.dat* which contains 5 columns, the time of the collision in Myr, the ID of the first and second colliding stars and the final mass of the product (the 5th column is included for safety given that in some cases the length of the number for the mass is so large that is not separated from the "=" which is in the column 14 usually, and therefore if we just print the 15th column, we could miss this information).

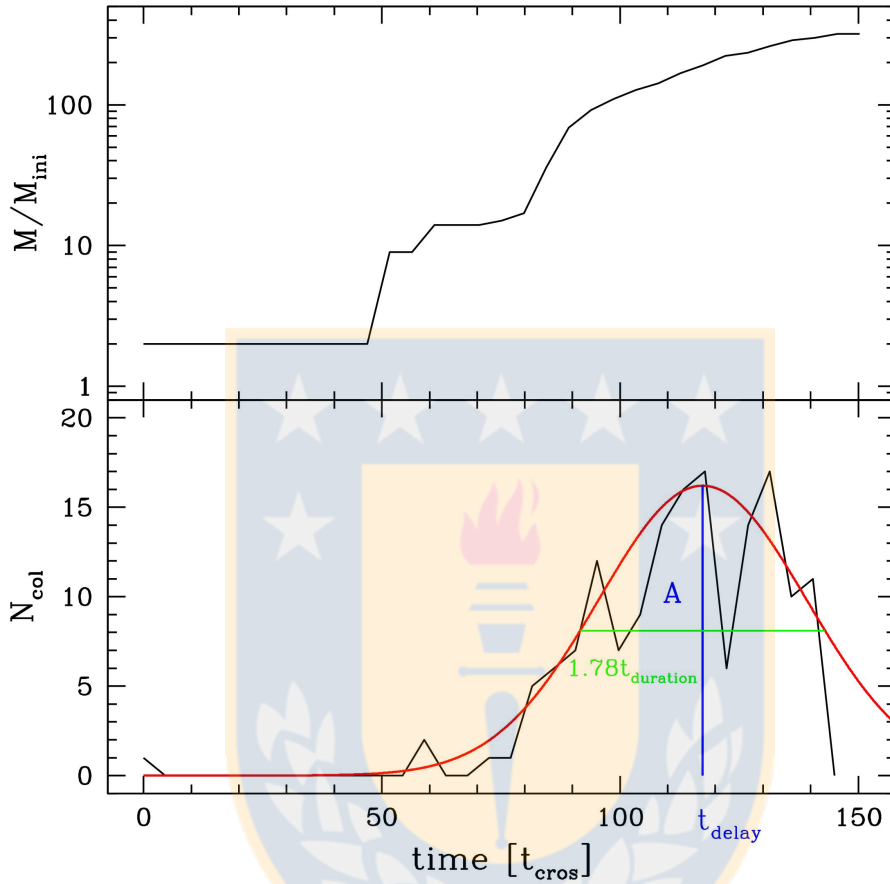


Figure 4.6: Modeling the runaway growth. Top panel: Mass growth of the runaway object in units of the initial mass M_{ini} . This simulation consist of $N = 5000$ stars, each with a mass of $M_{\text{ini}} = 2 M_{\odot}$ and a radius of $R = 200 R_{\odot}$. Bottom panel: Number of collisions with the runaway object (in bins of 5 crossing times) as a function of the crossing time of the cluster. The red line shows the best fit for a Gaussian function with the parameters A , t_{delay} and t_{duration} . Note that the peak in the number of collisions coincides with the rapid mass growth. Source: Own elaboration.

Now from this file it is easy to distinguish collisions involving the most massive object, one only needs to know the ID of the most massive object and this can be done with this same file.

4.5.3 Number of collisions per time interval

The next step is to choose a time interval for counting the number of collisions in such a period. We have chosen a time interval or bin-size of 0.1 Myr (because the information of collisions is presented in Myr) which is roughly 5 half-mass crossing times, this choice we made taking into account that a very small bin-size will show the contribution from individual collisions rather than a general description, and, on the other side, with a larger bin-size we have less points for fitting the function. Nevertheless in the following we also present a comparison of some results using different bin-sizes and show that they do not vary significantly.

We show the analysis of changing the bin-size for 1 simulation with $N=5000$ stars, each with a radius of $R=200 R_{\odot}$ and use 3 different bin-sizes, $2 t_{\text{cross}}$, $5 t_{\text{cross}}$ and $10 t_{\text{cross}}$. For the case of $2 t_{\text{cross}}$ we start to see the contribution from individual collisions and the Gaussian shape is not seen (see Fig. 4.7), however the function still reproduces the delay and duration time of the runaway collision process and the total number of collisions can be calculated if the parameter A is adjusted to reproduce that result.

For the case of $10 t_{\text{cross}}$ we obtain a more general description and the Gaussian shape is more evident now in Fig. 4.8, with a higher peak because we count more collisions and the mass growth rate could also be approximated by a Gaussian function, however we have less points to fit now and the errors for the fit are larger so we decided to use a bin-size of $5 t_{\text{cross}}$ at the end. Note that the function still can reproduce the delay time and duration of the collision process if the parameter A is tuned for this purpose, and we have included, after determining A through the linear fits, a correction which is $1/4$ for A in all the cases.

4.5.4 Simulations with few collisions

In general, the 3 parameters can be obtained after fitting the Gaussian function to the data, however, there are simulations with very few collisions. For example, for $N=100$ and $R=20 R_{\odot}$ we expect 1 or up to 3 collisions and this is not enough for fitting an accurate Gaussian function, an example of this is presented in Fig. 4.9. In this example, only 3 points are used for the fitting and the errors are too big. For the height of the Gaussian the function fit of `gnuplot` gives $A = 2.00 \pm 9.148$, $t_{\text{delay}} = 13.55 \pm 133.5$ and $t_{\text{duration}} = 1.07 \pm 31.24$. We present in the following section the way in which we solved this problem.

4.5.5 Combination of the data

In this section we describe the steps we followed in order to solve the problem of having few collisions which causes a poor fit and unreliable parameter estimations. The trick

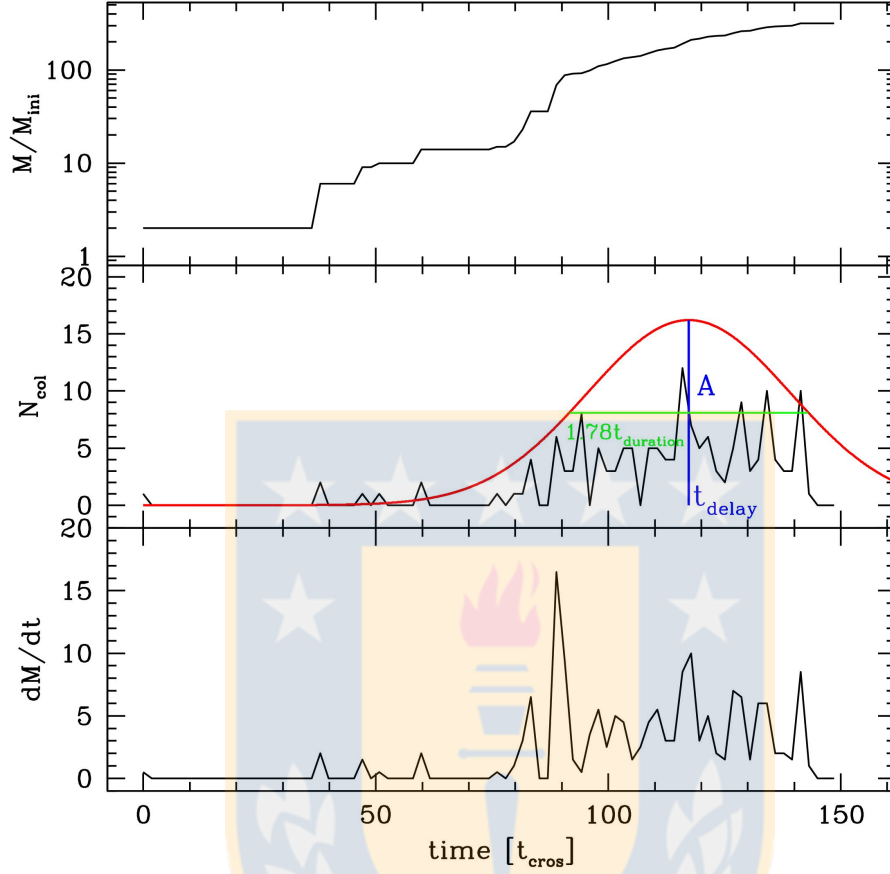


Figure 4.7: Computing the collision rate with a time interval of 2 crossing times. Top panel: Mass growth of the runaway object during the simulation in units of the initial mass M_{ini} . This simulation consists of $N = 5000$ stars, each with a mass of $M_{\text{ini}} = 2 M_{\odot}$ and a radius of $R_{\text{star}} = 200 R_{\odot}$. Middle panel: Number of collisions with the runaway object (in bins of 2 crossing times) as a function of the crossing time of the cluster. The red line shows the best fit for the data binned in $5 t_{\text{cros}}$ for comparison (see Fig. 4.6). Note that the Gaussian fit is still a good description for the time delay and duration of the runaway collision process, the parameter A may be adjusted later for a better agreement with the total number of collisions. Bottom panel: Mass growth in intervals of $2 t_{\text{cros}}$. At this time interval this plot shows the contribution from individual collisions and the highest peak is caused by the collision with another high mass object created in the cluster. Source: Own elaboration.

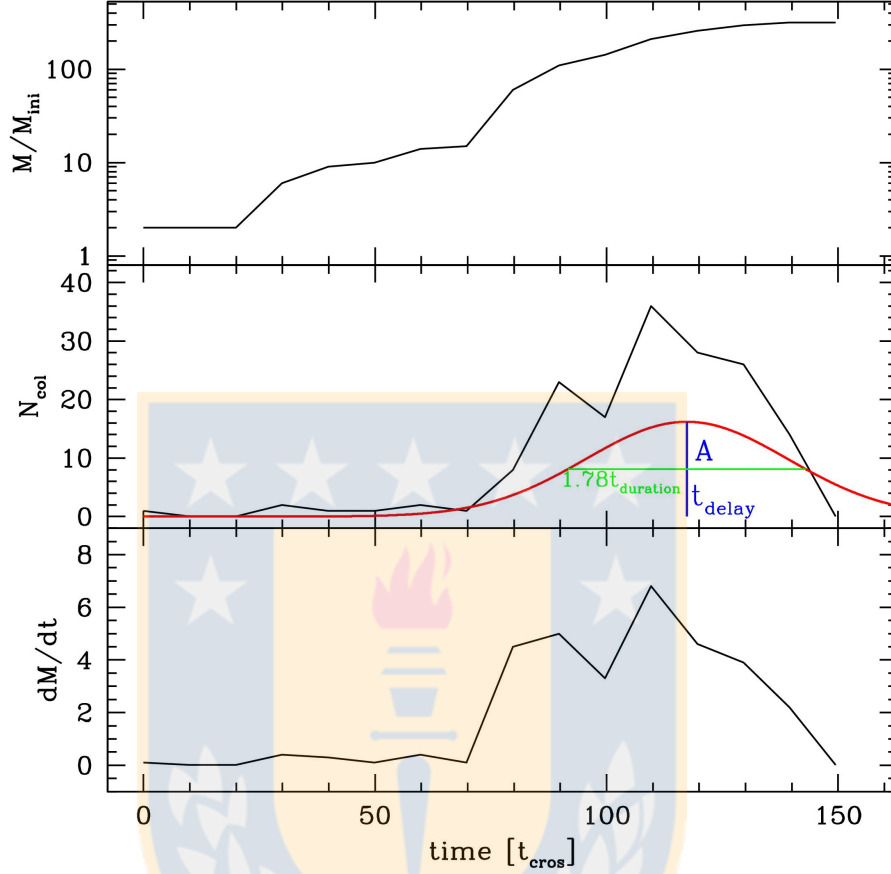


Figure 4.8: Computing the collision rate with a time interval of 10 crossing times. Top panel: Mass growth of the runaway object during the simulation in units of the initial mass M_{ini} . This simulation consists of $N = 5000$ stars, each with a mass of $M_{\text{ini}} = 2 M_{\odot}$ and a radius of $R_{\text{star}} = 200 R_{\odot}$. Middle panel: Number of collisions with the runaway object (in bins of 10 crossing times) as a function of the crossing time of the cluster. The red line shows the best fit for the data binned in $5 t_{\text{cros}}$ for comparison (see Fig. 4.6). Note that the Gaussian fit is still a good description for the time delay and duration of the runaway collision process, the parameter A may be adjusted later for a better agreement with the total number of collisions. Bottom panel: Mass growth in intervals of $10 t_{\text{cros}}$. At this time interval this plot shows the contribution from several collisions and the Gaussian shape is now evident. Source: Own elaboration.

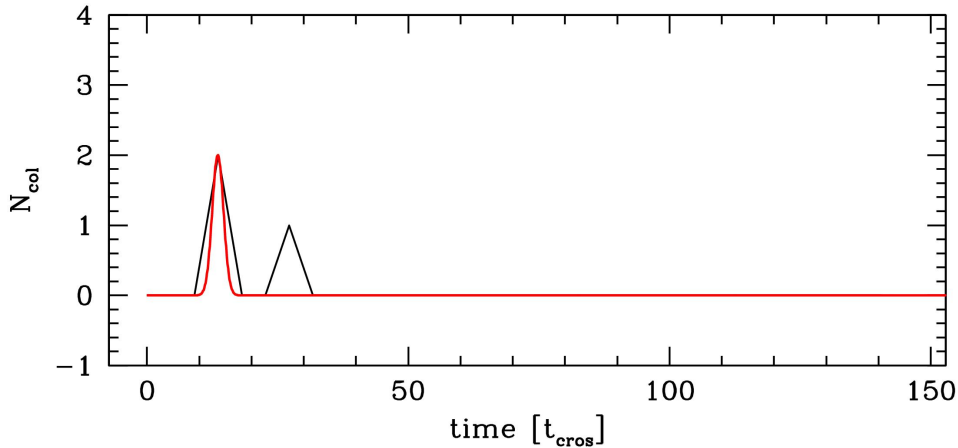


Figure 4.9: Example of a simulation with few collisions. Number of collisions as a function of the crossing time of the cluster calculated in bins of $5 t_{\text{cr}}$ for a simulation with $N=100$ stars with $20 R_{\odot}$ each. Due to the lack of collisions the Gaussian function represented by the red line is not well fitted. The solution is to combine the data from the 10 random simulations as described in Sec. 4.5.5. An example of the improvement of the fit after the combination of the data is shown in Fig. 4.10. Source: Own elaboration.

we used consist in the combination of the data from the 10 random simulations by first binning the data of each simulation using the same time interval ($5 t_{\text{cros}}$ in our case). Once this is done we just sum the number of collisions in each file for each time interval. The Gaussian shape is best reproduced now given that most of the collisions occur at approximately the same time in all the random simulations.

4.6 Parameter estimation

Once we combined and fitted Gaussian functions to the data the next step is to find relations between the Gaussian parameters and our parameter space defined by combinations of N and R_{star} . The parameters t_{delay} and t_{duration} are not seriously affected by the combination of the 10 simulations, in fact there is a very good agreement for the parameters derived using 1 or 10 simulations but an improvement in the error estimation. Therefore we use these values to determine the last parameter A by imposing the condition that the function reproduces the average total number of collisions.

The derivation of these parameters comes from the command “fit” in `gnuplot`. We first write the function that we want to fit:

$$f(x) = A * \exp(-(b - x)^2/2c^2), \quad (4.4)$$

with b being the center of the Gaussian and c the standard deviation. Then we use the software `gnuplot` to do the fit as:

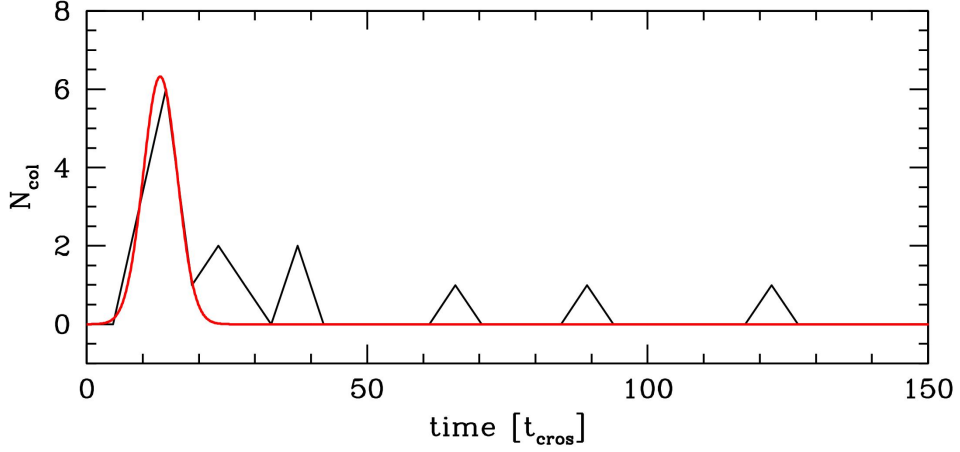


Figure 4.10: Combination of the data. Number of collisions as function of the crossing time of the cluster calculated in bins of $5 t_{\text{cros}}$. This is the combination of 10 random simulations for $N=100$ stars with $R=20 R_{\odot}$. The red line is the best Gaussian fit. Source: Own elaboration.

```
fit f(x) 'params.dat' u 1:2 via A,b,c
```

'params.dat' is a file that contains two columns, the time in units of the crossing time t_{cros} and the number of collisions per time interval in the second column. The results of the fits are presented in Figure 4.11.

After fitting the Gaussian function to the data, we checked if this function can reproduce the expected number of collisions accurately. Therefore we integrated the Gaussian function with the parameters derived for each simulation and compared the prediction with the total number of collisions for every simulation. The result is that we need to correct the values of A by a factor of $1/4$. This factor is probably related to the choice of the time-step for calculating the number of collisions in a given time interval as discussed in Sec. 4.5.3. We have derived the correction factor as follows:

$$A_{\text{corr}} = \frac{\overline{N}_{\text{col,RO}}}{A \int_0^t \exp\left(\frac{-(t-t_{\text{delay}})^2}{2 t_{\text{duration}}^2}\right)}, \quad (4.5)$$

where $\overline{N}_{\text{col,RO}}$ is the mean total number of collisions experienced by the runaway object (calculated from the 10 simulations) and $A \int_0^t \exp\left(\frac{-(t-t_{\text{delay}})^2}{2 t_{\text{duration}}^2}\right)$ is the integration of the Gaussian function which provides the uncorrected expected number of collisions experienced by the runaway object. By applying this correction factor we ensured that the function will reproduce correctly the expected number of collisions. The corrected values for A range from $0.1 - 1$ for $R_{\text{star}} = 20 R_{\odot}$ up to $0.6 - 10$ for $R_{\text{star}} = 5000 R_{\odot}$ (see

Fig. 4.11). We present our derivation for A , t_{duration} , and t_{delay} , and their dependence on N and R_{star} in the following sections.

4.6.1 The normalization factor A

The relation between A and the radii of the stars is clear and can be described as a power law of the form:

$$\log(A) = \alpha \log(R_{\text{star}}) + \beta, \quad (4.6)$$

where α and β are both functions of the number of stars N . The increase of A with R_{star} is expected as the cross-section for collisions increases quadratically with R_{star} . The values of α and β are presented in Tab. 4.2 and a small increase with the number of stars N is found for these parameters. We then apply a simple linear fit to the data presented in Tab. 4.2 and find the expressions for α and β that depend on N as:

$$\alpha = 0.16 \pm 0.09 \log N + 0.06 \pm 0.27, \quad (4.7)$$

$$\beta = -0.05 \pm 0.31 \log N - 1.43 \pm 0.90. \quad (4.8)$$

Then combining Eqs. (4.6), (4.7) and (4.8) we get the expression for A depending on N and R_{star} :

$$\log(A) = [0.16 \log(R_{\text{star}}) - 0.05] \log(N) + 0.06 \log(R_{\text{star}}) - 1.43. \quad (4.9)$$

4.6.2 The delay time and duration time of the runaway growth

As we described in Sec. 4.5.1 we can estimate the expected number of collisions experienced by the runaway object through Eq. (4.3) if we know the delay time for the start of the collision process t_{delay} and the duration of this process t_{duration} . This task is not that easy but we have a good understanding on how the delay time depends on the number of stars and their radii. As shown in the middle panel of Fig. 4.11 the delay time t_{delay} decreases as a power-law with the number of stars, and in fact we used the next equation for fitting this data:

$$\log(t_{\text{delay}}) = \gamma \log(R_{\text{star}}) + \delta. \quad (4.10)$$

The values of γ and δ depends on the number of stars as shown in Tab. 4.2. Our data suggest a clear linear relation between γ and the number of stars N with γ decreasing from -0.15 ± 0.04 at $N = 100$ up to -0.51 ± 0.05 at $N = 5000$. On the other hand, δ increases from 1.39 ± 0.09 at $N = 100$ up to 3.24 ± 0.12 at $N = 5000$. We applied the linear fit to the data shown in Tab. 4.2 and obtained the next expressions:

$$\gamma = -0.21 \pm 0.05 \log N + 0.30 \pm 0.13, \quad (4.11)$$

$$\delta = 1.09 \pm 0.01 \log N - 0.79 \pm 0.04. \quad (4.12)$$

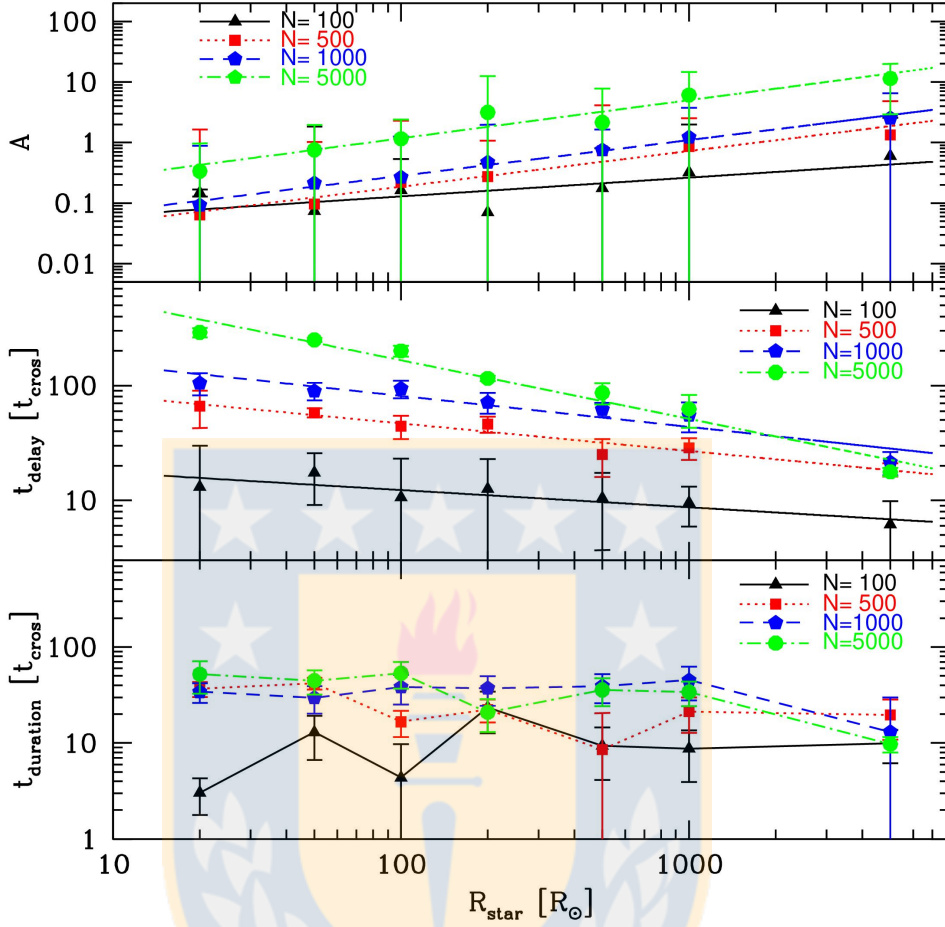


Figure 4.11: Parameters of the Gaussian fit A , t_{delay} , and t_{duration} as functions of the initial stellar radii R_{star} and initial number of stars N . The trends in the first two panels are clear and the behavior is as we expected, the number of collisions increases with increasing the stellar radii or the number of stars since the normalization factor A is an indicator of the total number of collisions. The time at which the runaway growth is triggered, namely t_{delay} decreases with increasing the stellar radii and this is consistent with an acceleration of the contraction phase of the cluster center driven by the rapid formation of massive stars due to their enhanced radii. On the other hand, the core collapse occurs after several relaxation times (see Sec. 1.3) which increases with increasing number of stars and therefore we expect that t_{delay} increases with the number of stars (see Eq. (1.3)). Finally, there is no clear relation between the duration time t_{duration} and the stellar radii. Source: Own elaboration.

N	α	β	γ	δ
100	0.31±0.12	-1.51±0.29	-0.15±0.04	1.39±0.09
500	0.59±0.06	-1.91±0.16	-0.24±0.03	2.15±0.07
1000	0.63±0.07	-1.19±0.19	-0.27±0.05	2.45±0.11
5000	0.59±0.03	-1.73±0.07	-0.51±0.05	3.24±0.12

Table 4.2: Parameters of Equations (4.6) and (4.10). The parameters in the second column were obtained from the fit to the total number of collisions as function of the stellar radii presented in the top panel of Fig. 4.11, using as fitting model the Eq. (4.6). The parameters presented in the third column were obtained from the fit of the data presented in the middle panel of Fig. 4.11, using as fitting model the Eq. (4.10) to estimate the parameter t_{delay} , which is related to the time when the rate of collisions with the central runaway star is maximum; this also depends on the initial radii R_{star} of the stars (Eq. (4.10)). Source: Own elaboration.

The combination of Eqs. (4.10), (4.11) and (4.12) allowed us to relate the delay time t_{delay} with the number of stars and the stellar radii as:

$$\log(t_{\text{delay}}) = [-0.21 \log(R_{\text{star}}) + 1.09] \log(N) + 0.30 \log(R_{\text{star}}) - 0.79. \quad (4.13)$$

While we have related the delay time t_{delay} with the stellar radii, there is no clear relation for the duration time t_{duration} and the stellar radii (see bottom panel of Fig. 4.11). For that reason we explored the dependence of this parameter on the number of stars N . Even when we plot t_{duration} against N , there may be cases in which the duration time decreases as a power-law with increasing N as in the case for $N = 5000$ or cases where the duration time seems to increase and then decrease again as for the case with $N = 100$. Despite this, the general trend, considering the error bars (see Fig. 4.12), is an increase of the duration time with the number of stars and we fitted the data with a power law of the form:

$$\log(t_{\text{duration}}) = 0.34 \pm 0.08 \log N + 0.34 \pm 0.24, \quad (4.14)$$

and we drop, for simplicity, the dependence on R_{star} .

4.6.3 Estimation of the number of collisions

One of the main goals of this research is to determine how many collisions with the runaway object we can expect at a certain time t . We can do this by modeling the runaway collision process as a Gaussian function which depends on 3 parameters: A , t_{delay} , and t_{duration} as we described in Sec. 4.5.1. We have found equations that relate these parameters to the number of stars N of the cluster and the radii of these stars R_{star} . Now a simple integration of the Eq. (4.3) by using the Eqs. (4.9), (4.13) and (4.14) can give us a clue about the expected number of collisions and mass enhancement experienced by the runaway object formed in these clusters. We integrated Eq. (4.3)

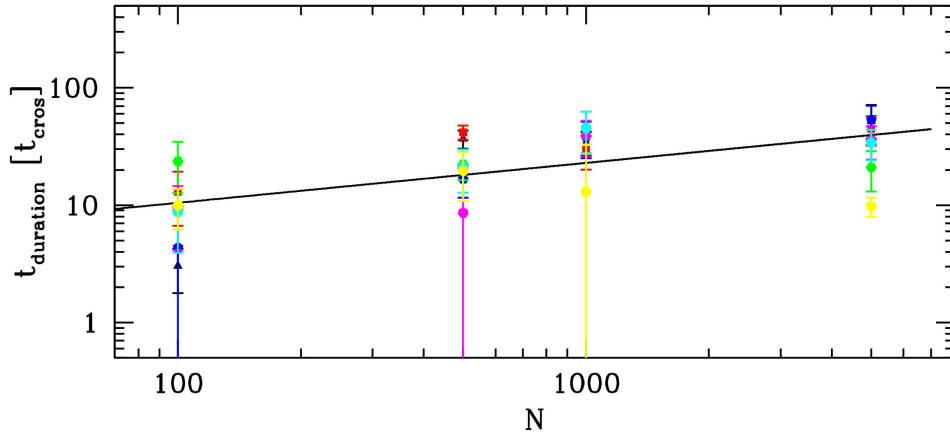


Figure 4.12: Parameter t_{duration} of the Gaussian fit as function of the number of stars N . Considering the error bars, the trend is an increase of t_{duration} with N . We assumed that t_{duration} only depends on N and the fit is described in Eq. (4.14). Source: Own elaboration.

until $t = 1$ Myr and $t = 10$ Myr for N between 50 and 10000 and R_{star} varies from $10 R_{\odot}$ until $2000 R_{\odot}$. While in principle our results are extrapolated for $N > 5000$ we expect that these relations still hold.

Our results show an expected behavior, more collisions occurs in clusters containing more stars with larger radii, in particular, if we consider a time-limit of 1 Myr, we may expect a total of 60 collisions with the runaway object for a cluster containing 10000 stars with $1000 R_{\odot}$ each, and potentially this number can increase up to 150 collisions if these stars have a radii of $2000 R_{\odot}$. Interestingly, a considerable amount of collisions (> 30) is expected only if the radii of the stars is larger or equal to $100 R_{\odot}$ but the number of stars must be between 100 and 1000 approximately, due to the fact that in a cluster containing more stars, the relaxation time, and hence the core-collapse time is longer and thus a time-limit of 1 Myr is not enough for producing an important number of collisions.

On the other hand, if we impose a time-limit of 10 Myr then the expected number of collisions with the runaway object increases by a factor of ~ 3 and now even for relatively small stars ($R_{\text{star}} = 100 R_{\odot}$) we can expect up to 150 collisions in a cluster containing 10000 stars, and in the more extreme case for $N = 10000$ and $R_{\text{star}} = 2000 R_{\odot}$ the number of collisions with the runaway star can be as large as 500. These results are presented in Figure 4.13.

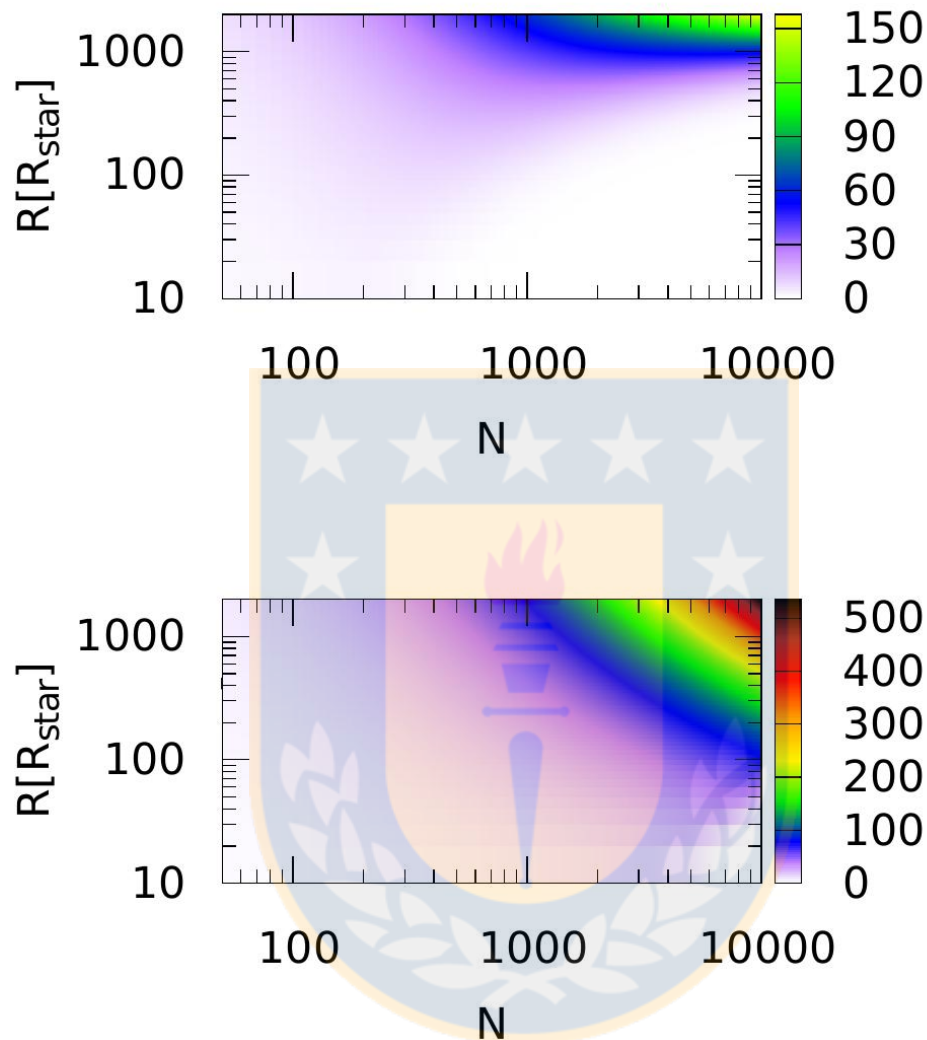


Figure 4.13: Estimation of the number of collisions experienced by the runaway star for different combinations of N and R_{star} . Total number of collisions calculated via Eq. (4.3), represented by the colours in the right colour bar, with the central object after 1 Myr (top panel) and after 10 Myr (bottom panel) for our cluster model depending on the number of stars R_{star} and their initial radii R_{star} . Source: Own elaboration.

Analytic gas potential

The final goal of this project is to produce realistic models of black hole formation in the first stellar clusters of the Universe, including as many effects as current computational capabilities allows. However when one includes that many physics into one simulation it is hard to disentangle the role of the different processes involved in the simulation. For this reason we want to go step by step, adding one effect after the other in such a way that at the end we can completely understand our results. We have initially investigated gas free clusters, which is not very realistic for the early evolution of these systems, as indeed star clusters are born out of a Giant Molecular Cloud (GMC), therefore in their initial stages of life they are still embedded in gas. As found in the Milky Way, embedded clusters can be an order of magnitude more abundant than open clusters [55], at least in a radius of ~ 2 kpc around the Sun, and recent studies using data from the Gaia Data Release 2 (GDR2) have shown that embedded clusters are less likely to be expanding than gas free clusters [56]. In this chapter we go one step forward in the modeling of the first star clusters of the Universe and include the effects of an analytic potential in the results that we found previously in Chapter 4.

5.1 Analytic potential in NBODY6

NBODY6 includes routines to include an external force in the calculations by changing the option `KZ(14)` and this external force may correspond to a standard tidal field, a point-mass galaxy, point-mass + bulge + disk + halo + plummer potential or a plummer potential. Since we are not interested in a cluster close to a spiral galaxy, the most adequate option for us is to include an external Plummer potential centered in our Plummer distribution of stars, this is, `KZ(14) = 4`. When this option is activated, the routine `xtrnl0.f` is called to initialize the Plummer potential. The important parameters are: `MP` which is the total mass of the Plummer sphere in N -body units, `AP2` which is the Plummer scale-radius in N -body units, `MPDOT` which is the time scale (in N -body units) over which the gas is expelled from the cluster, i.e., after this time, the mass of the Plummer potential has been reduced to $M_{\text{plummer}} = MP \times e^{-1}$, and finally, `TDELAY`

which is the time, in N -body units, after which the gas expulsion starts. Now we present a fragment of the routine *xtrnl0.f* in which the plummer potential is initialized and the velocities of the stars are scaled to the virial ratio Q defined by the user in the input file.

```

*      Include Plummer potential for 2D and 3D (use MP = 0 if not needed).
      IF (KZ(14).EQ.3.OR.KZ(14).EQ.4) THEN
*      Check input for Plummer potential.
          READ (5,*) MP, AP2, MPDOT, TDELAY
          WRITE (6,70) MP, AP2, MPDOT, TDELAY
70      FORMAT (/ ,12X, 'PLUMMER POTENTIAL: MP =',F7.3, ' AP =',F6.2,
&          ' MPDOT =',F8.3, ' TDELAY =',F5.1)
          MPO = MP
          AP2 = AP2**2
          IF (KZ(14).EQ.3) RTIDE = RTIDE*(ZMASS + MPO)**0.3333
*      Rescale velocities by including the Plummer & galactic virial
energy.
          IF (ZKIN.GT.0.0D0) THEN
*      Note that QVIR = Q is saved in routine SCALE and VIR < 0 with
GPU.
          CALL ENERGY
          VIR = POT - VIR
          QV = SQRT(QVIR*VIR/ZKIN)
          DO 80 I = 1,N
              DO 78 K = 1,3
                  XDOT(K,I) = XDOT(K,I)*QV
78          CONTINUE
80          CONTINUE
          END IF

```

Note that the routine *ENERGY* is called to calculate the potential energy *POT* of the stars associated to the Plummer potential, then the scale factor for velocities *QV* is calculated taking into account this extra force and finally the velocities of the stars are adjusted with this factor. Here we present the input file that we used to perform the simulations using an analytic Plummer potential:

```

1 10000.0
5000 1 10 826 145 1
0.02 0.01 0.2 1.0 1.0 1419.0 2.0E-01 0.14 2.0
1 1 1 0 1 0 2 0 0 0
0 0 0 4 1 1 0 0 0 0
1 1 2 0 0 2 2 0 0 0
1 0 0 0 0 0 2 1 0 1
0 0 0 1 0 0 0 0 0 0
1.0E-03 0.001 0.2 1.0 1.0E-06 0.001
1.0 2.0 2.0 0 0 0.0001 0.0 0.0
0.5 0.0 0.0 0.0 0.125
1.0 0.59 10000 10000
1.0 5000 0 500.0 1.0

```

5.1.1 Stability of the clusters under the effects of an external potential

We present in Fig. 5.1 an example of a simulation of a cluster containing 5000 stars with the same setup shown in Sec. 5.1 but without using the option for the external potential ($KZ(14)=0$). The cluster remains in virial equilibrium after 50 crossing times and no stars escape the cluster. A binary is formed between 32 and 38 crossing times but it is disrupted some time in between 42 and 48 crossing times.

We then performed the same simulation but including now the option for an external Plummer potential ($KZ(14)=4$). The situation is shown in Fig. 5.2 and is practically the same, with no escaping stars during the first 50 crossing times, and the Lagrangian radii remain constant enough to ensure that the cluster is in virial equilibrium. Compared to the cluster without the external potential in which at 50 t_{cross} the 90% Lagrangian radius was 0.8 pc, in this case the 90% Lagrangian radius is 0.7 pc. A small difference is also seen in the number of binaries, now one binary is formed between 44 and 50 t_{cross} . The goal of this analysis was to make sure that we model a stable star cluster after the addition of an external Plummer potential.

5.2 First simulations

After we ensure that we can properly model a star cluster with an external potential to mimic, at first order, the effects of including gas in our simulations we can start to explore the effects of this extra force on our previous results. We performed a set of

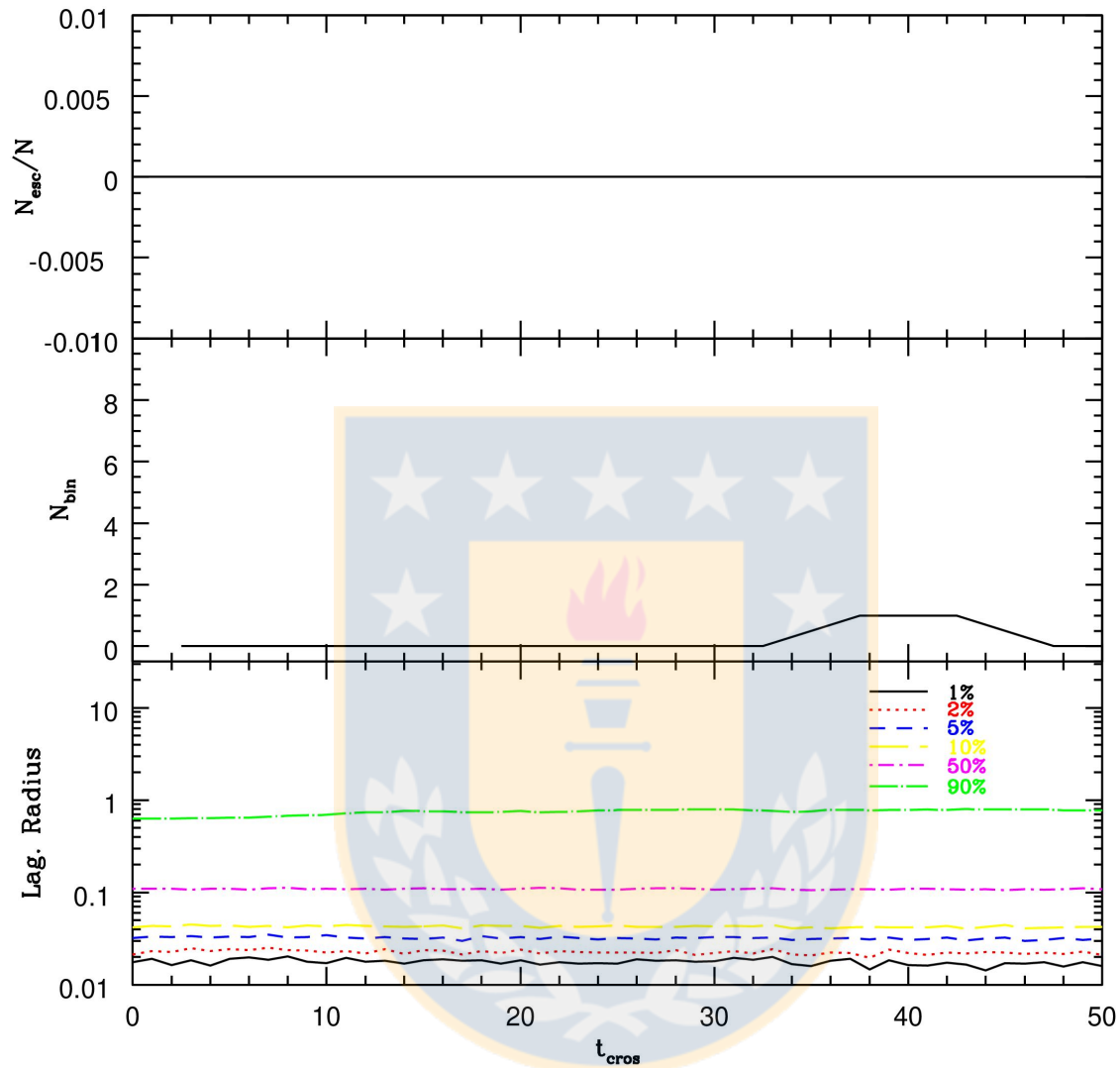


Figure 5.1: Stability of a star cluster without an analytic potential. Stability of a star cluster of 5000 stars evolved until 50 crossing times. The top panel shows the fraction of escaped stars which in this case is 0. The middle panel shows the number of binaries formed in the cluster, in bins of 5 crossing times. The bottom panel shows the 1%, 2%, 5%, 10%, 50% and 90 % Lagrangian radii and clearly these radii remains stable during this early evolution of the cluster. Source: Own elaboration.

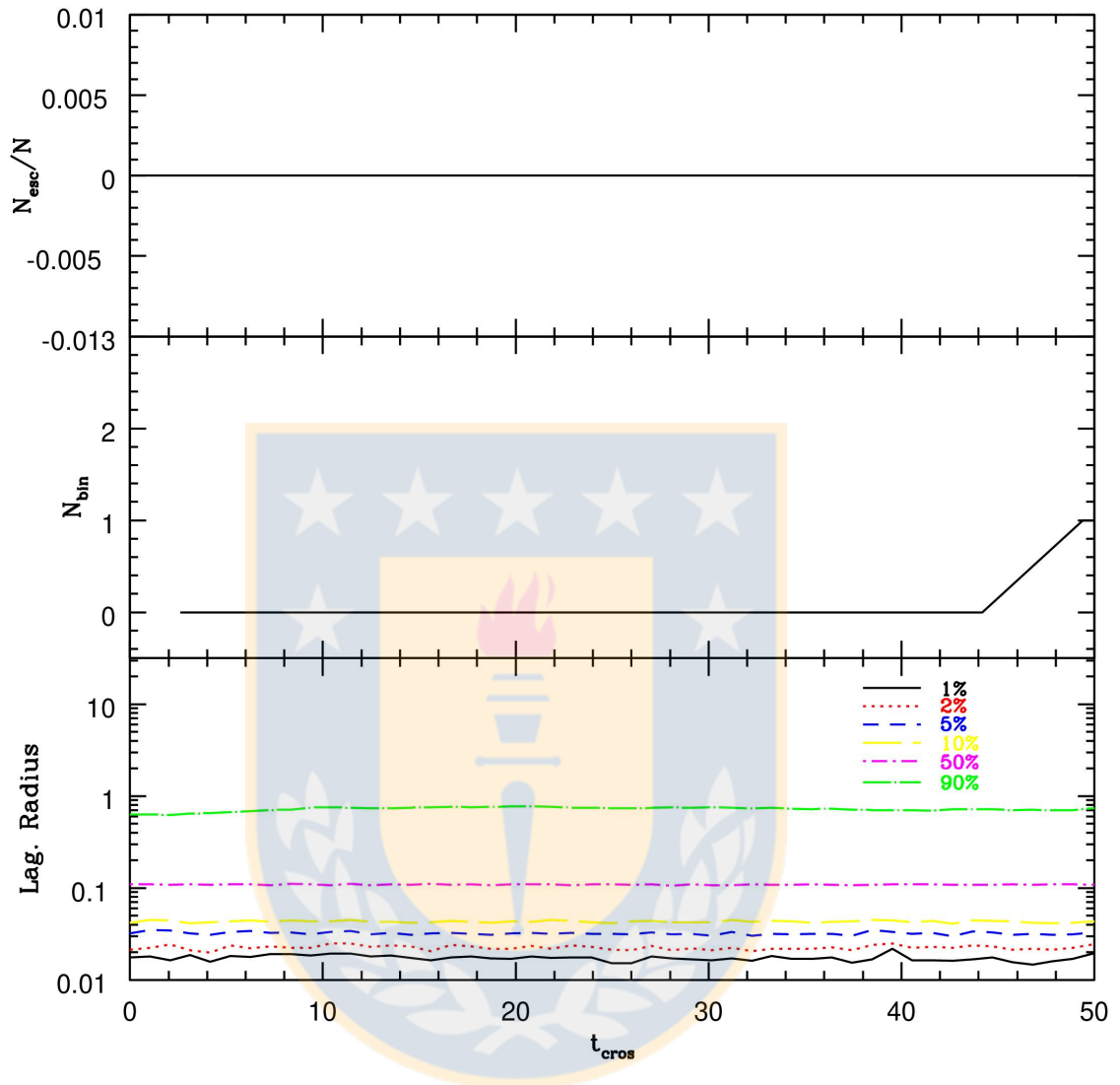


Figure 5.2: Stability of a star cluster with an analytic potential. Stability of a star cluster of 5000 stars evolved until 50 crossing times and under the influence of an external potential. The top panel shows the fraction of escaped stars which in this case is 0. The middle panel shows the number of binaries formed in the cluster, in bins of 5 crossing times. The bottom panel shows the 1%, 2%, 5%, 10%, 50% and 90 % Lagrangian radii and clearly these radii remains stable during this early evolution of the cluster. Source: Own elaboration.

12×2 simulations, the first 12 are a combination of $N = 100, 500, 1000$ & 5000 stars, with $R_{\text{star}} = 50, 100, 500 R_{\odot}$. The remaining 12 simulations are the same initial conditions but with the addition of the external Plummer potential with a total mass of $10^4 M_{\odot}$ and a half-mass radius of 0.1 pc. The summary of the initial conditions for this set of simulations is presented in Tab. 5.1. We ran these simulations until $1000 t_{\text{cross}}$, a moment at which the runaway collision process has stopped in the gas-free clusters, this corresponds to a time of 7.8 Myr for these clusters, whereas for the clusters containing an analytic potential, $1000 t_{\text{cross}}$ corresponds to 5.5 Myr. From the analysis of the first set of 12 simulations we find that the runaway collision process has stopped in the gas-free clusters, and the fraction of colliding stars depends on the stellar radius rather than on the number of stars (see Fig. 5.3), as we already found in Ch. 4. We also show the final mass of the runaway object in units of its initial mass and we also confirm our previous results, that the mass enhancement depends on both N and R_{star} (see Fig. 5.4).

For the first set of simulations we employed a modification for the collision criteria. As discussed in Sec. 2.4.1, the previous criteria for detecting collisions was based on the paper by Kochanek 1992[51]

$$R_{\text{coll}} = 1.7 \left(\frac{m_1 + m_2}{2m_1} \right)^{1/3} R_1.$$

We modified this line in the code, in the routine *ksint.f* from the line 465

```

      IF (KZ(43).GE.2.AND.KSTAR(J2).EQ.14) THEN
        RCOLL=RADIUS(J1)+RADIUS(J2)
      ELSE IF (KZ(27).LE.2) THEN
*      Adopt collision criterion of Kochanek (Ap.J. 385, 604, 1992).
        FAC = 0.5*BODY(I)/BODY(J1)
*      RCOLL = 1.7*FAC**0.3333*RADIUS(J1)
        RCOLL = RADIUS(J1) + RADIUS(J2)
      ELSE
        RCOLL = 6.0*BODY(I)/CLIGHT**2
      END IF

```

we have just commented the line with the previous collision criteria and wrote the new one as $\text{RCOLL} = \text{RADIUS}(J1) + \text{RADIUS}(J2)$, therefore now the collision occurs once the distance d between two stars become smaller than the sum of their radii $R_1 + R_2$.

We also had to employ this modification on the same routine *ksint.f*. From line 581 we have

```

*      Set possible BH index and check disruption condition (& #43) first.
      J2 = 2*IPAIR + 1 - J1
      IF (KZ(43).GE.2.AND.KSTAR(J2).EQ.14) THEN
        RCOLL = (BODY(J2)/BODY(J1))**0.3333*RADIUS(J1)
      ELSE IF (KZ(27).LE.2) THEN

```

N	R_{star} R_{\odot}	M_{stars} M_{\odot}	$R_{\text{h,stars}}$ pc	M_{gas} M_{\odot}	$R_{\text{h,gas}}$ pc	t_{cros} Myr
100	50	10^4	0.1	-	-	0.0078
100	100	10^4	0.1	-	-	0.0078
100	500	10^4	0.1	-	-	0.0078
500	50	10^4	0.1	-	-	0.0078
500	100	10^4	0.1	-	-	0.0078
500	500	10^4	0.1	-	-	0.0078
1000	50	10^4	0.1	-	-	0.0078
1000	100	10^4	0.1	-	-	0.0078
1000	500	10^4	0.1	-	-	0.0078
5000	50	10^4	0.1	-	-	0.0078
5000	100	10^4	0.1	-	-	0.0078
5000	500	10^4	0.1	-	-	0.0078
100	50	10^4	0.1	10^4	0.1	0.0055
100	100	10^4	0.1	10^4	0.1	0.0055
100	500	10^4	0.1	10^4	0.1	0.0055
500	50	10^4	0.1	10^4	0.1	0.0055
500	100	10^4	0.1	10^4	0.1	0.0055
500	500	10^4	0.1	10^4	0.1	0.0055
1000	50	10^4	0.1	10^4	0.1	0.0055
1000	100	10^4	0.1	10^4	0.1	0.0055
1000	500	10^4	0.1	10^4	0.1	0.0055
5000	50	10^4	0.1	10^4	0.1	0.0055
5000	100	10^4	0.1	10^4	0.1	0.0055
5000	500	10^4	0.1	10^4	0.1	0.0055

Table 5.1: Initial conditions for simulations with an external potential. The simulations consist of gas-free clusters and clusters with an external analytic potential. The first column shows the number of stars, the second column is the radius of the stars, the third column is the total mass in stars, the fourth column is the half-mass radius for the stellar distribution. Columns 6 and 7 are the total mass and half-mass radius for the external Plummer potential. The last column is the crossing time of the cluster. Source: Own elaboration.

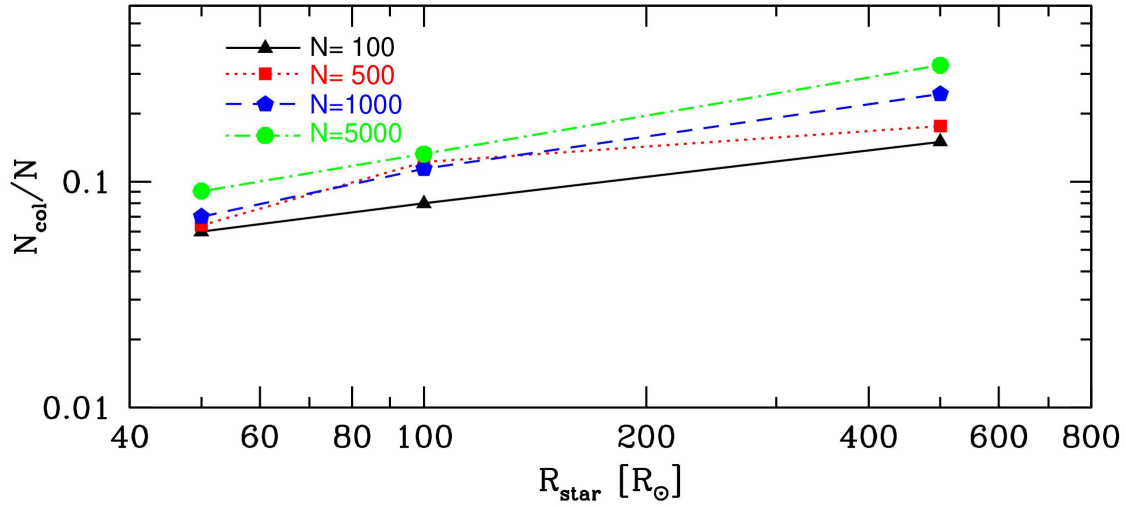


Figure 5.3: Collision fraction for a gas-free star cluster. Fraction of collisions for star clusters without gas for different combinations of N and R_{star} . As discussed in Ch. 4, the inner parts of the cluster contract due to two-body relaxation effects and the runaway collision process takes place. The expected fraction of collisions does not depend (or depends very weakly) on the number of stars, but rather it depends on the stellar radius. Source: Own elaboration.

```

*      Adopt collision criterion of Kochanek (Ap.J. 385, 604, 1992).
      FAC = 0.5*BODY(I)/BODY(J1)
*      RCOLL = 1.7*FAC**0.3333*RADIUS(J1)
      RCOLL = RADIUS(J1) + RADIUS(J2)
      ELSE
      RCOLL = 6.0*BODY(I)/CLIGHT**2
      END IF

```

It is also important to note that in our input file now we have used the option `KZ(27) = 2` which reproduced best the results for the number of collisions compared to the simulations using the code `ph4` in `AMUSE` (See sec. 6.3.1 and Fig. 6.1).

From the analysis of the first set of 12 simulations we find that the runaway collision process has stopped in the gas-free clusters, and the fraction of colliding stars depends on the stellar radius rather than on the number of stars (see Fig. 5.3), as we already found in Ch. 4. We also show the final mass of the runaway object in units of its initial mass and we also confirm our previous results, that the mass enhancement depends on both N and R_{star} (see Fig. 5.4), but now due to the modification of the collision criteria, the number of collisions as well as the mass enhancement of the runaway object has increased by a factor of about 2. The same collision criteria is used for the remaining 12 simulations that include an external potential.

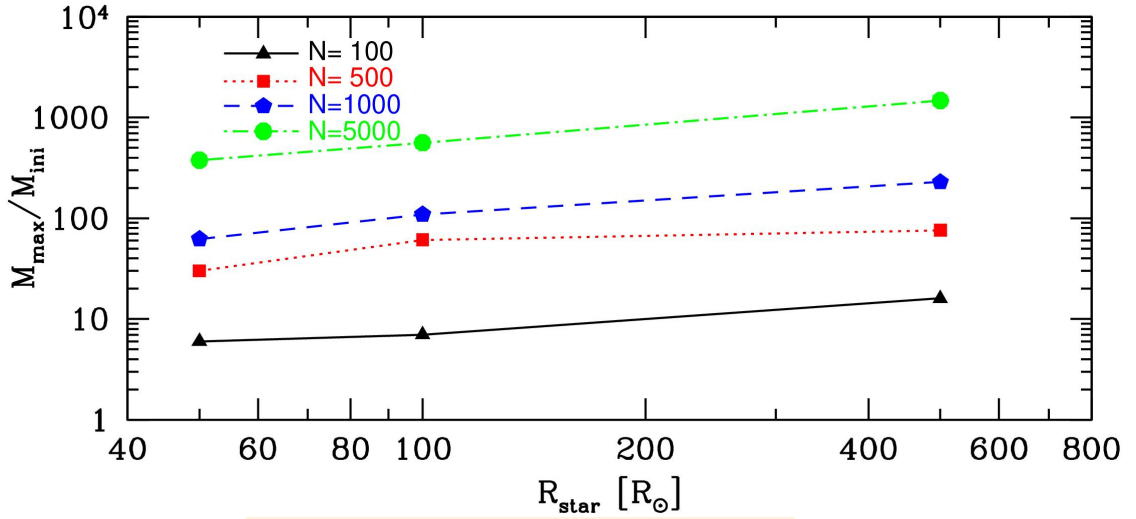


Figure 5.4: Mass of the runaway object for a gas-free star cluster. Final mass of the runaway object divided by its initial mass, for star clusters without gas for different combinations of N and R_{star} . We can expect a higher mass enhancement for clusters containing more stars, and with larger stars. Source: Own elaboration.

After the analysis of the remaining set of 12 simulations including the external force of an analytic Plummer potential centered in the center of the cluster, our results show that collisions are not greatly enhanced under the influence of this external force, in fact, the smallest clusters ($N = 100$) were evaporated even before reaching $1000 t_{\text{cross}}$, but also more collisions occurred and there was an enhancement in the mass of the most massive object. The fraction of collisions and the mass of the runaway object also increased for clusters with $N = 500$ stars, however, for clusters with $N = 1000$ and $N = 5000$ there was a decrease in both the fraction of collisions and the mass of the runaway star (see Figs. 5.5 and 5.6) compared to gas-free clusters. This is at first a bit misleading given that we expect a deeper contraction during the core-collapse phase and that the cluster remains contracted for a longer time due to the additional gravitational force acting on the stars. The fact that we have less collisions in the same number of crossing times is related to this additional force and we will explore the reasons in the next section.

5.3 A delay in the runaway growth

In the previous section we found an unexpected result, the number of collisions in a cluster with an external potential was decreased compared to a gas-free cluster and therefore also the mass enhancement for a time-limit of $1000 t_{\text{cross}}$. We now present the same set of simulations but using a longer simulation time because we suspect that the runaway growth was not yet started in the clusters with $N = 1000$ and $N = 5000$ stars. We

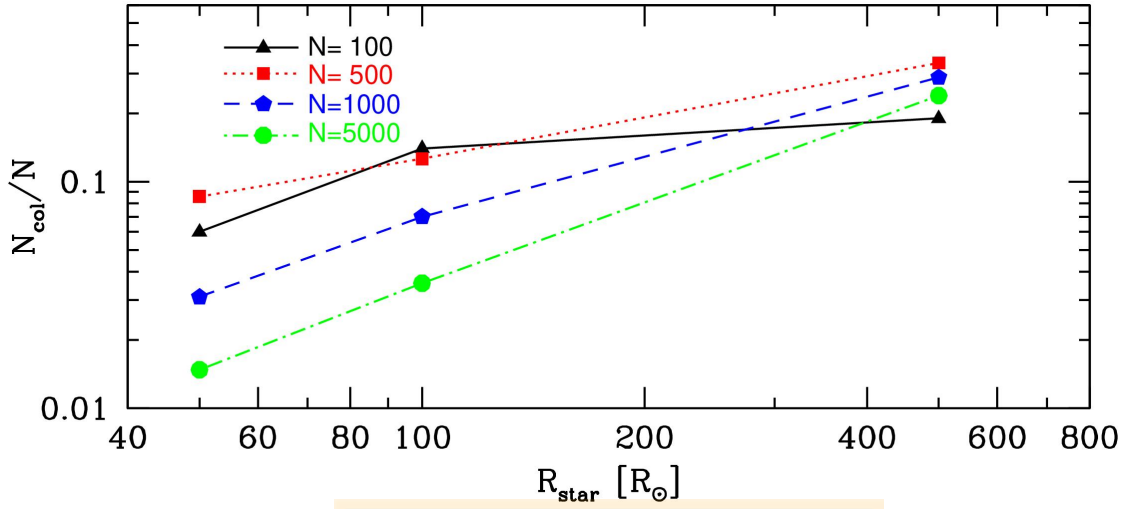


Figure 5.5: Fraction of collisions for different clusters under the influence of an external Plummer potential. The simulations were run until $1000 t_{\text{cross}}$, the same as the gas-free clusters but, despite the cases of $N = 100$ and $N = 500$, the number of collisions has decreased due to the external force. Source: Own elaboration.

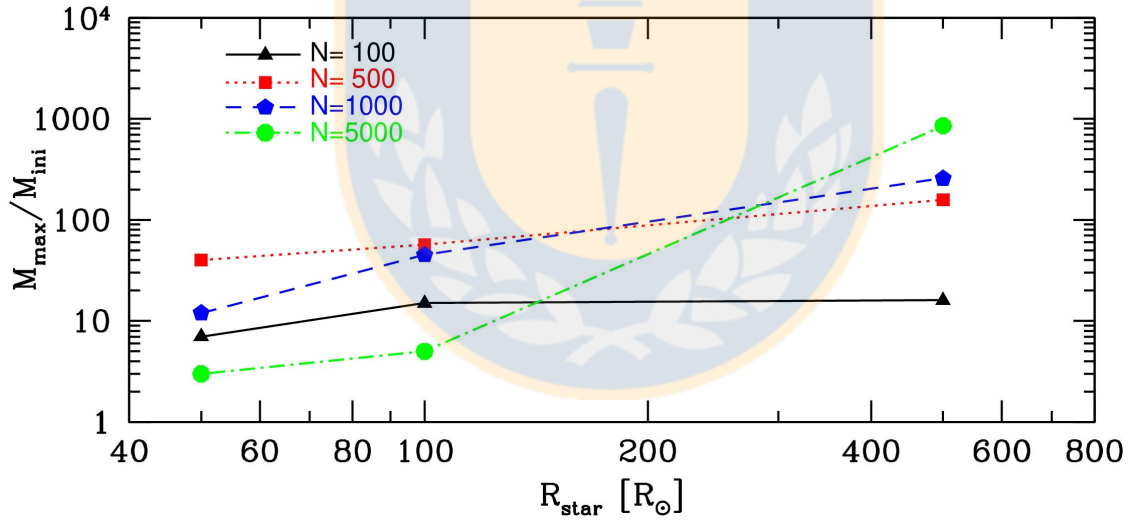


Figure 5.6: Mass enhancement of the runaway object for different clusters under the influence of an external Plummer potential. The simulations were run until $1000 t_{\text{cross}}$, the same as the gas-free clusters but, despite the cases of $N = 100$ and $N = 500$, the number of collisions has decreased and therefore so did the mass enhancement. Source: Own elaboration.

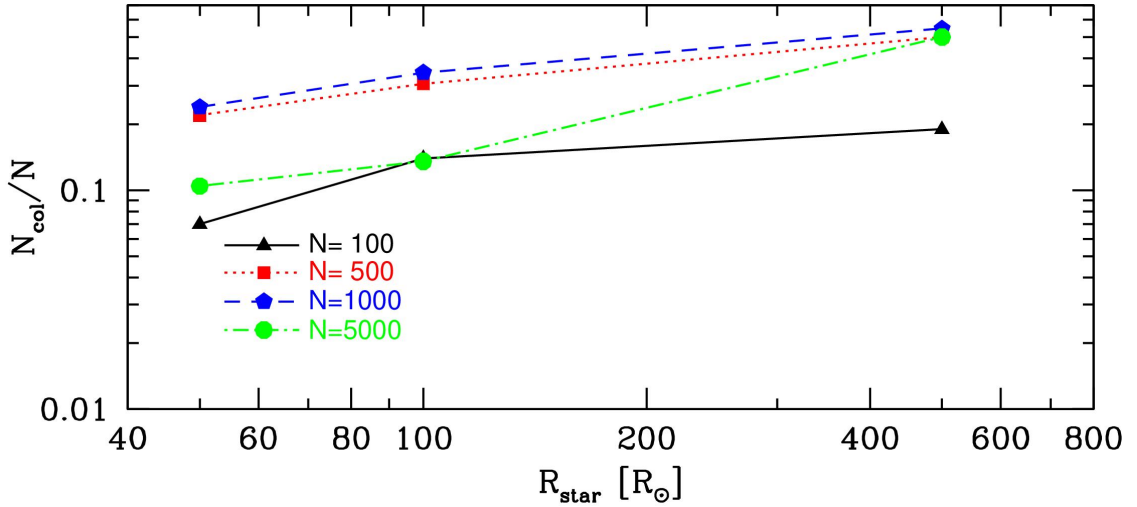


Figure 5.7: Collision fraction at the end of the runaway growth for clusters with an external potential. Fraction of collisions (y -axis) for clusters under the influence of an external Plummer potential as a function of the stellar radius (x -axis) for clusters containing different numbers of stars. Compared to the case when the runaway growth was not finished (Fig. 5.5) we see now an enhancement in the collision fraction except for $N = 100$ because these clusters were evaporated and for $N = 5000$ because at some point in the simulation, the runaway object was ejected from the cluster. Source: Own elaboration.

therefore ran these simulations until $3000 t_{\text{cross}}$ for clusters with $N = 1000$ stars and $4000 t_{\text{cross}}$ for clusters with $N = 5000$ stars. The results show that effectively the runaway growth had not started yet in larger clusters and that this process was delayed in all the clusters. Interestingly, this runaway process is now different for the cluster containing $N = 5000$ stars, in fact now the total fraction of collisions is enhanced only for the case when $R_{\text{star}} = 500 R_{\odot}$ and it remained the same for stars with 50 and $100 R_{\odot}$ (see Fig. 5.7). The reason is that for these simulations, the runaway star escaped from the cluster and this halted the collision process during a short period of time and then a new runaway star started to emerge, but there was little time to compensate for the number of collisions. We still have not investigated in detail why the most massive star escaped from the clusters, and we think for now that these may be rare events, but in the future we are going to look further into this.

For the mass enhancement we find for $N = 500$ and $N = 5000$ that the runaway object is more massive by a factor of 3 if there is an external potential in the cluster, however for $N = 100$ the external potential caused the clusters to evaporate and for the clusters with $N = 5000$ stars, the runaway star was ejected from the cluster at some point, and then a new runaway star emerged but there was not enough time to grow

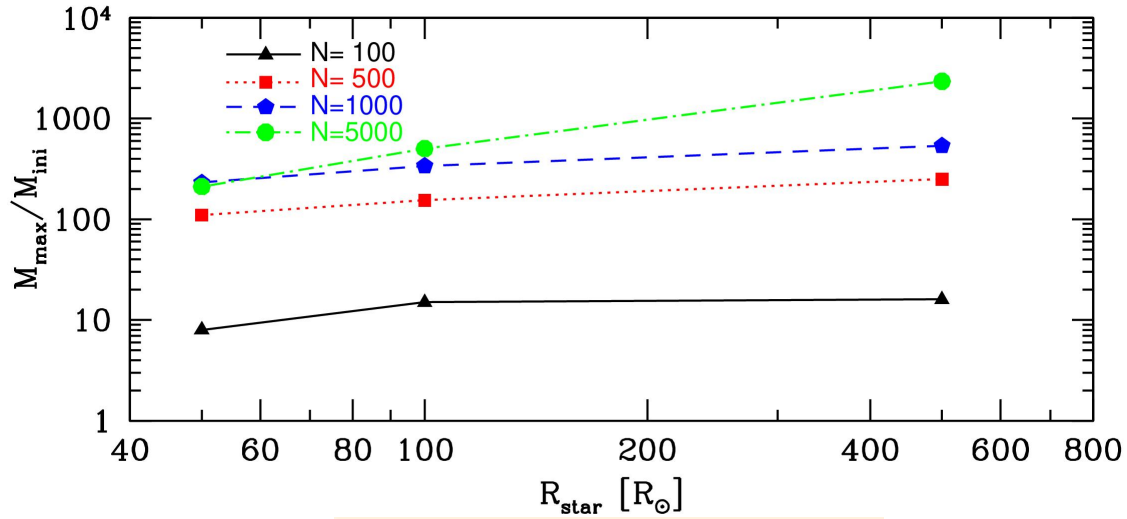


Figure 5.8: Mass enhancement of the runaway star at the end of the runaway growth for clusters with an external potential. Mass enhancement in units of the initial mass (y -axis) of the runaway star in clusters under the influence of an external Plummer potential as a function of the stellar radius (x -axis) for clusters containing different number of stars. Compared to the case when the runaway growth was not finished (Fig. 5.6) we see now an enhancement in the mass, except for $N = 100$ because these clusters were evaporated. For $N = 5000$ we see little enhancement because at some point in the simulation, the runaway object was ejected from the cluster and then a new runaway star emerged and the time was not enough for the runaway growth to finish properly. Source: Own elaboration.

further in mass, so the mass enhancement remained the same as in the gas-free clusters. This results are shown in Fig. 5.8.

5.3.1 The importance of binaries

We were quite surprised by the fact that the runaway growth is delayed due to the presence of an external potential that we included to mimic the effects of the gas in the clusters. We expected an increased number of collisions due to the extra force acting on the stars, and actually there was an increase but the process was slower. We show an example of the delay in the runaway growth in Fig. 5.9 and we found that in clusters with an external potential the binary collisions are occurring at much later times. In all the clusters with and without an external potential there is a constant rate for hyperbolic collisions (collisions in which the binding energy of the stars before the collision was larger than zero) and this rate is maintained during the entire simulation, then, at some point we see binary collisions occurring (collisions in which the binding energy of

the stars before colliding was less than zero) and they can be as important as 40% of the total number of collisions in the cluster. The onset of the binary collisions is delayed for clusters under the influence of an external potential as can be seen in the third panel of Fig. 5.9 but still the fraction of binary collisions is as important as 30% of the total number of collisions in these clusters. In both cases the runaway growth occurs shortly after the onset of the binary collisions suggesting that the hyperbolic collisions, at least before this, only produce several stars quite more massive than the rest.

The natural question now is why there is a delay in the onset of the binary collisions in clusters under the influence of the external potential, and to address this issue we have explored the total number of binaries in clusters with and without the external potential. For this we make use of the option `KZ(9) = 2` in the input file of NBODY6. With this option we obtain two files showing the properties of soft and hard binaries, the soft binaries being binaries with a semi-major axis larger or equal to 0.1 times the virial radius of the cluster, therefore soft binaries in our simulations are those with a semi-major axis larger or equal to 0.014 pc and hard binaries are binaries with a separation smaller than this. With this information printed in the files `OUT9` and `fort.19` we can now count the total number of binaries in bins of $5 t_{\text{cross}}$ and understand how the population of binaries change over time in both clusters. We present the results of this analysis in Fig. 5.10, where we see in the top panel, the total number of binaries as a function of the crossing time of the cluster for a gas-free cluster, and in the bottom panel the same information for a star cluster subject to the effects of the external potential. We have found that the number of binaries is always larger in gas-free clusters, there are always more than 10 binaries during the first $400 t_{\text{cross}}$, and binaries are formed and destroyed during all the simulation. After the first $400 t_{\text{cross}}$ there is a decrease in the number of binaries due to the onset of the binary collisions. For the clusters under the effect of the external potential, this picture is different, in general we always see less binaries in these clusters, and at some times there are no binaries in the system. We also find a small increase in the number of binaries just before the onset of the binary collisions and naturally the number decreases after this onset. In the clusters that are subject to the additional force the stars have to move faster to compensate the extra gravity in order to have a virialized system. As the stars move faster in that situation, it is harder to form binaries because the velocity has to be slowed down more than in the clusters without the additional potential, and, moreover, the kinetic energy may become comparable now to the binding energy of the binaries, thus is easier to destroy these systems until eventually some energy has been dispersed from the system and there is a rise in the number of binaries and subsequently the onset of the binary collisions. So we have found the reason for the delay in the runaway growth due to the addition of an external potential, but we have opened a few new questions like why there is an onset of binary collisions shortly after an enhancement in the number of binaries, or if the destruction of binaries is related to the evaporation of the clusters containing $N = 100$ stars. These questions we will not answer now but they will be addressed in a future investigation.

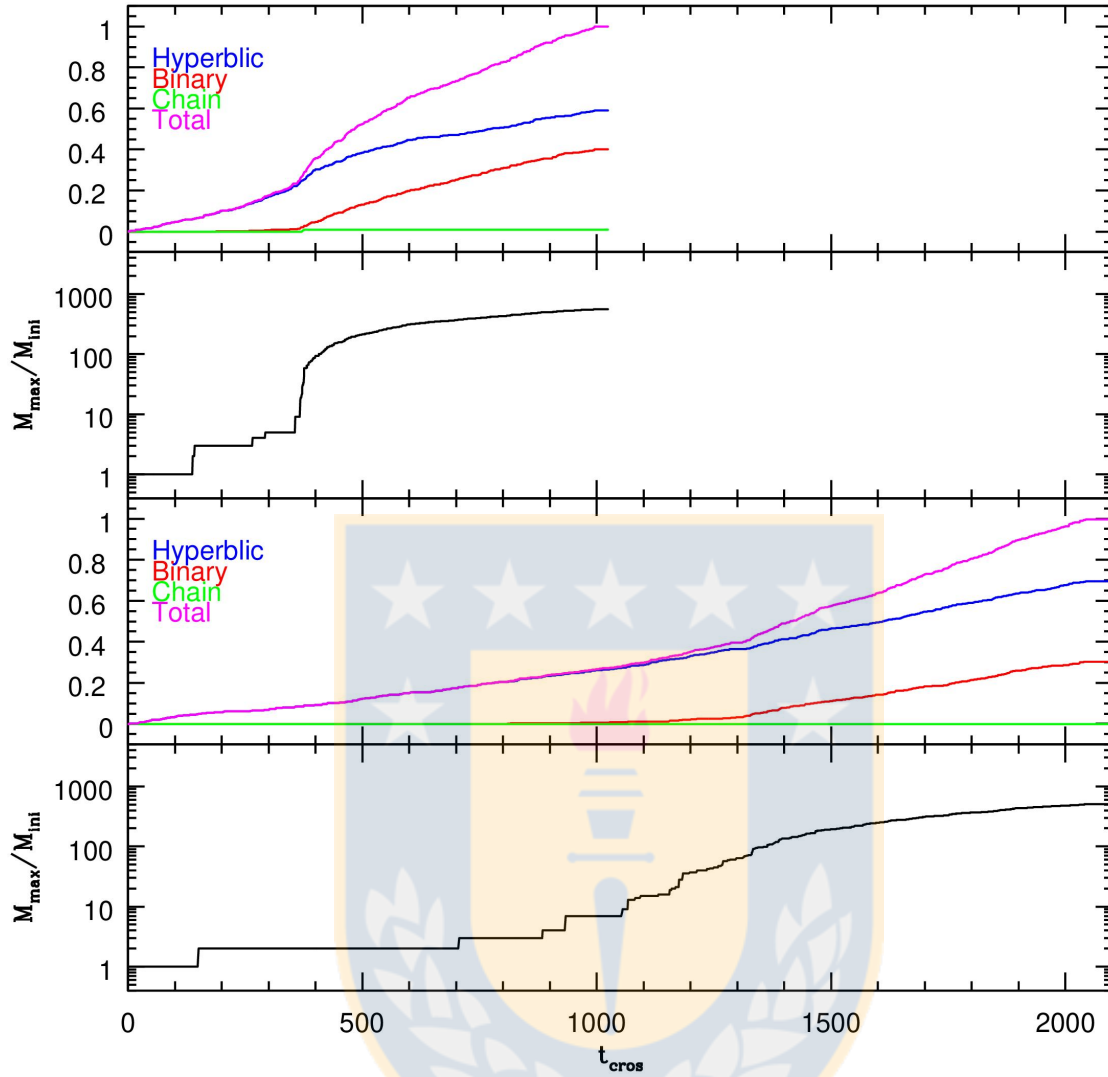


Figure 5.9: Delay in the runaway growth due to an external potential. Delay of the runaway growth for clusters under the influence of an external potential. The top panel shows the fraction of hyperbolic collisions (blue solid line), i.e. the result of a close encounter where the binding energy was larger than zero. The red solid line shows the fraction of binary collisions, i.e. the result of a close encounter where the binding energy was less than zero. The solid green line shows the fraction of chain collisions, i.e. a system of 3 or more bound stars. The top panel is the result of a simulation for a gas-free cluster and we see that hyperbolic collisions occur during all the simulation and at some point binary collisions become important at around $400 t_{\text{cross}}$ eventually becoming 40% of the total fraction of collisions. The second panel shows the mass growth of the runaway object whose mass has reached $100 M_{\text{ini}}$ in only $400 t_{\text{cross}}$. The third panel is the same as the first panel but for a cluster under the influence of an external Plummer potential. In this case we see that during all the simulation there is a constant rate of hyperbolic collisions and that binary collisions starts at around $1100 t_{\text{cross}}$ eventually reaching 30% of the total number of collisions. The fourth panel is the same as the second panel showing the mass growth of the most massive object in the cluster with an external potential and the delay in the runaway growth is clear, now the mass has grown by a factor of 100 at $1300 t_{\text{cross}}$. Source: Own elaboration.

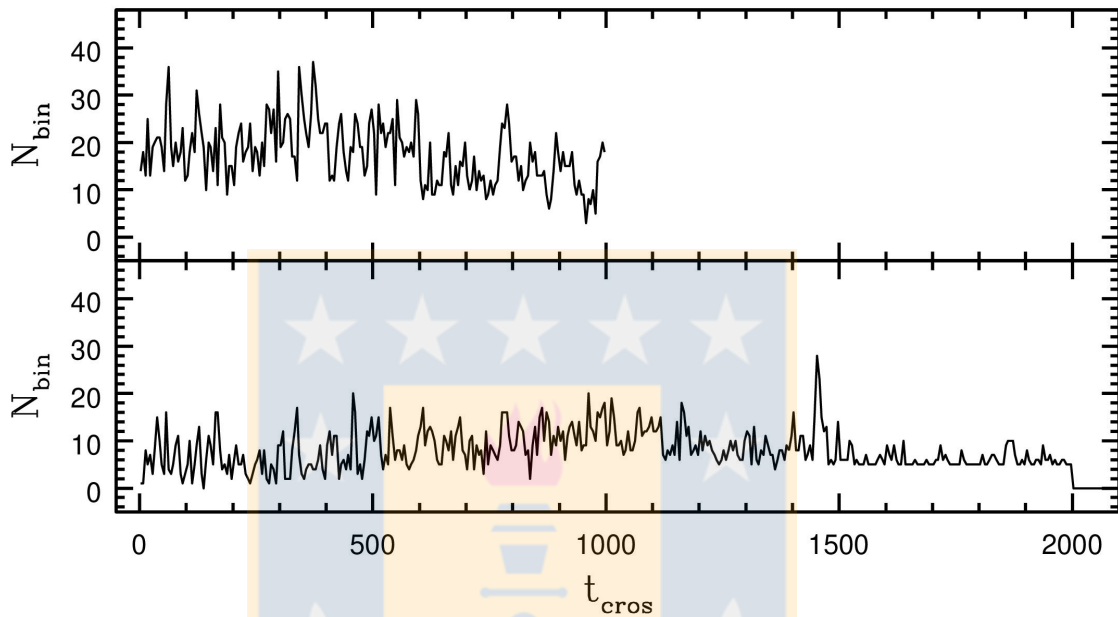


Figure 5.10: The effects of an external potential on the number of binaries in a cluster. Number of binaries as a function of the crossing time of the cluster for a gas-free star cluster in the top panel and for a cluster under the influence of an external potential in the bottom panel. In general, there are always more binaries in the gas-free clusters and a small increase just before the onset of the binary collisions which starts at $400 t_{\text{cros}}$ (see Fig. 5.9) and then a decrease due to the collisions between the stars in binary systems. In the cluster subject to the additional force of the analytic potential, the number of binaries is about half of the binaries in the cluster without the external potential, and we also see a small increase in the number of binaries prior to the onset of the binary collisions which starts at around $1100 t_{\text{cros}}$. Source: Own elaboration.



Chapter 6

AMUSE

In chapter 2.1 we described the main features of NBODY6, in particular, the integration method which is a fourth order predictor corrector scheme. Additionally, we described in Section 2.3 the routines that make this code particularly fast compared to many N -body codes. Although NBODY6 and the later versions NBODY6++ or the state of the art N -body code which includes post-Newtonian terms, namely NBODY7, are superior when it comes to the speed of the calculations, the disadvantage is the complexity of the code which is probably completely understood only by a handful of people besides Sverre Aarseth. We described previously in Section 2.5 a few modifications we did to the code which are very simple but we could only include them with the help of Sverre.

Due to this limitation, and considering the future work which aims at a more realistic modeling of the first stars of the Universe, their IMF, accretion rates, stellar evolution and ultimately an explicit treatment of the gas, we decided to explore the Astrophysical MULTipurpose Software Environment (AMUSE) which is a python interface that allows the coupling of different codes such as N -body integrators, Hydro codes, stellar evolution and radiative transfer codes.

6.1 The AMUSE framework

The first version of AMUSE, called MUSE [57] was developed in Leiden under the supervision of Simon Portegies Zwart. AMUSE is free to download¹ and to use and provides a very simple python interface to existing codes, handling unit conversions so the user can focus more on the coupling strategies for performing multi-physics simulations. There is currently a version of AMUSE on github² that is frequently being debugged by the community and a google group³ where the users can ask for help related to the installation and the use of the software.

¹AMUSE website: <http://amusecode.org/wiki/WikiStart>

²AMUSE github: <https://github.com/amusecode/amuse>

³AMUSE google group: <https://groups.google.com/forum/#!forum/amusecode>

AMUSE contains a variety of codes written in different languages such as C, C++ and Fortran. These codes are usually free source codes such as ATHENA[58] or MESA⁴ and are referred to as *community codes*.

AMUSE provides a PYTHON interface where the *community codes* are loaded and initialized giving them the initial conditions with generic functions such as `code.add_particles(stars)` and then run with functions such as `code.evolve_model(t_end)`. AMUSE provides a simple way to run simulations combining different codes hiding the complexity of the numerical implementations.

6.2 Bridge

The BRIDGE method was first used by Fujii et al. 2007[41] to model star clusters interacting with their parent galaxies through N-body simulations. In such simulations a galaxy usually consists of 10^{11} particles and a star cluster consists of something like $10^4 - 10^6$ particles, therefore modeling these system with N-body simulations for some Gyr is unfeasible given the different scales such as the relaxation or crossing times. The solution presented by Fujii, M. et al 2007[41] is the split of the system in two smaller systems evolved separately, treating the galaxy dynamics with the tree algorithm, the star cluster with the hermite algorithm and the interaction between the galaxy and the star cluster with the tree algorithm. If we consider the Hamiltonian of the system (the galaxy being the system A and the star cluster being the system B) we have

$$H = \sum_{i \in A \cup B} \frac{p_i^2}{2m_i} + \sum_{i \neq j \in A \cup B} \frac{Gm_i m_j}{|r_i - r_j|}.$$

Now this Hamiltonian can be separated as

$$\begin{aligned} H &= \sum_{i \in A} \frac{p_i^2}{2m_i} + \sum_{i \neq j \in A} \frac{Gm_i m_j}{|r_i - r_j|} + \sum_{i \in B} \frac{p_i^2}{2m_i} + \sum_{i \in B} \frac{Gm_i m_j}{|r_i - r_j|} + \sum_{i \in A, j \in B} \frac{Gm_i m_j}{|r_i - r_j|} \\ H &= H_A + H_B + H_{int}, \end{aligned}$$

where H_A and H_B are the Hamiltonians of the systems A and B , respectively, and additionally the interaction Hamiltonian H_{int} only depends on the separation of the systems. Now the idea behind the bridge method becomes more clear, we can perform a time evolution of the system A using a fast tree method and a more accurate time evolution of the system B using a direct method, whereas the interaction is treated as pure momentum kicks. In AMUSE these momentum kicks are computed with a Leapfrog scheme and we can use different codes for treating systems A and B .

⁴MESA webpage: <http://mesa.sourceforge.net/>

6.3 AMUSE simulations

We decided to use the AMUSE framework to do the simulations of stellar collisions in dense star clusters with the aim to make more realistic simulations which treat not only the dynamics of the stars in the cluster but also the evolution of the gas and eventually the accretion onto the stars and their feedback on the gas. We describe in this section the first steps towards the realization of these objective starting from the simplest case of pure dynamical evolution using the AMUSE framework, comparing these results to the outcome of the simulations with NBODY6.

6.3.1 Pure dynamical simulations

We use the same setup described in Sec. 3 and model a star cluster with $10^4 M_{\odot}$ and a half-mass radius of $R_h = 0.14$ pc, varying the total number of stars from $N = 100$ to $N = 5000$ and the stellar radius from $R_{\text{star}} = 20 R_{\odot}$ to $R_{\text{star}} = 5000 R_{\odot}$. The collision process is treated as in NOBODY6 replacing the colliding stars by a new star whose mass is the sum of the masses of the colliding stars and no mass loss is included. The radius is calculated requiring that the density of the product is the same as the density of the colliding stars (see Sec. 2.4.2). We merge two stars once their separation d is equal or smaller than the sum of their radii, this is $d \leq R_1 + R_2$. We use the same criteria for simulations with `ph4` and with NBODY6. The evolution of the clusters is calculated with the fourth-order Hermite integrator `ph4` [59, Sec. 3.2], the same scheme used in NBODY6. Here we present a comparison of the results produced by these two codes. First we note that the amount of collisions for the same initial conditions is very similar, from 0.06% for $50 R_{\odot}$ stars, to 32% for $500 R_{\odot}$ stars (see Fig. 6.1).

We also expect similar results for the general evolution of the star clusters, in particular, for the mass growth of the runaway object, we expect not only a similar number of collisions but that they occur at similar times. We also expect that the runaway growth starts at approximately the same time. We have tested this by looking at the evolution of a simulation with $N = 5000$ stars, with $500 R_{\odot}$ each, and up to a time of 1000 crossing times. The results showing the evolution of these clusters are presented in Figs. 6.2 and 6.3.

While we have developed, debugged, tested and compared the first scripts to perform simulations with `ph4` in AMUSE, this is only the very first step towards more realistic models of the first star clusters of the Universe and the interaction between the stars inhabiting them. The final models that we aim to produce will contain realistic initial mass functions determined by the environment in which the cluster may form. For example, it is most likely that nuclear star clusters will be formed under turbulent conditions by gas accretion on the central part. Given that turbulence implies more fragmentation we could expect the clusters to consist of a larger number of stars in these environments and possibly with a broader range of masses. On the other hand in the absence of turbulence the initial mass function should be logarithmically flat. One of the most important effects that we want to include is an explicit treatment of the gas, either with an SPH,

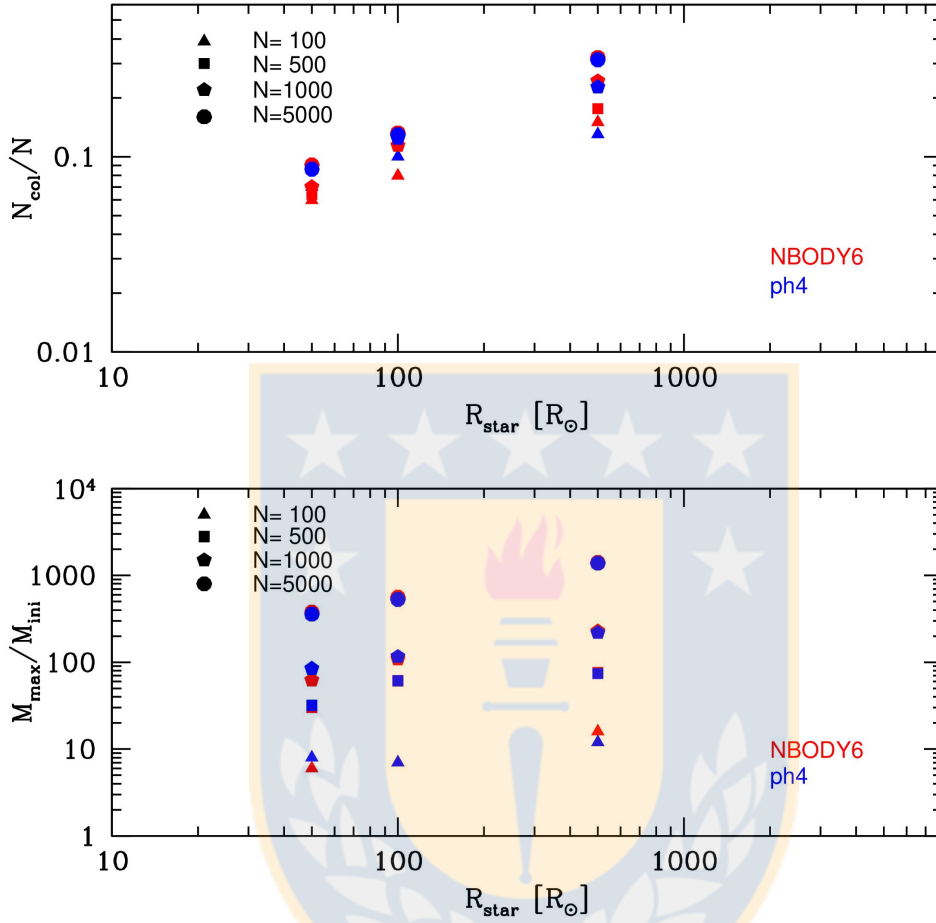


Figure 6.1: Comparison of the results produced by ph4 in AMUSE and NBODY6. The top panel presents the fraction of collisions for different numbers of stars $N = 100, 500, 1000$ & 5000 and different radii $R_{\text{star}} = 50, 100$ & $500 R_{\odot}$. The bottom panel shows the final mass of the runaway object in units of its initial mass for the same different N and R_{star} . In both plots the symbols overlaps and we expect some deviations in the results due to the differences in the codes such as the implementation of the KS regularization (see Sec. 2.3.3) and the neighbour scheme (see Sec. 2.3) in NBODY6. There is excellent agreement between the results. Source: Own elaboration.

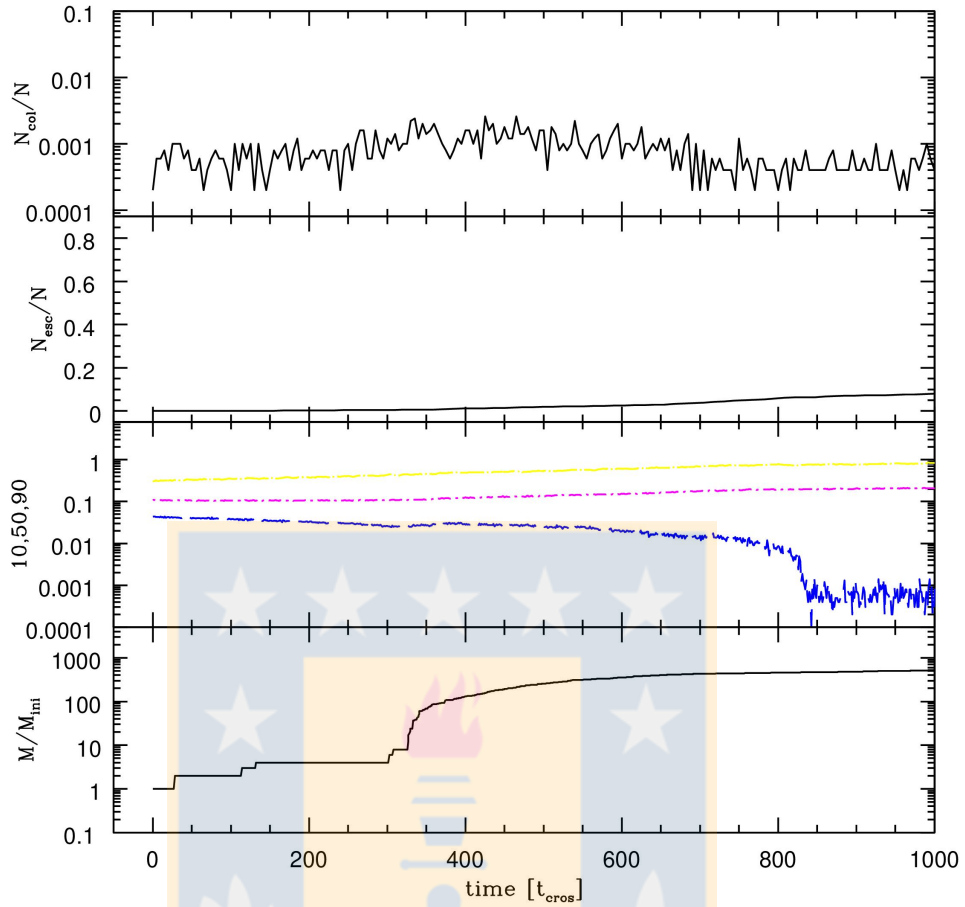


Figure 6.2: General evolution of a star cluster containing 5000 stars with ph4. The stars have a radius of $100 R_{\odot}$, the total cluster mass is $10^4 M_{\odot}$ and the half-mass radius is $r_h = 0.1$ pc. The calculations were performed with the code ph4 in AMUSE. The top panel shows the rate of collisions, this is, the fraction of collisions in bins of 5 crossing times. This rate is initially $0.001 \times N \times 0.2 = 1$ collisions per crossing time, and starts to increase at around $200 t_{\text{cros}}$. At this moment several collisions occur but do not involve the runaway object, instead several stars more massive than the average are formed and the collision rate is around 3 collisions per crossing time until $700 t_{\text{cros}}$. The second panel shows the fraction of escaping stars which slowly starts to increase at around $200 t_{\text{cros}}$ and then monotonically continues increasing up to 0.1 at the end of the simulation. The third panel shows the 10, 50 and 90% Lagrangian radius and we can see that the radius enclosing 10% of the mass is decreasing as the cluster is slowly contracting due to two body relaxation until eventually a high collision rate causes that the 10% of the mass is contained in one single object at around $800 t_{\text{cros}}$, then the 10% Lagrangian radius just traces the position of the runaway star. In the bottom panel we see the mass growth of the runaway object which experiences a rapid growth between 300 and 600 t_{cros} and eventually its mass is enhanced by a factor of 500. Source: Own elaboration.

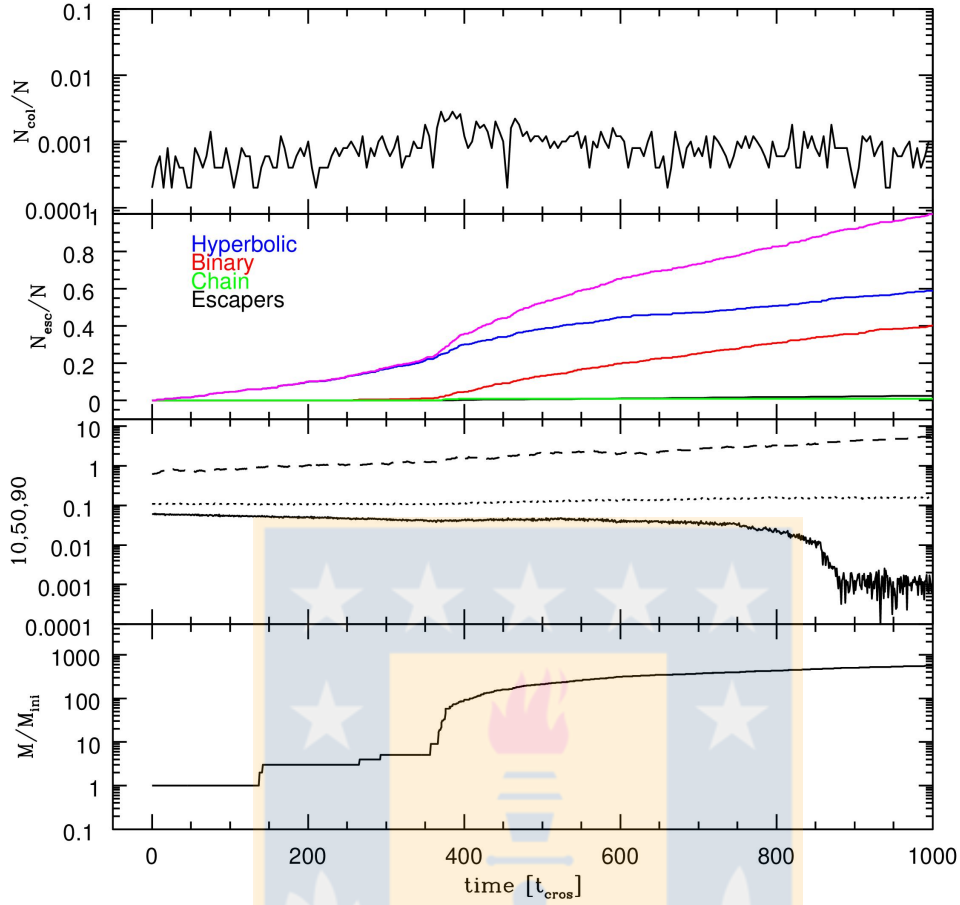


Figure 6.3: General evolution of a star cluster containing 5000 stars with NBODY6. The stars have a radius of $100 R_{\odot}$, the total cluster mass is $10^4 M_{\odot}$ and the half-mass radius is $r_h = 0.1$ pc. This simulation was performed with the code NBODY6. The top panel shows the rate of collisions, this is, the fraction of collisions in bins of 5 crossing times. This rate is initially $0.0008 \times N \times 0.2 = 0.8$ collisions per crossing time, and starts to increase at around $200 t_{\text{cros}}$. At this moment several collisions occur but do not involve the runaway object, instead several stars more massive than the average are formed. At $400 t_{\text{cros}}$ the collision rate is around 2-3 collisions per crossing time until $600 t_{\text{cros}}$. The second panel shows the fraction of escaping stars which is not important and only $< 5\%$ of stars escape from the cluster. The third panel shows the 10, 50 and 90% Lagrangian radius and we can see that the radius enclosing 10% of the mass is decreasing as the cluster is slowly contracting due to two body relaxation until eventually a high collision rate causes that the 10% of the mass is contained in one single object at around $550 t_{\text{cros}}$, then the 10% Lagrangian radius just traces the position of the runaway star. In the bottom panel we see the mass growth of the runaway object which experiences a rapid growth between 300 and $600 t_{\text{cros}}$ and eventually its mass is enhanced by a factor of 500. Source: Own elaboration.

AMR code or the state of the art code AREPO[60]. The explicit treatment of the gas becomes extremely important for accretion processes, especially in the central part of the cluster where massive objects are formed through collisions. A more accurate modeling for the collision process is also important for determining the mass loss and feedback effects on the surrounding gas. Finally stellar evolution could be included in AMUSE with some stellar evolution code, but this would make the simulations much slower, so probably only an approximation for the mass and stellar radius, along with an estimated life-time for the first stars is adequate for our purpose.





Conclusions

We have pursued a first investigation aimed at understanding how the first star clusters that were formed in the Universe evolved, in particular, focusing our study to the most massive and dense stellar systems composed by the very first generation of stars, the so called Pop. III.1 stars whose peculiar properties such as enhanced mass ($M \sim 100 M_{\odot}$) and enhanced radius ($R \sim 100 R_{\odot}$) suggest that the systems containing these stars are very good candidates for forming very massive objects through the process of runaway stellar collisions in the early Universe. The formation of massive objects is of particular interest for explaining the presence of supermassive black holes at redshift $z \sim 6$ given that it is very unlikely that these objects have grown by accretion only, but probably the first black hole seeds were very massive, and finding one feasible mechanism for producing large seeds was the aim of this work.

Cosmological simulations suggest that the first gas clouds collapsed around redshift 20 in dark matter halos of $10^8 M_{\odot}$ and these clouds were as massive as $10^6 M_{\odot}$. Although there is still ongoing research on the assembly of the first star clusters, we conservatively assume that only 1% of the total mass of these clouds is converted into stars, thus we model these clusters with a total mass of $10^4 M_{\odot}$. Additionally, we focus on the densest systems and consider that these clusters had an initial half mass radius of only 0.1 pc. Subsequently, we performed a set of 280 N-body simulations with NBODY6 to explore how the properties of the final most massive object depends on the number of stars in the cluster and their radii. We also performed simulations of clusters under the influence of an external Plummer potential to mimic, at first order, the effects of the gas in these clusters. Our results show that:

- The total fraction of stars that experience collisions in these clusters depend only on the radius of the stars, ranging from 0.01-0.02% for stars with $20 R_{\odot}$, 0.08% for stars with $200 R_{\odot}$ and up to 30-40% for stars potentially having $5000 R_{\odot}$.
- The mass of the most massive object formed in the cluster depends on both the number of stars in the cluster and their radii, with the systems having more stars and larger radii being the best candidates for the formation of more massive objects.

Considering a cluster formed by 5000 stars, each of them with a radius of $500 R_{\odot}$, the most massive object can grow up to 300 times its initial mass.

- The clusters evolve towards core-collapse via close encounter of the stars until the onset of the runaway growth, which occurs after a few tens of crossing times for less populated clusters and around 300 crossing times for clusters containing more stars.
- The time required for the onset of the runaway growth decreases when the stellar radius is increased.
- The time required for the onset of the runaway growth increases with the number of stars due to the increase in the relaxation time of the cluster.
- Runaway stellar collisions in the first star clusters are able to produce massive black hole seeds of $10^3 M_{\odot}$.
- The addition of an external potential produces a delay in the runaway growth.
- Collisions of stars in binary systems are an important contribution to the total number of collisions in a cluster, and under the presence of an external potential binaries are harder to form and easier to destroy.

7.1 Discussion

We have shed some light on the process of runaway growth in the first star clusters of the Universe with a very simplified model, considering equal mass and equal radii stars, no stellar evolution, and without the effects of a gaseous potential. Our N -body models resemble very dense star clusters of $10^4 M_{\odot}$ which is a conservative assumption for the mass of these clusters given that the first collapsing gas clouds had masses of $10^6 M_{\odot}$. There is still ongoing research on the fragmentation process of these clouds, but we know that magnetic fields are not important and that the first stars were very massive and with large radii. Turbulence can lead to the formation of a larger number of stars, with a broader mass range, and further research is needed to determine the amount of turbulence during the formation of the first stars. This should be important for the formation of nuclear star clusters due to the inflow of high velocity gas streams but then also the accretion process is different, especially if the gas is heated to temperatures of 10 000 K. The effects of a gaseous potential were investigated in [61], showing an enhancement in the collision rate and the mass of the final object by a factor of 10 due to accretion on protostars and collisions. We performed a few simulations of clusters subject to an external potential to mimic the effects of the gas, without accretion nor gas expulsion and surprisingly we found a delay in the runaway growth process but at the end the number of collisions and the mass of the most massive object was enhanced due to this extra force. We were able to show that binary collisions are important for building up a massive object and that due to the external potential, the stars move faster

and therefore the formation of binaries is harder, and the destruction is easier. The delay in time was a factor of about 2.5 but we did not see this in the presence of accretion [61], thus modeling accretion is very important at least for the time required to start the runaway growth in the presence of gas. It is also important to understand in more detail the merger process, in particular, how much mass is lost during this event or if there are stellar winds after the collision, but a lot of research is missing on collisions between Pop. III stars. From Gaburov, Lombardi and Portegies Zwart 2008[62] we know that collisions between high mass (up to $80 M_{\odot}$) and low mass stars is less than 10% in all the cases they have studied. Still there are many uncertainties such as the effect of the initial mass function of the population of the cluster and the impact on the mass of the final object. Some characteristics about the first stars are still unknown but there is ongoing research to determine the evolution and life time, as well as the expected number of stars due to fragmentation processes. By including an initial mass function we may expect a mass segregation that would favour the formation of more massive objects but could also lead to more ejections of small stars. Future studies including these effects are needed to better understand the early evolution of the first star clusters and the assembly of massive objects in their center. This is a promising scenario for the formation of very massive black holes.





Bibliography

- [1] J. P. Gardner, J. C. Mather, M. Clampin, R. Doyon, M. A. Greenhouse, H. B. Hammel, J. B. Hutchings, P. Jakobsen, S. J. Lilly, K. S. Long, J. I. Lunine, M. J. Mccaughrean, M. Mountain, J. Nella, G. H. Rieke, M. J. Rieke, H.-W. Rix, E. P. Smith, G. Sonneborn, M. Stiavelli, H. S. Stockman, R. A. Windhorst, and G. S. Wright, “The james webb space telescope,” *Space Science Reviews*, vol. 123, no. 4, pp. 485–606, Apr 2006. [En línea]. Disponible: <https://doi.org/10.1007/s11214-006-8315-7>
- [2] R. Schödel, T. Ott, R. Genzel, R. Hofmann, M. Lehnert, A. Eckart, N. Mouawad, T. Alexander, M. J. Reid, R. Lenzen, M. Hartung, F. Lacombe, D. Rouan, E. Gendron, G. Rousset, A.-M. Lagrange, W. Brandner, N. Ageorges, C. Lidman, A. F. M. Moorwood, J. Spyromilio, N. Hubin, and K. M. Menten, “A star in a 15.2-year orbit around the supermassive black hole at the centre of the Milky Way,” *Nature*, vol. 419, pp. 694–696, Oct. 2002.
- [3] A. M. Ghez, S. Salim, N. N. Weinberg, J. R. Lu, T. Do, J. K. Dunn, K. Matthews, M. R. Morris, S. Yelda, E. E. Becklin, T. Kremenek, M. Milosavljevic, and J. Naiman, “Measuring Distance and Properties of the Milky Way’s Central Supermassive Black Hole with Stellar Orbits,” *The Astrophysical Journal*, vol. 689, pp. 1044–1062, Dec. 2008.
- [4] D. J. Mortlock, S. J. Warren, B. P. Venemans, M. Patel, P. C. Hewett, R. G. McMahon, C. Simpson, T. Theuns, E. A. González-Solares, A. Adamson, S. Dye, N. C. Hambly, P. Hirst, M. J. Irwin, E. Kuiper, A. Lawrence, and H. J. A. Röttgering, “A luminous quasar at a redshift of $z = 7.085$,” *Nature*, vol. 474, pp. 616–619, Jun. 2011.
- [5] E. Bañados, B. P. Venemans, C. Mazzucchelli, E. P. Farina, F. Walter, F. Wang, R. Decarli, D. Stern, X. Fan, F. Davies, J. F. Hennawi, R. Simcoe, M. L. Turner, H. Rix, J. Yang, D. D. Kelson, G. Rudie, and J. M. Winters, “An 800 million solar mass black hole in a significantly neutral universe at redshift 7.5,” *ArXiv e-prints*, Dec. 2017.

- [6] M. J. Rees, “Black Hole Models for Active Galactic Nuclei,” *Annual Review of Astronomy and Astrophysics*, vol. 22, pp. 471–506, 1984.
- [7] M. Volonteri and M. J. Rees, “Rapid Growth of High-Redshift Black Holes,” *The Astrophysical Journal*, vol. 633, pp. 624–629, Nov. 2005.
- [8] A. Ferrara, S. Salvadori, B. Yue, and D. Schleicher, “Initial mass function of intermediate-mass black hole seeds,” *Monthly Notices of the Royal Astronomical Society*, vol. 443, pp. 2410–2425, Sep. 2014.
- [9] M. A. Latif, S. Bovino, T. Grassi, D. R. G. Schleicher, and M. Spaans, “How realistic UV spectra and X-rays suppress the abundance of direct collapse black holes,” *Monthly Notices of the Royal Astronomical Society*, vol. 446, pp. 3163–3177, Jan. 2015.
- [10] J. D. Bowman, A. E. E. Rogers, R. A. Monsalve, T. J. Mozdzen, and N. Mahesh, “An absorption profile centred at 78 megahertz in the sky-averaged spectrum,” *Nature*, vol. 555, pp. 67–70, Mar. 2018.
- [11] M. Volonteri, “Formation of supermassive black holes,” *The Astronomy & Astrophysics Review*, vol. 18, pp. 279–315, Jul. 2010.
- [12] J. M. Bestenlehner, J. S. Vink, G. Gräfener, F. Najarro, C. J. Evans, N. Bastian, A. Z. Bonanos, E. Bressert, P. A. Crowther, E. Doran, K. Friedrich, V. Hénault-Brunet, A. Herrero, A. de Koter, N. Langer, D. J. Lennon, J. Maíz Apellániz, H. Sana, I. Soszynski, and W. D. Taylor, “The VLT-FLAMES Tarantula Survey. III. A very massive star in apparent isolation from the massive cluster R136,” *Astronomy & Astrophysics*, vol. 530, p. L14, Jun. 2011.
- [13] P. A. Crowther, S. M. Caballero-Nieves, K. A. Bostroem, J. Maíz Apellániz, F. R. N. Schneider, N. R. Walborn, C. R. Angus, I. Brott, A. Bonanos, A. de Koter, S. E. de Mink, C. J. Evans, G. Gräfener, A. Herrero, I. D. Howarth, N. Langer, D. J. Lennon, J. Puls, H. Sana, and J. S. Vink, “The R136 star cluster dissected with Hubble Space Telescope/STIS. I. Far-ultraviolet spectroscopic census and the origin of He II $\lambda 1640$ in young star clusters,” *Monthly Notices of the Royal Astronomical Society*, vol. 458, pp. 624–659, May 2016.
- [14] K. Omukai and R. Nishi, “Formation of Primordial Protostars,” *The Astrophysical Journal*, vol. 508, pp. 141–150, Nov. 1998.
- [15] N. Yoshida, K. Omukai, L. Hernquist, and T. Abel, “Formation of Primordial Stars in a Λ CDM Universe,” *The Astrophysical Journal*, vol. 652, pp. 6–25, Nov. 2006.
- [16] T. Hosokawa and K. Omukai, “Evolution of Massive Protostars with High Accretion Rates,” *The Astrophysical Journal*, vol. 691, pp. 823–846, Jan. 2009.
- [17] V. Bromm, N. Yoshida, L. Hernquist, and C. F. McKee, “The formation of the first stars and galaxies,” *Nature*, vol. 459, pp. 49–54, May 2009.

- [18] K. Omukai, T. Tsuribe, R. Schneider, and A. Ferrara, “Thermal and Fragmentation Properties of Star-forming Clouds in Low-Metallicity Environments,” *The Astrophysical Journal*, vol. 626, pp. 627–643, Jun. 2005.
- [19] N. Yoshida, K. Omukai, and L. Hernquist, “Protostar Formation in the Early Universe,” *Science*, vol. 321, p. 669, Aug. 2008.
- [20] K. Omukai, “Protostellar Collapse with Various Metallicities,” *The Astrophysical Journal*, vol. 534, pp. 809–824, May 2000.
- [21] T. Abel, G. L. Bryan, and M. L. Norman, “The Formation of the First Star in the Universe,” *Science*, vol. 295, pp. 93–98, Jan. 2002.
- [22] T. Hosokawa, K. Omukai, and H. W. Yorke, “Rapidly Accreting Supergiant Protostars: Embryos of Supermassive Black Holes?” *The Astrophysical Journal*, vol. 756, p. 93, Sep. 2012.
- [23] D. Lynden-Bell and R. Wood, “The gravo-thermal catastrophe in isothermal spheres and the onset of red-giant structure for stellar systems,” *Monthly Notices of the Royal Astronomical Society*, vol. 138, p. 495, 1968.
- [24] H. Cohn, “Numerical integration of the Fokker-Planck equation and the evolution of star clusters,” *The Astrophysical Journal*, vol. 234, pp. 1036–1053, Dec. 1979.
- [25] L. Spitzer, *Dynamical evolution of globular clusters*, 1987.
- [26] J. L. Breiden, H. N. Cohn, and P. Hut, “The onset of gravothermal oscillations in globular cluster evolution,” *The Astrophysical Journal*, vol. 421, pp. 195–205, Jan. 1994.
- [27] M. Giersz and D. C. Heggie, “Statistics of N-body simulations - III. Unequal masses,” *Monthly Notices of the Royal Astronomical Society*, vol. 279, pp. 1037–1056, Apr. 1996.
- [28] D. C. Heggie, “A theory of core collapse in clusters,” *Monthly Notices of the Royal Astronomical Society*, vol. 188, pp. 525–554, Aug. 1979.
- [29] S. McMillan, P. Hut, and J. Makino, “Star cluster evolution with primordial binaries. I - A comparative study,” *The Astrophysical Journal*, vol. 362, pp. 522–537, Oct. 1990.
- [30] D. C. Heggie and S. J. Aarseth, “Dynamical effects of primordial binaries in star clusters. I - Equal masses,” *Monthly Notices of the Royal Astronomical Society*, vol. 257, pp. 513–536, Aug. 1992.
- [31] J. Gerssen, R. P. van der Marel, K. Gebhardt, P. Guhathakurta, R. C. Peterson, and C. Pryor, “Addendum: Hubble Space Telescope Evidence for an Intermediate-Mass Black Hole in the Globular Cluster M15. II. Kinematic Analysis and Dynamical

- Modeling [</abs/2002AJ....124.3270G>] *Astron. J.* 124, 3270 (2002); *A*],” *The Astronomical Journal*, vol. 125, pp. 376–377, Jan. 2003.
- [32] S. F. Portegies Zwart, J. Makino, S. L. W. McMillan, and P. Hut, “Star cluster ecology. III. Runaway collisions in young compact star clusters,” *Astronomy & Astrophysics*, vol. 348, pp. 117–126, Aug. 1999.
- [33] —, “Runaway Collisions in Star Clusters,” *ArXiv Astrophysics e-prints*, Dec. 2000.
- [34] S. F. Portegies Zwart and S. L. W. McMillan, “The Runaway Growth of Intermediate-Mass Black Holes in Dense Star Clusters,” *The Astrophysical Journal*, vol. 576, pp. 899–907, Sep. 2002.
- [35] S. F. Portegies Zwart and E. P. J. van den Heuvel, “A runaway collision in a young star cluster as the origin of the brightest supernova,” *Nature*, vol. 450, pp. 388–389, Nov. 2007.
- [36] S. E. Woosley, S. Blinnikov, and A. Heger, “Pulsational pair instability as an explanation for the most luminous supernovae,” *Nature*, vol. 450, pp. 390–392, Nov. 2007.
- [37] L. Šubr, P. Kroupa, and H. Baumgardt, “Catch Me If You Can: Is There a “Runaway-mass” Black Hole in the Orion Nebula Cluster?” *The Astrophysical Journal*, vol. 757, p. 37, Sep. 2012.
- [38] H. Baumgardt and R. S. Klessen, “The role of stellar collisions for the formation of massive stars,” *Monthly Notices of the Royal Astronomical Society*, vol. 413, pp. 1810–1818, May 2011.
- [39] N. Moeckel and C. J. Clarke, “Collisional formation of very massive stars in dense clusters,” *Monthly Notices of the Royal Astronomical Society*, vol. 410, pp. 2799–2806, Feb. 2011.
- [40] Y. Sakurai, N. Yoshida, M. S. Fujii, and S. Hirano, “Formation of intermediate-mass black holes through runaway collisions in the first star clusters,” *Monthly Notices of the Royal Astronomical Society*, vol. 472, pp. 1677–1684, Dec. 2017.
- [41] M. Fujii, M. Iwasawa, Y. Funato, and J. Makino, “BRIDGE: A Direct-Tree Hybrid N-Body Algorithm for Fully Self-Consistent Simulations of Star Clusters and Their Parent Galaxies,” *Publications of the Astronomical Society of Japan*, vol. 59, pp. 1095–1106, Dec. 2007.
- [42] P. C. Clark, S. C. O. Glover, and R. S. Klessen, “The First Stellar Cluster,” in *First Stars III*, ser. American Institute of Physics Conference Series, B. W. O’Shea and A. Heger, Eds., vol. 990, Mar. 2008, pp. 79–81.
- [43] P. C. Clark, S. C. O. Glover, R. J. Smith, T. H. Greif, R. S. Klessen, and V. Bromm, “The Formation and Fragmentation of Disks Around Primordial Protostars,” *Science*, vol. 331, p. 1040, Feb. 2011.

- [44] S. J. Aarseth, “NBODY 6: A New Star Cluster Simulation Code,” in *The Chaotic Universe*, V. G. Gurzadyan and R. Ruffini, Eds., 2000, pp. 286–287.
- [45] J. Makino, “Optimal order and time-step criterion for Aarseth-type N-body integrators,” *The Astrophysical Journal*, vol. 369, pp. 200–212, Mar. 1991.
- [46] Sverre Aarseth. NBODY6 User manual.
- [47] S. J. Aarseth, “Dynamical evolution of clusters of galaxies, I,” *Monthly Notices of the Royal Astronomical Society*, vol. 126, p. 223, 1963.
- [48] A. Ahmad and L. Cohen, “A numerical integration scheme for the N-body gravitational problem,” *Journal of Computational Physics*, vol. 12, pp. 389–402, 1973.
- [49] S. Mikkola and S. J. Aarseth, “An efficient integration method for binaries in N-body simulations,” *New Astronomy*, vol. 3, pp. 309–320, Jul. 1998.
- [50] J. R. Hurley, O. R. Pols, and C. A. Tout, “Comprehensive analytic formulae for stellar evolution as a function of mass and metallicity,” *Monthly Notices of the Royal Astronomical Society*, vol. 315, pp. 543–569, Jul. 2000.
- [51] C. S. Kochanek, “The dynamical evolution of tidal capture binaries,” *The Astrophysical Journal*, vol. 385, pp. 604–620, Feb. 1992.
- [52] L. Haemmerlé, T. E. Woods, R. S. Klessen, A. Heger, and D. J. Whalen, “The evolution of supermassive Population III stars,” *Monthly Notices of the Royal Astronomical Society*, vol. 474, pp. 2757–2773, Feb. 2018.
- [53] P. Hut and S. Djorgovski, “Rates of collapse and evaporation of globular clusters,” *Nature*, vol. 359, pp. 806–808, Oct. 1992.
- [54] D. Kasen, S. E. Woosley, and A. Heger, “Pair Instability Supernovae: Light Curves, Spectra, and Shock Breakout,” *The Astrophysical Journal*, vol. 734, p. 102, Jun. 2011.
- [55] C. J. Lada and E. A. Lada, “Embedded Clusters in Molecular Clouds,” *Annual Review of Astronomy & Astrophysics*, vol. 41, pp. 57–115, 2003.
- [56] M. A. Kuhn, L. A. Hillenbrand, A. Sills, E. D. Feigelson, and K. V. Getman, “Kinematics in Young Star Clusters and Associations with Gaia DR2,” *ArXiv e-prints*, Jul. 2018.
- [57] S. Portegies Zwart, S. McMillan, S. Harfst, D. Groen, M. Fujii, B. Ó. Nualláin, E. Glebbeek, D. Heggie, J. Lombardi, P. Hut, V. Angelou, S. Banerjee, H. Belkus, T. Fragos, J. Fregeau, E. Gaburov, R. Izzard, M. Jurić, S. Justham, A. Sottoriva, P. Teuben, J. van Bever, O. Yaron, and M. Zemp, “A multiphysics and multiscale software environment for modeling astrophysical systems,” *New Astronomy*, vol. 14, pp. 369–378, May 2009.

- [58] J. M. Stone, T. A. Gardiner, P. Teuben, J. F. Hawley, and J. B. Simon, “Athena: A New Code for Astrophysical MHD,” *The Astrophysical Journal Supplement Series*, vol. 178, pp. 137–177, Sep. 2008.
- [59] S. L. W. McMillan and P. Hut, “Binary–Single-Star Scattering. VI. Automatic Determination of Interaction Cross Sections,” *The Astrophysical Journal*, vol. 467, p. 348, Aug. 1996.
- [60]
- [61] T. C. N. Boekholt, D. R. G. Schleicher, M. Fellhauer, R. S. Klessen, B. Reinoso, A. M. Stutz, and L. Haemmerlé, “Formation of massive seed black holes via collisions and accretion,” *Monthly Notices of the Royal Astronomical Society*, vol. 476, pp. 366–380, May 2018.
- [62] E. Gaburov, J. C. Lombardi, and S. Portegies Zwart, “Mixing in massive stellar mergers,” *Monthly Notices of the Royal Astronomical Society*, vol. 383, pp. L5–L9, Jan. 2008.

